CFD MODELING AND OPTIMIZATION ANALYSIS OF THERMAL ENERGY STORAGE BASED SOLAR COLLECTORS

A Dissertation
IN
Engineering
and
Electrical and Computer Engineering

Presented to the Faculty of the University
of Missouri–Kansas City in partial fulfillment of
the requirements for the degree

DOCTOR OF PHILOSOPHY

by
VIVEK R. PAWAR

M. S., Gannon University, 2017
B. E., Gujarat Technological University, 2014

Kansas City, Missouri
2022

CFD MODELING AND OPTIMIZATION ANALYSIS OF THERMAL ENERGY STORAGE BASED SOLAR COLLECTORS

Vivek R. Pawar, Candidate for the Doctor of Philosophy Degree

University of Missouri–Kansas City, 2022

ABSTRACT

Among various types of solar collectors, evacuated tube solar collector (ETC) has attracted many attentions especially for the application in solar water heating systems (SWHs). However, due to the intermittency in solar intensity, the ETCs may not work at their maximum functionality. In this study, the computational fluid dynamics (CFD) modeling of a heat pipe ETC (HPETC) with and without the integration of phase change materials (PCMs) is performed. In order to cross-validate the obtained results from CFD and recent experimental analysis, the boundary conditions are set as the field-testing data. The simulation results show an acceptable agreement with the experimental data with an average deviation of 4.8%. In order to further increase accuracy of a numerical model, volume of fluid (VOF) approach is adopted to simulate two-phase (evaporation-condensation process) phenomena inside a heat pipe. The result showed 0.78% increase in numerical model accuracy when heat pipe is simulated as a two-phase device in comparison with

the simplified approach (in which HP is considered as a high thermal conductive device). The result of this study showed improvement in numerical model accuracy when VOF model is adopted. However, VOF approach is found very time consuming. As a result, simplified numerical approach is adopted to optimize thermal performance of a HPETC system. The performance of an HPETC is optimized by investigating the effect of HP position and various energy storage materials in both normal and on-demand operation. The results show that the solid-to-liquid phase change process was expedited by 48 minutes when the HP shifted from the top to the center of the glass tube. On the other hand, during normal operation, the maximum liquid fraction of PCM was reached up to 98% in an optimized system where the conventional system reached up to only 74%.

During normal operation, It is observed that the HPETC system integrated with PCM struggled to reach melting fraction of 100% due to its poor thermal conductivity. The issue of poor thermal conductivity is addressed by impregnation of high thermal conductive porous metal to the PCM. To demonstrate the viability of proposed approach, experimental analysis is carried out. The proposed system has reported maximum thermal efficiency of 71.71% while conventional system showed maximum thermal efficiency of only 29.14%. Impregnation of porous metal to the PCM showed promising result and improved thermal performance in HPETC system. The same approach is used to improve electrical and thermal performance of a photovoltaic-thermal (PVT) system. CFD analysis is performed to assess the effect of integrating PCM + Cu porous metal with PVT

system. In addition, during the simulation, a real-time transient solar radiation boundary condition is applied to accurately predict the performance parameters such as the surface temperature of the PV cell, melting fraction of PCM, and the thermal energy stored by the system. The PVT system integrated with PCM + Cu porous metal system exhibited electrical efficiency of 11.49% which is 12.09% higher compared with PVT system integrated with pure PCM. In addition, PV cell temperature is also decreased by 23.03 °C for PVT system integrated with PCM + Cu porous metal. The outcome of this study can be a benchmark for further optimization of thermal energy storage based solar collectors.

APPROVAL PAGE

The faculty listed below, appointed by the Dean of the School of Graduate Studies, have examined a dissertation titled "CFD Modeling and Optimization Analysis of Thermal Energy Storage Based Solar Collectors," presented by Vivek R. Pawar, candidate for the DOCTOR OF PHILOSOPHY degree, and hereby certify that in their opinion it is worthy of acceptance.

Supervisory Committee

Sarvenaz Sobhansarbandi, Ph.D., Committee Chair and advisor
Department of Civil & Mechanical Engineering

Masud Chowdhury, Ph.D., Co-discipline advisor
Department of Computer Science & electrical Engineering

Gregory King, Ph.D., P.E.
Department of Civil & Mechanical Engineering

Amirfarhang Mehdizadeh, Dr. Ing.
Department of Civil & Mechanical Engineering

Mahbube Khoda Siddiki, Ph.D.
Department of Computer Science & electrical Engineering

CONTENTS

ILLUSTRATIONS

TABLES

ACKNOWLEDGEMENTS

I would like to sincerely thank my advisor Dr Sarvenaz Sobhansarbandi for her advice and direction during my research at University of Missouri-Kansas City. I have learned a lot through my work with her guidance and greatly appreciate her support. I have acquired great experience working with her and I am grateful to have had the opportunity to be a part of her research group. My very special thanks to my lab mates/friends, Arman Nokhosteen, Tyler O'Neil, Celine Lim, Ozkaya Onur, and Jordan Berg for their support in the past few years.

Last but not least, I would like to thank my parents and my sisters, who never ceased to encourage and support me in my life. I owe them everything that I have achieved.

CHAPTER 1

CFD MODELING OF A THERMAL ENERGY STORAGE BASED HEAT PIPE EVACUATED TUBE SOLAR COLLECTOR

This research work is published in *Journal of Energy Storage* in 2020:
"Pawar, V. R., & Sobhansarbandi, S. (2020). CFD modeling of a thermal energy storage based heat pipe evacuated tube solar collector. *Journal of Energy Storage, 30, 101528.*"
DOI: https://doi.org/10.1016/j.est.2020.101528

1.1 Introduction

Solar irradiance is a widely available source that can be converted to thermal energy by utilizing solar collectors. Among various types of solar collectors, evacuated tube solar collector (ETC) has attracted many attention especially for the application in solar water heating systems (SWHs). Based on various heat extraction mediums, the ETCs may be classified in three different categories of water-in-glass, U-type and heat pipe. The water-in-glass ETC consists of flooded single-ended tubes, where the water is in direct contact with the absorber surface. The heat transfer in this collector is achieved by natural circulation of water through the single-ended tubes [25,104]. The glass tubes used in this type of collectors can withstand only a few meters of water head. Hence, the water-in-glass ETC can be only used in low-pressure applications. In the U-type ETC system, copper made U-pipe is brazed with fin and inserted into the inner glass tube. The heat transfer fluid (HTF) is injected in the copper tube with an optimum flow rate to extract the

heat from the collector [59, 109]. In this type of collector, the thermophysical properties of the HTF directly affect the thermal efficiency of the collector.

The heat pipe ETC (HPETC) consists of a heat pipe that is located inside the inner tube. The heat pipe contains a heat transfer fluid (typically water or ethylene glycol) that transfers the heat to the system's manifold. The liquid in the heat pipe has a low boiling point, so when it is heated, the liquid inside the pipe begins to vaporize and rapidly rises to the top of the heat pipe while carrying a large amount of energy to the manifold. As the heat is off-loaded to the manifold, the vapor condenses and liquid returns to the bottom of the heat pipe [116]. HPETCs are also convenient for maintenance in comparison with the other types of ETC due to the dry connection between the water manifold and the glass tubes. Moreover, the characteristics of the heat pipe, such as anti-freezing property, rapid heat transfer from the evaporator to condenser and high performance contribute greatly to enhance the overall performance of the HPETC system [11, 31]. The unique features of HPETC make it attractive for domestic solar water heating applications. Daghigh et al. [37] performed an experimental analysis to investigate the thermal performance of heat pipe solar collector, and developed a numerical model to analyze the thermal efficiency of the system. They reported that a maximum energy and exergy efficiency of 56.8% and 7.2% can be achieved respectively during the cold winter day of January [37]. Shafieian [136] et al. experimentally studied the thermal performance of heat pipe solar water heater (HPSWH) system with a variable mass flow rate technique and different solar working fluids. They used distilled water and nanofluid as a solar working fluid. The results from their study show maximum thermal efficiency improvement of 19.34% when

nanofluid with variable mass flow rate was used [136].

Due to the intermittency in solar radiation, the HPETCs may not work at their maximum functionality. Therefore, in recent years, many researchers have investigated new methods to improve the thermal efficiency of the HPETC system [79, 134]. Among these techniques, the application of phase change materials (PCMs) has received remarkable attention due to large thermal energy density during charging (melting) and discharging (solidification) processes. The stored thermal energy within the PCM, in the form of latent heat, can be utilized at a later time after the sunset or when solar radiation is not available [102, 169]. Navarro et al. [111], studied the effect of the incorporation of shape high density polyethylene spheres with PCM integrated inside the hot water tank in domestic SWH system. The results from their work showed that the effect of PCM is beneficial to keep the temperature of the water at a high level for longer period of time [111]. Salunkhe et al. [127], presented a review study on various latent heat storage materials (LHSMs) in low operating temperature conditions for the application in SWH system. They reported a list of commercially available LHSMs which can be employed for the solar water and space heating applications [127]. Wang et al. [165],conducted an outdoor experiment to investigate the effects of weather conditions, air-flow rates, and inlet temperature on the integrated collector storage solar heaters (ICSSHs). They reported the maximum heat extraction power of 1268.8 W when the air-flow rate was 240 m^3/hr and the inlet temperature was 15$^{\circ}C$. They also found that the thermal storage and release efficiency of ICSSHs reached 67.5% and 98.5%, respectively [165].

Few researchers have investigated the effect of PCMs integrated directly within

the ETCs or as a separate storage tank [13, 63]. Tyagi et al. [157], studied effect of two different PCMs integrated inside a U-tube type ETC in comparison with the system without temporary heat energy storage. They reported that the ETC system with PCM has higher exergy and energy efficiency compared to the system without PCM [157]. Essa et al. [47], performed an experiment with U-tube type ETC to study the effect of working fluid flow rate on the phase change process of paraffin wax filled inside the tube. They stated that, with a flow rate of 0.25 LPM, the efficiency of the ETC system integrated with PCM was increased by 21.9%. Naghavi et al. [108], experimentally investigated the performance of the HPETC attached to a latent heat storage unit. They found that the system has an efficiency of $\sim 38 - 42\%$ during sunny days, while it drops to $\sim 34 - 36\%$ during rainy days [108]. Li et al. [89], performed an experimental and theoretical study of heat pipe solar collector with a composite PCM. The results from their study showed that the storage efficiency of the system reached to 40.17% in mid-temperature operating conditions [89]. Faegh et al. [50], introduced a novel solar still system by using the ETC with an external condenser filled with PCM. They revealed that the presence of the PCM integrated external condenser with ETC, makes the desalination process continue after the sunset with the efficiency of 50% [50]. Feliński et al. [55], performed an experimental study with HPETC integrated with PCM in the Polish city of Czestochowa. They reported that the use of PCM in the HPETC enhanced the annual solar fraction by 20% in the domestic solar water heating system compared with the reference ETC without storage [55]. Recently, Chopra et al. [30], presented an experimental study of HPETC with and without PCM. They compared the performance of HPETC with five different mass flow rates and

reported that with the optimum mass flow rate of 20 L/hr, the efficiency of the HPETC with PCM can be achieved as 36.69% higher than the HPETC without PCM [30].

Due to the rapid change in weather conditions, the high cost of the installation/maintenance and the possible material degradation, the experimental investigation of SWH systems has some shortcomings. Therefore, a simulation analysis of such systems is not only a reliable source for further investigation, but also provides a detailed insight of temperature distribution inside the HPETCs and predict the performance of the system over time. The thermal performance of the HPETCs in 24 hours of normal operation (when pump runs continuously) with variable solar heat flux during the day has been investigated in experimental analysis so far. There are some numerical studies, however, the authors have considered less hour of operation (6-12 hours) [46, 89], a fixed value of solar radiation [94,104] or the combination of these factors. study with the current state of the art, which not only include the full cycle operation of the system with respect to variable solar flux, but also includes the effect of energy storage materials integrated directly within the HPETC. In addition, as can be seen from the literature review on HPETC, most of the researchers have studied the effect of mass flow rate, inlet & outlet temperature of the manifold and efficiency of the HPETC. Till now, no one has studied the effect of solar radiation on the melting and solidification of the PCM inside the glass tube for the 24 hours of operation. The aim of this study is to perform a three dimensional transient CFD modeling of the HPETC system using ANSYS Fluent 19. In phase-I of the study, the 3D model of commercially available HPETC is simulated, while in the phase-II the HPETC integrated with the PCM is developed with field-testing conditions. During the

simulation, the fin temperature data were tracked with respect to flow time of 24 hours of operation to validate the experimental outcome. Moreover, the melting fraction of the PCM inside the glass tube was also recorded which provides the charging and discharging behavior of the PCM. The comparison of the obtained results from CFD and the previous experimental work is performed.

1.2 Background

The novel method of integrating the HPETC with organic PCMs for the application in a domestic SWH system was proposed for the first time in my supervisor's experimental work [116]. The operation of SWH system was investigated during both normal and on-demand (stagnation) operation in Dallas, TX. The feasibility of the system was evaluated via commercially available solar collectors (ETC-10). The solar irradiation data were recorded using an SP-Lite2 pyranometer during the consecutive days of the experiment. The schematic of the HPETC integrated with PCM is shown in Figure 1. The geometry consists of two concentric glass tubes with the space between the glass tube is evacuated to form an insulating vacuum which greatly reduces conduction and convection heat losses. Heat transfer fin inside the glass tube serves the purpose of both to hold the heat pipe in place and also transfer the heat from the absorber tube to the heat pipe and consequently to the system's manifold. To measure the fin temperature, several thermocouples were attached at the top and bottom part of the aluminum fin and the manifold and the transient temperature were recorded by using a OMEGA HH309A data collector

during 24 hours of operation. The temperature of the fin was recorded for both the conventional HPETC with no PCM and the HPETC integrated with PCM, working parallel together.

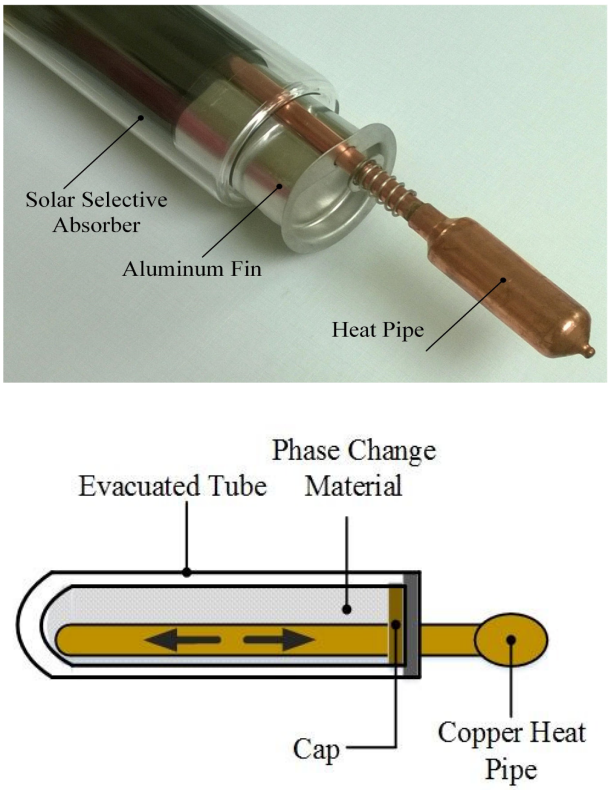

Figure 1: HPETC design configuration [116].

The thermal efficiency (η_s) of such a system is defined as the ratio of heat transfer rate ($\dot{q}$) over the product of collector gross area (A_c) and the total global solar radiation (G_t) on the surface of the collectors [151]. The results from experimental work showed an efficiency improvement of 26% for the normal operation and 66% for the stagnation mode compared to the conventional HPETC that lacks phase change materials. The benefit of

this method includes enhanced performance by extracting stored latent heat from the PCM when solar intensity is insufficient and providing hot water during peak hours.

1.3 Computational fluid dynamics modeling

The commercial CFD package of ANSYS-Fluent 19 is utilized for the transient simulation of HPETC.

1.3.1 System's configuration

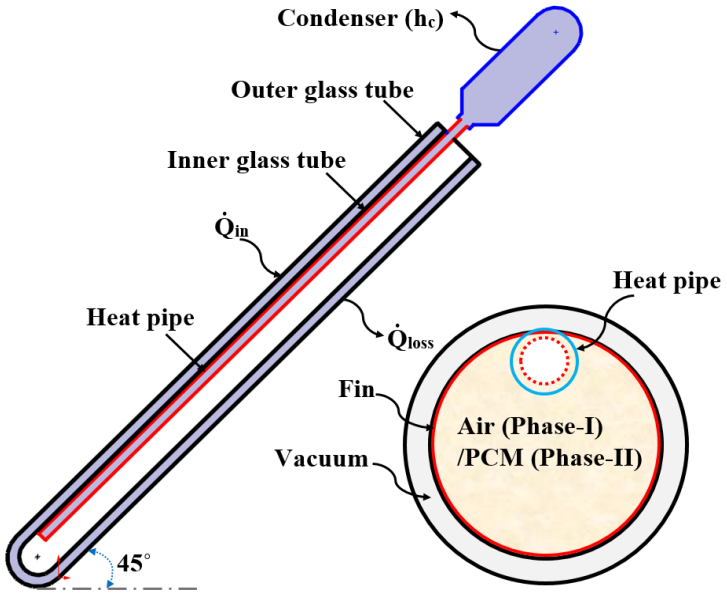

Figure 2: Schematic of HPETC.

The ANSYS design modeler is used to generate 3D geometry of HPETC. Figure 21 shows a schematic diagram of HPETC system. The outer glass tube is defined as a transparent surface allowing sunlight to pass through, while the surface of the inner glass tube is defined as an opaque wall with an absorptance of 0.92. The aluminum fin is

defined as a pure conductive layer with a thickness of 0.2 mm. The heat pipe is made of copper containing a small volume of distilled water as a heat transfer fluid (HTF).

As the vacuum environment is defined in the heat pipe, the HTF boils at a relatively low temperature of $\sim$ 30 °C. Due to high heat capacity of the water, a large amount of energy can be transferred from the tube to the manifold (where water is passing through) during evaporation/condensation process. As the steam offloads the heat, it cools and condenses flowing back to the bottom of the heat pipe (natural convection phenomena) and the cycle is repeated [14, 116]. The dimensions and thermophysical properties of HPETC are listed in Table 6. The selected type of PCM in phase-II of this study is Tritriacontane paraffin (PCM-72) which is directly filled inside the tube. Table 7 shows the thermal properties of PCM-72.

Table 1: Thermophysical properties of PCM-72 [15, 95].

PCM-72	Melting temperature (K)	345
(Tritriacontane paraffin)	Density$_{(s)}$ (kg/m^3)	810
($C_{33}H_{68}$)	Density$_{(l)}$ (kg/m^3)	765
	Specific heat$_{(s)}$ (J/kg-K)	870
	Specific heat$_{(l)}$ (J/kg-K)	1110
	Thermal conductivity (W/m-k)	0.21
	Latent heat of fusion (kJ/kg)	256
	Viscosity (kg/m-s)	0.026
	Solidus temperature (K)	338.83
	Liquidus temperature (K)	345.18

Table 2: Dimensions and thermophysical properties of HPETC [14].

Component	**Properties**	
Glass tubes	Outer tube diameter (m)	0.058
(Borosilicate glass)	Inner tube diameter (m)	0.047
	Thickness (m)	0.0018
	Length (m)	1.8
	Density (kg/m^3)	2230
	Specific heat (J/kg-K)	980
	Thermal conductivity (W/m-k)	1.14
	Transmittance	0.92
Absorber coating	Thickness (m)	0.0001
(Al-N)	Absorptance	0.92
	Emittance	0.08
Fin	Thickness (m)	0.0002
(Aluminum)	Length (m)	1.8
	Density (kg/m^3)	2699
	Specific heat (J/kg-K)	900
	Thermal conductivity (W/m-k)	210
Heat pipe	Evaporator length (m)	1.73
(Copper)	Evaporator diameter (m)	0.008
	Condenser length (m)	0.045
	Condenser diameter (m)	0.01985
	Total length (m)	1.8
	Density (kg/m^3)	8978
	Specific heat (J/kg-K)	381
	Thermal conductivity (W/m-k)	38000

1.3.2 Mesh

The tetrahedral unstructured mesh is applied to the geometry with the patch conforming method. The mesh is divided into five regions. To control the number of nodes, hexahedral elements with the size of 0.004 m are selected for the outer glass tube and vacuum region. On the other hand, tetrahedral mesh with inflation is applied to the inner glass tube, fluid domain (air/PCM) and heat pipe. Six layers of cells with an element size

of less than 0.001 m are constructed adjacent to the surface of PCM and heat pipe. Moving further from the surface to the center of fluid domain, the element size is increased up to 0.002 m. HPETC mesh cross-sectional views are represented in Figure 23.

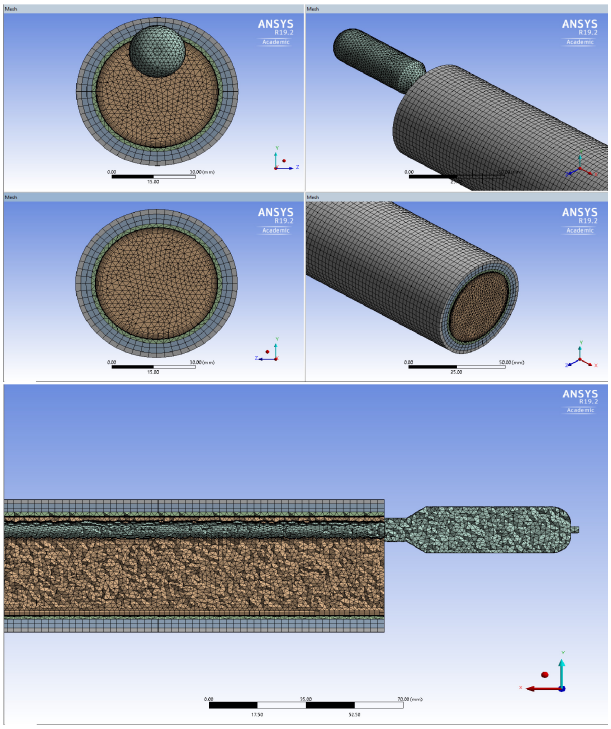

Figure 3: HPETC mesh cross sectional views.

1.3.3 Boundary conditions

In both phases, mounting angle of 45° is considered (recommended by manufacturer) and initialized at a temperature of 298 K [14]. The solar irradiance data recorded during the previous experimental work (Figure 4), is applied as a boundary condition using a user-defined function (UDF) in ANSYS Fluent. In UDF, a time-dependent polynomial function for solar irradiance is written in C++ language and compiled with the

solar load model. Equation 3.1 is used to calculate the useful heat transfer gain by the collector [93]:

$$\dot{Q}_{useful} = \dot{Q}_{in} - \dot{Q}_{loss} \tag{1.1}$$

where $\dot{Q}_{loss}$ is set to a fixed value of 0.8 W$m^{-2}K^{-1}$ as suggested by the manufacturer [14], and $\dot{Q}_{in}$ can be calculated as follows:

$$\dot{Q}_{in} = \tau_{og}\tau_{ig}\alpha_a G_t \tag{1.2}$$

where τ_{og}, τ_{ig}, α_a and G_t are the value of transmittance of the outer glass tube, transmittance of inner glass tube, the absorptivity of the absorber surface and the total solar irradiance, respectively.

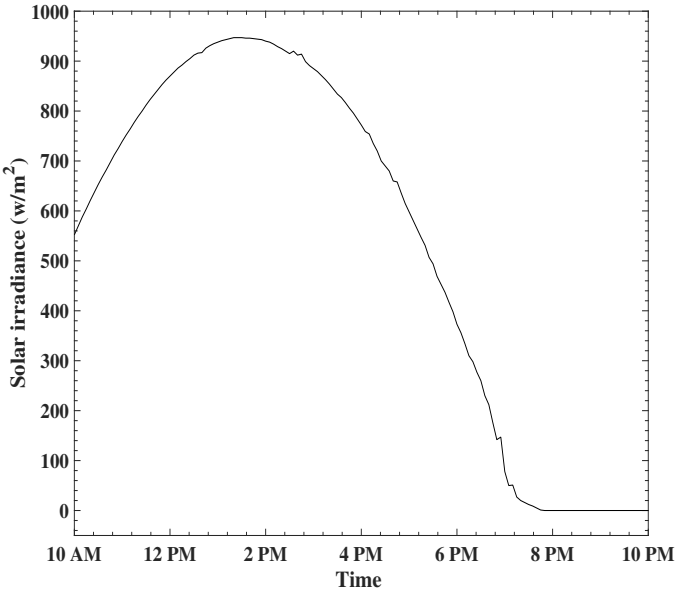

Figure 4: Solar radiation data.

The geographical location of the collector is set as Dallas, TX with the global position of -94.11° longitude and 32.73° latitude to match the experimental work. The conduction heat transfer between the inner glass tube and fin is modeled using shell conduction approach [57]. The primary mode of heat transfer from the outer glass tube to the inner glass tube is only through radiation. The vacuum region is modeled considering the air with a low thermal conductivity of 1.0 e-18 W/m-K [46, 112, 114]. Furthermore, in order to prevent the conduction and convection losses in the vacuum region, the density of the vacuum region is considered as a constant value of 1.225 kg/m^3 and the value of specific heat is considered as 1.0 e-5 J/kg-K [46]. The velocity components in the vacuum region are also set as zero.

A convection heat transfer is applied as a boundary condition to the condenser part of the heat pipe to extract the heat from the inner glass tube. The value of convective heat transfer coefficient (h_c) is calculated using equation (1.3) and applied as a UDF to the heat pipe condenser [10, 49].

$$h_c = \frac{Q}{\pi D L_c (T_c - T_m)} \tag{1.3}$$

where T_c and T_w are the temperature of the condenser and the manifold, respectively, recorded during the experiment for 24 hours of operation. The time-dependent polynomial function of the heat transfer coefficient is written in C++ language and compiled as a boundary condition on a condenser wall of the heat pipe. The following assumptions are considered to develop the CFD model:

- The thermophysical properties of the PCM are assumed to be constant in both solid

and liquid phases except for the density, which contributes to the buoyancy force;

- Boussinesq approximation is considered to express the density variation as: $\rho = \rho_m/(\beta(T - T_{mean}) + 1)$ where $T_{mean} = (T_{solidus} - T_{liquidus})/2$;
- The molten PCM is considered as a Newtonian fluid;
- The molten PCM flow is considered as laminar and incompressible (Ra$< 10^{10}$, Ma< 0.3).

1.3.4 Governing equations

Following the system and the boundary conditions set-up, the total calculation time-step is set as 86,400 seconds which is the duration of 24 hours of system's operation. At each time step, ANSYS Fluent solves the following equations for both PCM and air. The continuity equation:

$$\frac{\partial \rho}{\partial t} + \nabla(\rho \vec{v}) = 0 \tag{1.4}$$

where ρ is density, t denotes time and $\vec{v}$ denotes the velocity vector with components u,v and w in the r,θ and z directions, respectively. The momentum equation is given by:

$$\frac{\partial}{\partial t}(\rho \vec{v}) + \nabla(\rho \vec{v}\vec{v}) = -\nabla p + \nabla \vec{\tau} + \rho \vec{g} + S_g \tag{1.5}$$

where p denotes the pressure, τ is the stress tensor and g is the gravity acceleration. The energy equation:

$$\frac{\partial}{\partial t}(\rho H) + \nabla(\vec{v}\,(\rho H + p)) = \nabla(k\nabla T + \vec{\tau}\,\vec{v}) + S_H \tag{1.6}$$

where k is the thermal conductivity and H is the enthalpy of the PCM, which H is sum of the sensible enthalpy h and the latent heat ΔH that can be written as:

$$H = h + \Delta H \tag{1.7}$$

The sensible enthalpy h can be found from:

$$h = h_{ref} + \int_{T_{ref}}^{T} c_p\, dT \tag{1.8}$$

where h_{ref} and T_{ref} are the reference enthalpy and reference temperature, respectively, and c_p is the constant pressure specific heat. The latent heat ΔH can be calculated from:

$$\Delta H = f_l\, h_{sl} \tag{1.9}$$

where h_{sl} is the latent heat of fusion and f_l is the liquid fraction which is defined by Fluent [57], as follows:

$$f_l = 0, \qquad if \quad T < T_{solidus} \tag{1.10a}$$

$$f_l = 1, \quad if \quad T > T_{liquidus} \tag{1.10b}$$

$$f_l = \frac{(T - T_{solidus})}{(T_{liquidus - Tsolidus})} \quad if \quad T_{solidus} < T < T_{liquidus} \tag{1.10c}$$

The stress tensor $\vec{\tau}$ is given by,

$$\vec{\tau} = \mu[(\nabla\vec{v} + \nabla\vec{v}^{\,T}) - \frac{2}{3}\nabla\cdot\vec{v}\, I] \tag{1.11}$$

where μ is the molecular viscosity and I is the unit tensor. The source term S_g is considered for natural convection and mushy region [57]:

$$S_g = \rho\ \vec{g}\ \beta\ (T - T_{ref}) - \frac{(1 - f_l)^2}{{f_l}^3 + \varepsilon}\ A_{mushy}\ \vec{v} \tag{1.12}$$

where, the first term is the Boussinesq approximation and the second term includes porous medium with porosity in each cell which is considered as a liquid fraction of the cell. In the second term, ε is applied as a very small number (0.001) to avoid division by zero and A_{mushy} is the mushy zone constant. The value of mushy zone constant is considered as 1.0×10^5.

In this study, the heat pipe is modeled by considering the conductivity of heat pipe 100 times higher than the conductivity of copper in order to reduce the calculation time [51, 87, 97, 156]. The energy equation of the heat pipe is expressed as:

$$(\rho C_p)_{hp}\frac{\partial T}{\partial t} = \frac{k_{hp}}{r}\frac{\partial}{\partial r}(r\frac{\partial T}{\partial r}) + \frac{k_{hp}}{r^2}\frac{\partial}{\partial \theta}(\frac{\partial T}{\partial \theta}) + k_{hp}\frac{\partial}{\partial z}(\frac{\partial T}{\partial z}) \tag{1.13}$$

The solar tracking is activated to consider the effect of incidence radiation change over the periphery of the glass tube. The values of transmissivity and reflectivity angular functions of the glass tubes are determined from fourth-order polynomial regression [56, 57]. Transmissivity is given by,

$$\bar{\Gamma}(\Phi, \lambda) = \bar{\Gamma}(0, \lambda)\bar{\Gamma}_{ref}(\Phi) \tag{1.14}$$

$$\bar{\Gamma}(\Phi) = a_0 + a_1 cos(\Phi) + a_2 cos^2(\Phi) + a_3 cos^3(\Phi) + a_4 cos^4(\Phi) \tag{1.15}$$

and reflectivity is considered as:

$$R(\Phi, \lambda) = R(0, \lambda)[1 - R_{ref}(\Phi)] + R_{ref}(\Phi) \tag{1.16}$$

where,

$$R(\Phi) = b_0 + b_1 cos(\Phi) + b_2 cos^2(\Phi) + b_3 cos^3(\Phi) + b_4 cos^4(\Phi) \tag{1.17}$$

where a and b are the constant values in equations 1.15 and 1.17 and ϕ is an angle between solar rays and the glass tube.

The pressure-based solver is employed to calculate the governing equations. SIMPLE algorithm and PRESTO method are employed for pressure-velocity coupling and pressure correction, respectively [57].

1.3.5 Mesh independency check

The pressure, momentum and liquid fraction are considered with relaxation factors of 0.3, 0.5 and 0.9 , respectively, in order to obtain stable convergence. Convergence criteria of 10^{-3}, 10^{-6} and 10^{-9} are selected for continuity, momentum and energy equations, respectively. In order to check the mesh independency of the numerical results, three different grid sets with 526,209, 634,184, and 919,353 number of nodes were tested using time adaptive method with minimum and maximum time step size of 0.01 and 1 second, respectively. The area-weighted average temperature of the fin was selected as the comparison criteria which are shown for different number of nodes in Table 3. Based on the obtained results, the grid with 634,184 nodes was selected for the simulation purpose.

Table 3: Grid size independency check

No. of nodes	Fin temperature (K)
526,209	410.10
634,184	408.82
919,353	408.77

1.4 Results and discussion

The temperature distribution inside the evacuated glass tube is analyzed for the flow-time of 86,400 seconds (24 hours of operation) and compared with experimental data to validate the CFD results. In both phases, the fin temperature was tracked throughout the simulation to investigate the temperature distribution inside the inner glass tube.

1.4.1 Phase-I results

Figure 5 demonstrates the fin temperature comparison between computational and experimental results over 24 hours of operation. As it can be seen in this figure, the temperature profile of the experimental and CFD analysis have the same trend with deviation ranging from 2.8 - 8.6%, while the overall average deviation of 4.8% is found over a time period of 24 hours. In the simulation analysis, the thermal losses from the end face of the collector are neglected and the value of the overall heat loss from the collector is estimated as a constant value. Due to the mentioned factors, there will be a slightly variation between the simulation and experimental results. This deviation percentage is an acceptable value in agreement with previously published work. Essa et al. [46] predicted the performance of an evacuated tube collector numerically with relative errors of 4.2 -

7.8%. Abokersh et al. [4] performed an experimental and numerical analysis of a u-type evacuated tube collector integrated with PCM. They predicted the efficiency of the system and validated it with the TRANSYS model. They reported a maximum deviation of 8.17% between the experimental and the CFD model. As can be seen from Figure 5, the temperature inside the collector is nearly constant around 298K after 10 PM, due to the solar radiation value of zero after sunset (around 7 PM).

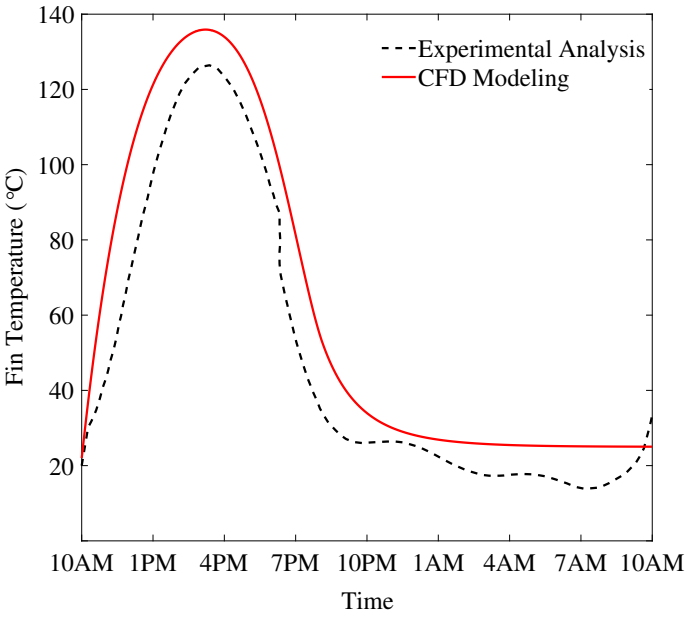

Figure 5: Phase-I: Fin temperature comparison in experimental analysis vs CFD modeling.

Figure 6 shows the temperature distribution inside the HPETC. Temperature contours depict logically the higher temperature near the fin wall which gradually reduces as we move to the center. It can be noticed that the temperature is lower in the vicinity of the heat pipe as heat is continuously extracted from the inner tube.

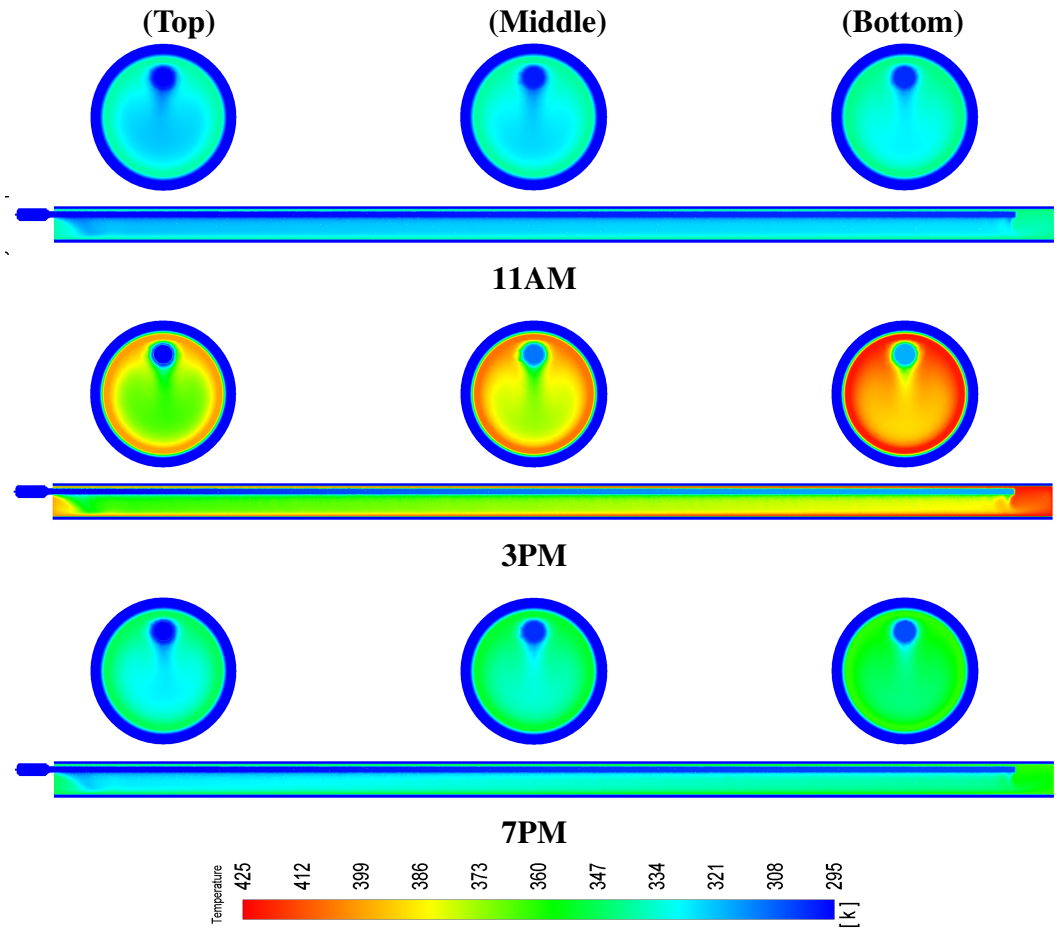

Figure 6: Phase-I: Temperature contours in axial and longitudinal directions.

At 3 PM, a distinct temperature difference at the top, middle and bottom planes can be observed. As it can be seen in this figure, the temperature at the bottom of the tube is much higher than the other parts due to the fact that the heat loss has been ignored in that part as well as there is no heat extraction by the heat pipe from the bottom of the tube. Figure 7 depicts the velocity distribution along the axial plane. Inside the glass tube temperature difference is generated because of higher fin temperature and lower heat pipe temperature. As a result, hot temperature air moves to the upward direction with

higher velocity and by releasing heat to the heat pipe it gets cool down and moves to the downward direction. Moreover, the heat pipe is located in the center and close to the upper part of the glass tube which created two natural convection loops having less temperature in a center of the tube.

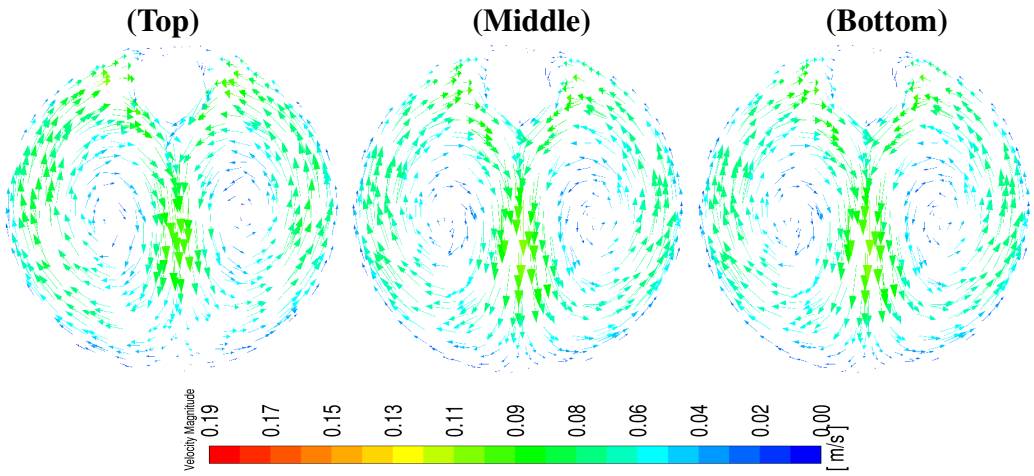

Figure 7: Phase-I: Velocity distribution inside the HPETC at 3PM.

1.4.2 Phase-II results

The 24 hours operation time has set to achieve a full cycle of melting-solidification of PCM, whereas in most of the studies, the researchers investigated this behavior for flow-time of 6-12 hours [38, 46]. Moreover, the liquid fraction of PCM was recorded which isn't feasible to achieve in experimental work. Figure 8 illustrates the comparison of fin temperature between computational and experimental results for the HPETC integrated with PCM. During the period of 24 hours, the computational results showed a good agreement with the experimental data by an average deviation of 2.04%. It can be observed that between 4 PM to 5 PM, a little deviation in fin temperature between

experimental and computational results is found, which is due to the fact that during CFD modeling, the PCM is fully melted earlier than the experiment and further increment in temperature values. This phenomena can be the result of considering constant thermo-physical properties of the PCM in CFD modeling, while there is a slightly change in these properties in real field testing.

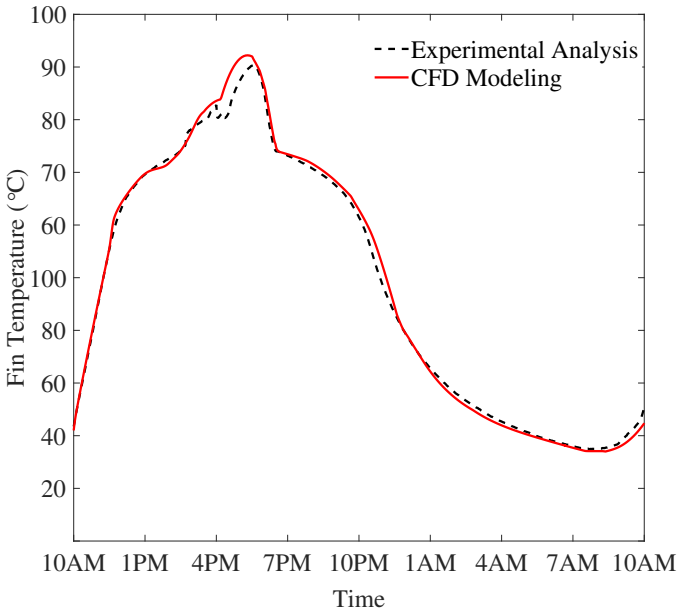

Figure 8: Phase-II: Fin temperature comparison in experimental analysis vs CFD modeling.

Since the conduction is the sole heat transfer mechanism at the beginning, a linear rise in the fin temperature profile can be noticed in Figure 8. In spite of that, slope reduction in fin temperature profile indicates the initialization of the melting process around 11:30 AM, where the fin temperature reaches close to the melting temperature of the PCM ($\sim 72^{\circ}C$). Once the temperature of the PCM reaches to its melting point, the additional

absorbed heat by the HPETC is used to break the intermolecular forces between the solid particles of the PCM. As the result, the temperature of the fin is nearly constant between noon to 2 PM (melting period of the PCM). After completion of the charging process, liquid heating of PCM begins which results in a sharp increase of the temperature profile and average fin temperature reaches its maximum of $\sim 92°C$. On the other hand, after 4:30 PM, the liquid cooling of the PCM begins. As a result, the temperature of fin starts reducing dramatically before reaching the phase-transition temperature ($\sim 72°C$) and after that temperature profile becomes gentle because PCM starts releasing the stored latent heat energy.

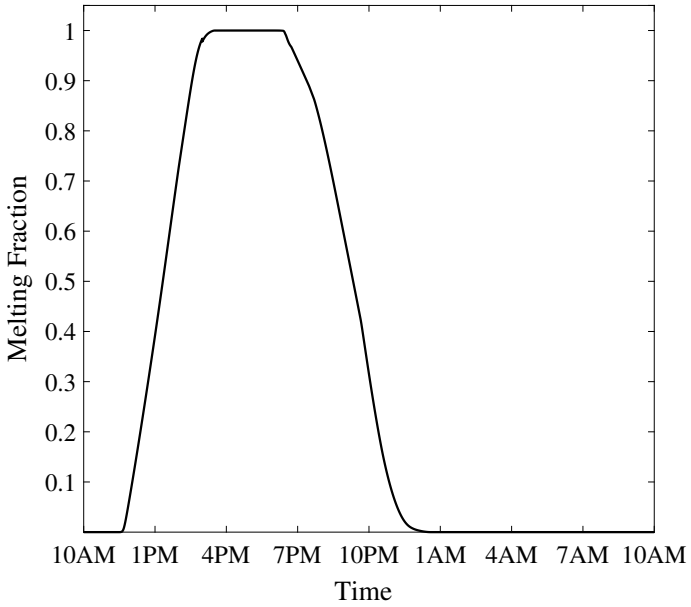

Figure 9: Phase-II: Melting fraction of PCM.

Figure 9 shows the volume-averaged melting fraction of PCM recorded throughout the simulation to study the charging and discharging rate. In the beginning, the slope

of a melting fraction profile is found zero due to the solid heating of the PCM. When fin temperature reaches the phase-transition temperature of the PCM, a steep increase in the value of melting fraction can be seen from 12 PM - 2 PM. The reason for the faster melting rate is the peak sun hours.

As it can be seen in this figure, around 3:30 PM, the PCM inside the glass tube is fully melted. After sunset (around 7 PM), the system starts cooling down, therefore, PCM initiates releasing its absorbed heat in the form of latent heat during solidification process until it completely crystallized around 1 AM, when the liquid fraction is zero. The longitudinal and axial cross-section of liquid fraction distribution inside the glass tube during melting-solidification process at different time steps are depicted in Figure 12 at the top, middle and bottom of the tube. At noon, a very thin mushy layer (the layer between solid and liquid phase) of the PCM close to the fin surface represents the beginning of the melting process. At 2 PM, when solar radiation is at peak, the layer of the liquid PCM becomes thicker at the top part of the glass tube where the sun directly strikes. Moreover, a typical flow structure of buoyancy-driven (natural convection) phase change system is observed in the longitudinal cross-section which shows the molten PCM rises at the top of the glass tube. The natural convection phenomena leads to lower the thermal resistance between fin and PCM which results in faster melting process of the PCM where complete melting is achieved around 4 PM.

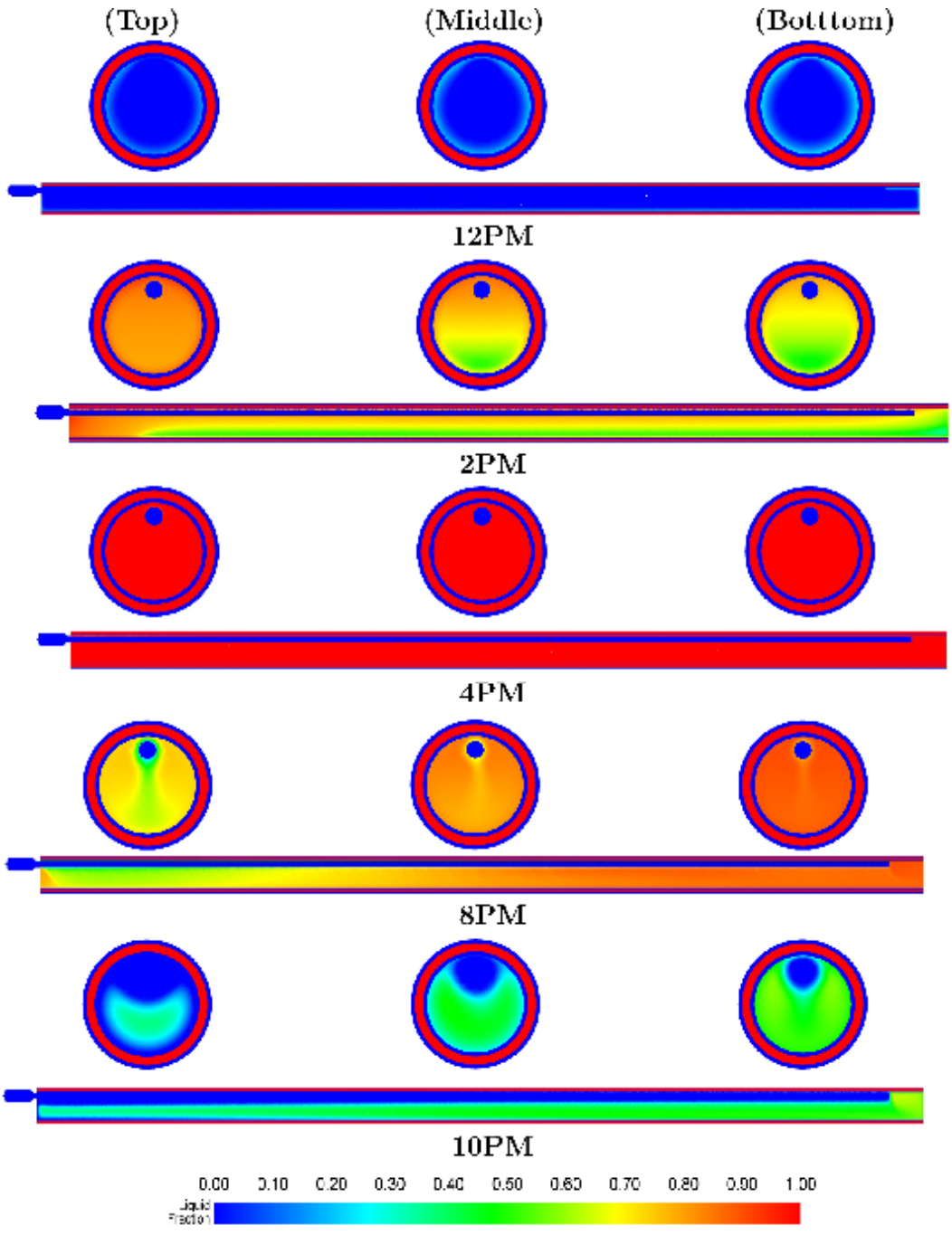

Figure 10: Thermal performance comparison of phase-I vs phase-II of CFD modeling.

The longitudinal and axial cross-section of liquid fraction distribution inside the

glass tube during melting-solidification process at different time steps are depicted in Figure 12 at the top, middle and bottom of the tube. At noon, a very thin mushy layer (the layer between solid and liquid phase) of the PCM close to the fin surface represents the beginning of the melting process. At 2 PM, when solar radiation is at peak, the layer of the liquid PCM becomes thicker at the top part of the glass tube where the sun directly strikes. Moreover, a typical flow structure of buoyancy-driven (natural convection) phase change system is observed in the longitudinal cross-section which shows the molten PCM rises at the top of the glass tube. The natural convection phenomena leads to lower the thermal resistance between fin and PCM which results in faster melting process of the PCM where complete melting is achieved around 4 PM.

The discharging process can be seen in Figure 12 between 8 PM - 10 PM. The crystallization initiates at 7 PM when solar intensity decreases. The solidification starts in the vicinity of the heat pipe and solid PCM layer propagate along the length of the heat pipe as it can be found in the longitudinal cross-section of the HPETC. Figure 12 shows that PCM layer close to the condenser section solidifies faster compared to other sections due to the cooling effect in the manifold. However, unlike the melting process, the solidification process is found less sensitive to the natural convection.

1.4.3 Comparison of Phase-I and Phase-II results

A comparison of the HPETC systems, with and without PCM, has been made to investigate the improved thermal performance of the system. As it can be seen in Figure 11, the maximum fin temperature in the HPETC system without PCM is $\sim 138^{\circ}C$,

while for the system with PCM is only $\sim 90°C$.

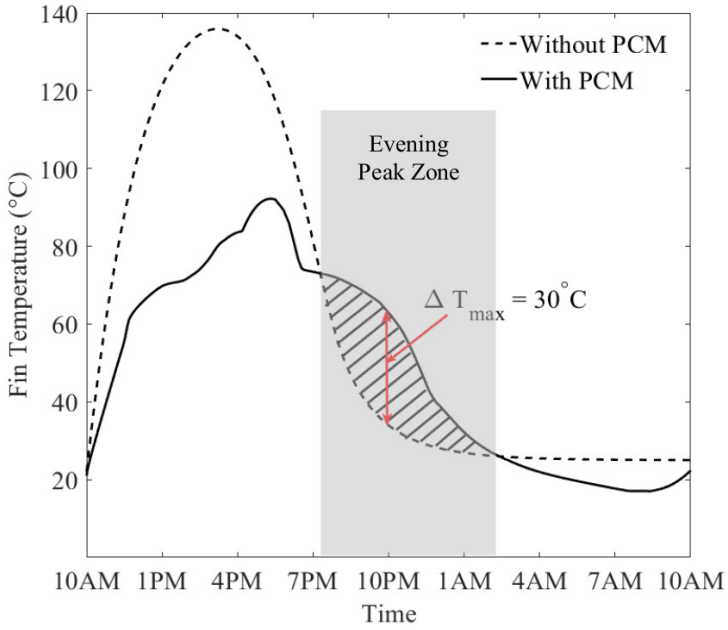

Figure 11: Thermal performance comparison of phase-I vs phase-II of CFD modeling.

This is due to the fact that some portion of absorbed solar radiation is utilized to break the bonding forces between molecules of the PCM (melting process), while in case of the system without PCM, the total amount of solar radiation is used to heat up the temperature inside the tube. Moreover, this phenomena can increase the chances of overheating of the system without PCM. Therefore, by integrating the tubes with PCM this issue can be solved accordingly. The hatched area in Figure 11 indicates the improved thermal performance of the system with PCM by having a maximum temperature difference of $30°C$ during the evening peak hours. Fast cooling in standard system without PCM and delayed cooling of PCM-based system are observed. Therefore, the PCM-based solar water heater system allow the operation of the system for a longer period of time

when solar radiation is not available.

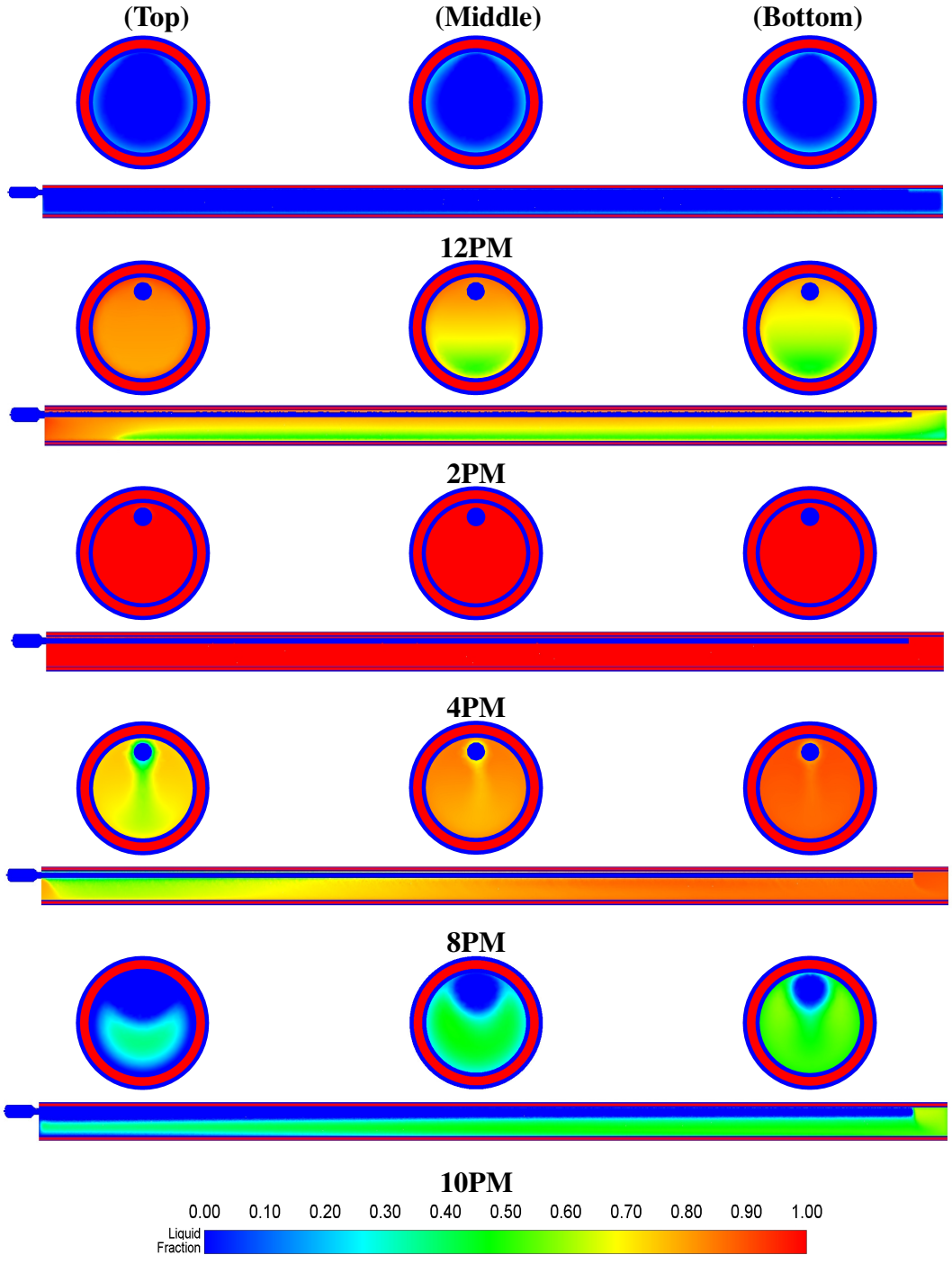

Figure 12: Phase-II: Melting fraction contours in axial and longitudinal directions.

1.5 Summary of this research work

A CFD modeling of an HPETC has been developed to predict their performance for the application in a solar water heater system. In order to cross-validate the obtained results to the previous experimental work, the boundary conditions are set as the real field-testing data. In the first part of the study, the 3D model of commercially available HPETC is simulated, while in the second part, the HPETC integrated with the PCM is developed. The selected type of PCM is Tritriacontane paraffin ($C_{33}H_{68}$) with melting point of 72 °C and a latent heat capacity of 256 kJ/kg. During the simulation, the fin temperature data were tracked with respect to flow time of 24 hours of operation. Moreover, the melting fraction of the PCM inside the glass tube was also recorded which provides the charging and discharging behavior of the PCM. The simulation results show an acceptable agreement between the CFD modeling and the experimental data with an average deviation of 4.8% and 2.04% for Phase-I and Phase-II, respectively. A comparison of the HPETC systems, with and without PCM, has been made to investigate the improved thermal performance of the system, which shows a maximum temperature difference of $30°C$ for the system with PCM during the evening peak hours. Fast cooling in standard system without PCM and delayed cooling of PCM-based system are observed. The obtained results from this study can be used as a benchmark for further optimization of the HPETCs integrated with PCMs in thermal energy storage systems, which allows the operation of the system for a longer period of time when solar radiation is not available.

CHAPTER 2

INVESTIGATION OF EVAPORATION-CONDENSATION PHENOMENA IN HEAT PIPE

This research work is under preparation to be published as a peer reviewed journal article.

2.1 Introduction

Heat pipe (HP) is a passive heat transfer device capable of transfering large amount of heat energy between the heat source and sink. Heat pipe can be divided in three sections, (1) evaporator: where heat is supplied and working fluid is evaporated, (2) condenser: where heat is released and working fluid is condensed, (3) adiabatic section which keeps apart evaporator and condenser sections.

Figure 13 shows schematic and working principle of the heat pipe. As shown in Figure 13, when heat is supplied to the evaporator, working fluid starts boiling only at $\sim 30^{\circ}C$ and converts to vapor (in the presence of vacuum) [14]. This vapor quickly spreads to the other end (condenser) using pressure generated by temperature difference. Condenser section of the heat pipe will be at lower temperature where the vapor offloads its latent heat and condenses flowing back to the evaporator by gravity and the cycle is repeated [14,116]. Heat pipe is also referred as super thermal conductor as it requires very less temperature difference to transfer the heat from one end (evaporator) to other (condenser). Based on the previous experimental and numerical studies, some researcher's have claimed thermal that the heat pipes can have conductivity 100 times higher than the

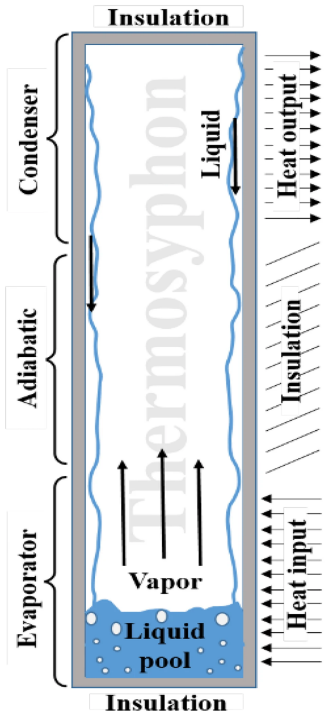

Figure 13: Working principle of heat pipe [19].

copper [51, 87, 156]. In addition, due to reversibility, flexible structure and high heat transfer efficiency, heat pipe have been used in numerous engineering applications, such as cooling of computers and electronic devices [81], solar collectors [132], HVAC systems [18, 150], and heat pump [95].

The performance of heat pipe can be investigated by experimentally, analytically or by using a computational fluid dynamics (CFD) approach. In CFD approach, set of governing equations are solved using finite volume method (FVM) to predict the heat and mass transfer phenomena. In order to investigate the evaporation and condensation inside the heat pipe, De Schepper [40, 41] introduced a volume of fluid (VOF) technique and validated their model with experimental data [40, 41]. Barrak et al. [18] investigated

the performance of oscillating heat pipe experimentally and numerically. They have used water as a working fluid and filling ratio of 50% of the total volume. In their numerical model, they used VOF technique to investigate evaporation and condensation process inside the heat pipe. The result of their study showed maximum deviation of 15% between experimental and numerical results [18]. Vo et al. [158] utilized transparent pyrex tubes to study the flow pattern inside the pulsating heat pipe. They have used high speed cameras to capture the fluid flow motion and reproduced the similar results numerically using VOF model. In addition, they found 5% deviation in heat transfer rate between experiment and CFD analysis [158]. Jouhara et al. [78] numerically investigated the performance of heat pipe using water and refrigerant R134a as a working fluid. They used three dimensional CFD model to compare the evaporation and condensation process of both the working fluids. They also analyzed the effect of different power input on working fluid evaporation evaporation [78].

In order to increase the accuracy of the VOF model, Fadhl et al. [49] implemented user defined function (UDF) within ANSYS-Fluent (commercial CFD solver) to simulate the heat transfer and phase change process inside the heat pipe. They successfully reproduced the evaporation and condensation phenomena in a thermosyphon. They also compared their numerical results with an experiment and found maximum deviation of 12% in temperature profile [49]. Alammar et al. [10] numerically investigated effect of inclination angle and different volume of the working fluid on thermal performance of heat pipe. In order to simulate the heat pipe, they used commercially available CFD tool ANSYS Fluent. They reported maximum deviation of 5% in temperature distribution

compared with an experimental data. In addition, They claimed that heat pipe having a 65% of fill ratio and inclination angle of 90° provides lowest thermal resistance [10]. In previous chapter, CFD analysis of the heat pipe evacuated tube collector (HPETC) is done by considering heat pipe as a super thermal conductor having a thermal conductivity of 100 time than the copper [118]. Result of the previous CFD model is validated with experimental data by comparing fin temperature profile. The overall average deviation of 4.8% is found over a time period of 24 hours. In order to further decrease the deviation, in this chapter, VOF technique is implemented to simulate the multi-phase (evaporation and condensation) phenomena inside the heat pipe. The VOF model can be applied to the two non-miscible fluids with Euler-Euler approach which uses idea of phasic volume fraction and it considers volume fractions as a continuous function of space and time [57, 88]. In the VOF model, Navier-Stoke equations and motion of the different phases are solved by considering the following conditions:

- α_l = 1, cell is considered as a liquid,
- α_l = 0, cell is considered as a vapor,
- α_l = 1, cell is considered as an interface between liquid and vapor.

2.2 CFD modeling of two phase phenomena

The commercial CFD package of ANSYS-Fluent 2020R2 is utilized for the modeling of heat pipe evacuated tube solar collector (HPETC).

2.2.1 System's configuration

Figure 14 shows experimental setup and a schematic diagram of a small size (bench-top) Apricus HPETC. During experiment, solar radiation data is recorded using SP-Lite Pyranometer (directional error less than 10 W/m^2) during experiment and several thermocouples are used to record the fin temperature (T_{fin}), and condenser temperature (T_c). Thermocouple readings are recorded with OMEGA OM-HL-EH-TC-K-CAL thermometer with accuracy $\pm 0.2\%$.

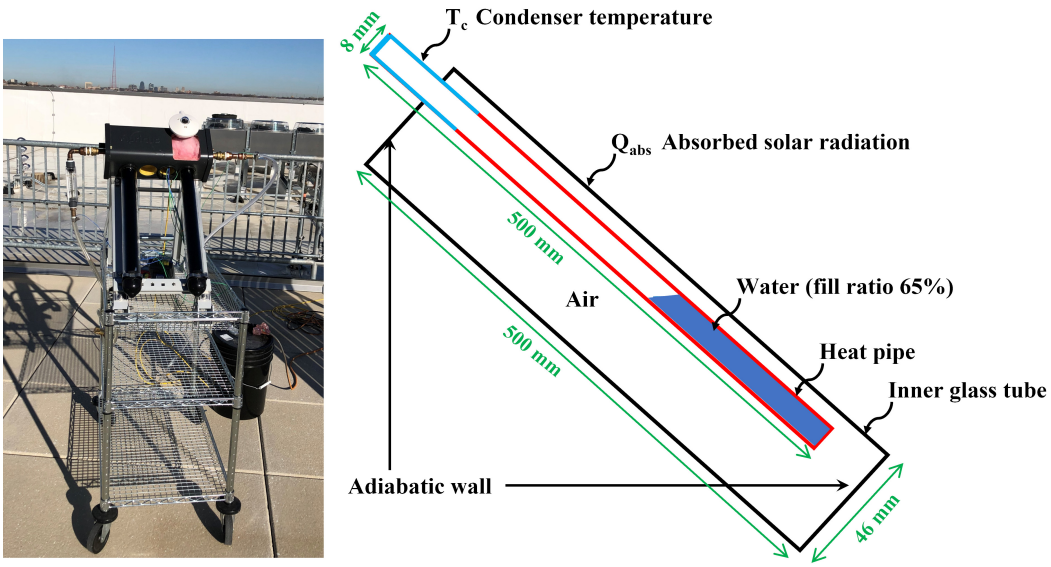

Figure 14: Experimental apparatus and schematic of HPETC

2.2.2 Geometry and boundary conditions

The ANSYS design modeler is used to generate two-dimensional (2D) geometry of HPETC. Figure 15 depicts 2D simplified geometry of HPETC. During the simulation mounting angle of 45° is considered (recommended by manufacturer) [14]. As shown in

Figure 15, only inner glass tube wall and heat pipe is modeled to reduce the computational time. However, the effect of outer glass tube on absorbed solar radiation is accounted in boundary condition.

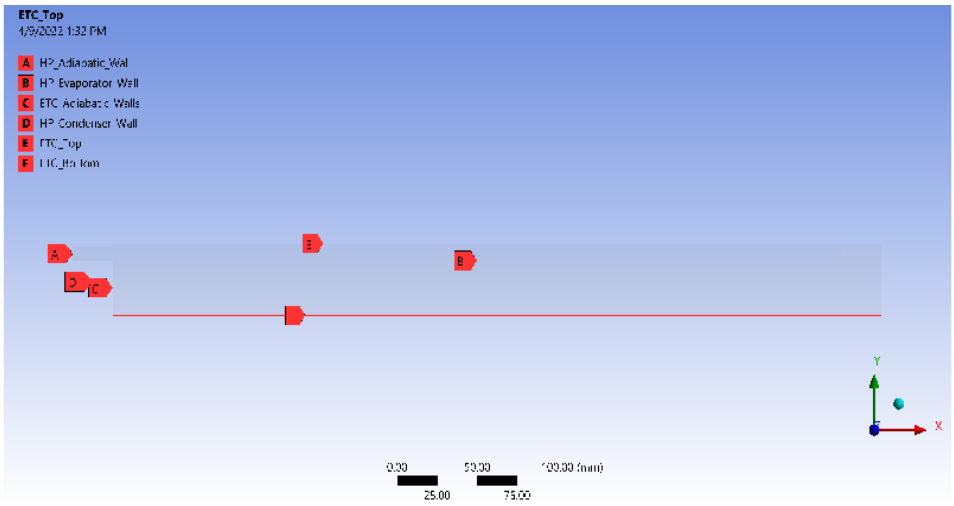

Figure 15: 2D geometry of HPETC

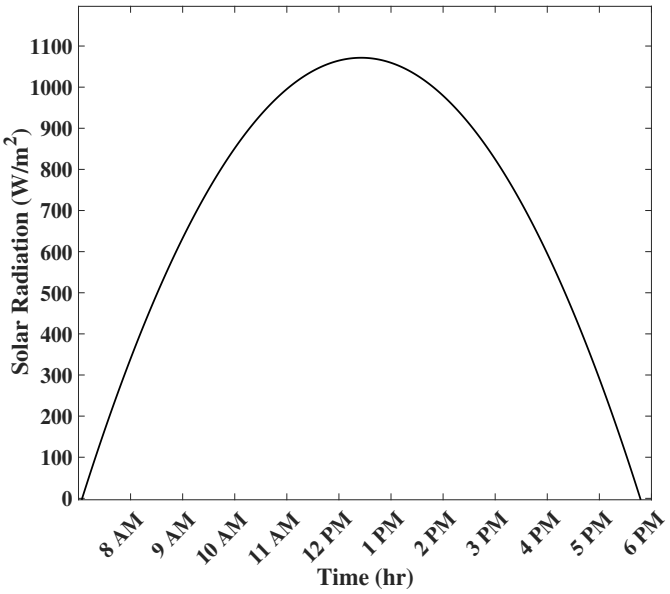

Figure 16: Solar radiation.

The solar irradiance data recorded during experimental is shown in Figure 16.

Solar flux is applied on the inner glass tube wall using a user-defined function (UDF) in ANSYS Fluent. In UDF, a time-dependent polynomial function for solar irradiance is written in C++ language and compiled. Equation 2.1 is used to calculate the useful heat flux gain by the collector [93]:

$$\dot{Q}_{useful} = \dot{Q}_{in} - \dot{Q}_{loss} \tag{2.1}$$

where $\dot{Q}_{loss}$ is set to a fixed value of 0.8 W$m^{-2}K^{-1}$ as suggested by the manufacturer [14], and $\dot{Q}_{in}$ can be calculated as follows:

$$\dot{Q}_{in} = \tau_{og}\tau_{ig}\alpha_a G_t \tag{2.2}$$

where τ_{og}, τ_{ig}, α_a and G_t are the value of transmittance of the outer glass tube, transmittance of inner glass tube, the absorptivity of the absorber surface and the total solar irradiance, respectively. Thermal and optical properties of a HPETC can be found in the chapter 1. In order to simulate the two-phase phenomena inside the heat pipe, VOF technique is adopted to track the fluid's motion. On the other hand, in-built Lee model is used by modifying the evaporation and condensation coefficient values to predict the heat and mass transfer process. In ANSYS Fluent, values for the evaporation (β_e) and condensation (β_c) coefficient are set as 0.1. The same coefficient values are not capable to keep the amount of mass transfer in balance. In this study, following equation is used to calculate the condensation coefficient [167],

$$\beta_c = \beta_e \times \frac{\rho_l}{\rho_v} \tag{2.3}$$

Lastly, condenser temperature (T_c) recorded during experimental analysis is applied as a boundary condition on the condenser wall of heat pipe. The VOF model takes large amount of computational time to simulate the two-phase flow inside the heat pipe. As a result, following governing equations are solved for the flow-time of 10800 seconds which is 3 hr of an operation (11 AM to 2 PM). In addition, the performance of a HPETC is simulated using two different methods, 1) by considering heat pipe as a high thermal conductive device and 2) HP is modeled as using VOF technique. An accuracy of both numerical methods are analyzed by comparing a fin temperature data (recorded during an experiment). In addition, computational time required to simulate HPETC system is also compared.

2.2.3 Governing equations

The commercial CFD package of ANSYS-Fluent 2020R2 is utilized for the modeling of phase change process (evaporation-condensation) inside a heat pipe. At each time step, ANSYS Fluent solves the following equations,

The continuity equation: Continuity equation for the liquid phase,

$$\bigtriangledown \cdot (\rho \vec{u}) = -\frac{\partial \rho}{\partial t} \tag{2.4}$$

where ρ, $\vec{u}$ and t are density, velocity and time, respectively. Equation for calculating volume fraction of the liquid phase (secondary phase),

$$\bigtriangledown \cdot (\alpha_l \rho_l \vec{u}) = -\frac{\partial (\alpha_l \rho_l)}{\partial t} + S_m \tag{2.5}$$

where S_m is the source term to calculate the mass transfer during the phase change

process. While the volume fraction of the primary phase is calculated by applying constraint:

$$\sum_{n}^{l=1} \alpha_l = 1 \tag{2.6}$$

Momentum equation:

$$\frac{\partial(\rho\vec{u})}{\partial t} + \bigtriangledown \cdot (\rho\vec{u}\vec{u}) = \rho\vec{g} - \bigtriangledown p + \bigtriangledown \cdot \left[\mu\left(\bigtriangledown\vec{u} + \bigtriangledown\vec{u}^T\right) - \frac{2}{3}\,\mu \bigtriangledown \cdot uI\right] + F_{CSF} \tag{2.7}$$

where F_{CSF} is the continuum surface forces between two phase has been added to the momentum equation and it can be calculated using following equation [21],

$$F_{CSF} = 2\sigma_{lv}\frac{\alpha_l\rho_l C_v \nabla\alpha_v + \alpha_v\rho_v C_l \nabla\alpha_l}{\rho_l + \rho_v} \tag{2.8}$$

where σ_{lv} and C are the surface tension force between liquid-vapor and curvature while subscripts l and v depicts liquid and vapor, respectively. In order to calculate density and dynamic viscosity at the interface, following equations are used:

Density:

$$\rho = \alpha_l\rho_l + (1 - \alpha_l)\rho v \tag{2.9}$$

Dynamic viscosity:

$$\mu = \alpha_l\mu_l + (1 - \alpha_l)\mu_v \tag{2.10}$$

Energy equation:

$$\frac{\partial(\rho e)}{\partial t} + \nabla \cdot (\rho e\vec{u}) = \nabla \cdot (k \cdot \nabla T) + \nabla \cdot (p\vec{u}) + S_E \tag{2.11}$$

where S_E is the source term to calculate the heat transfer during the phase change process. Source terms (S_m) in Eq. 2.5 and S_E in Eq. 2.11 are calculated using equations

suggested by De Schepper [41] shown in Table 4.

Table 4: Source term for energy equation [41]

Thermal energy	Phase change process		Phase	Source term (S_E)
Mass transfer	Evaporation	$T_{mix} > T_{sat}$	Liquid	S_m = -0.1 ρ_l α_l $\frac{T_{mix}-T_{sat}}{T_{sat}}$
		$T_{mix} < T_{sat}$	Vapor	S_m = 0.1 ρ_l α_l $\frac{T_{mix}-T_{sat}}{T_{sat}}$
	Condensation	$T_{mix} > T_{sat}$	Liquid	S_m = 0.1 ρ_v α_v $\frac{T_{sat}-T_{mix}}{T_{sat}}$
		$T_{mix} < T_{sat}$	Vapor	S_m = -0.1 ρ_v α_v $\frac{T_{sat}-T_{mix}}{T_{sat}}$
Heat transfer	Evaporation	$T_{mix} > T_{sat}$		- 0.1 ρ_l α_l $\frac{T_{mix}-T_{sat}}{T_{sat}}$ LH
	Condensation	$T_{mix} < T_{sat}$		0.1 ρ_v α_v $\frac{T_{sat}-T_{mix}}{T_{sat}}$ LH

During the simulation, VOF model treats the temperature (T) and internal energy ('e') as a mass-averaged quantity which can be calculated by following equations,

Thermal conductivity:

$$k = \alpha_l k_l + (1 - \alpha_l) k_v \tag{2.12}$$

$$e = \frac{\alpha_l \rho_l e_l + \alpha_v \rho_v e_v}{\alpha_l \rho_l + \alpha_v \rho_v} \tag{2.13}$$

where e_l and e_v are,

$$e_l = c_{p,l}(T - T_{sat}) \tag{2.14}$$

$$e_v = c_{p,v}(T - T_{sat}) \tag{2.15}$$

2.3 Model validation

As discussed earlier, VOF model is time consuming. As a result, instead of directly validating VOF model with complex HPETC simulation, first, it is validated with

a simple heat pipe case. The details regarding an experimental setup, geometrical dimensions and boundary conditions can be found in literature published by Fadhl et al. [49]. During the simulation, polynomial functions shown in Eq. 2.17 and Eq. 2.16 are used to calculate density of the water and surface tension forces between water and vapor, respectively. The simulation is carried out for the heat input of 172 w.

$$\sigma_{lv} = 0.09805856 - 1.845 \times 10^{-5}\, T - 2.3 \times 10^{-7}\, T^2 \tag{2.16}$$

$$\rho_l = 859.0083 + 1.2522\, T - 0.002642\, T^2 \tag{2.17}$$

Table 5: Comparison between experimental data and CFD simulation [49].

	Position (m)	T_{Exp} (k) [49]	T_{num} (k) [49]	Error (%)	$T_{current}$ (k)	Error(%)
T_{evap}	0.05	345.75	378.33	9.42%	365.82	5.81%
	0.15	337.45	378.40	12.14%	366.46	8.60%
T_{adia}	0.25	327.45	362.41	10.68%	357.11	9.06%
T_{cond}	0.32	320.55	329.54	2.80%	320.26	0.09%
	0.36	318.85	326.54	2.41%	318.63	0.07%
	0.40	317.95	325.95	2.52%	318.39	0.14%
	0.44	317.05	325.64	2.71%	318.29	0.39%
	0.48	315.95	327.13	3.54%	318.23	0.72%

Table 5 shows a comparison between experimental data, numerical model used by Fadhl et al. [49] and current numerical model. As shown in Table 5, after modifying the evaporation and condensation coefficients in current model error percentage is reduced by almost half compared to the previous numerical model proposed by Fadhl et al. [49]. Figure 17 shows comparison of heat pipe wall temperature between experimental and numerical analysis.

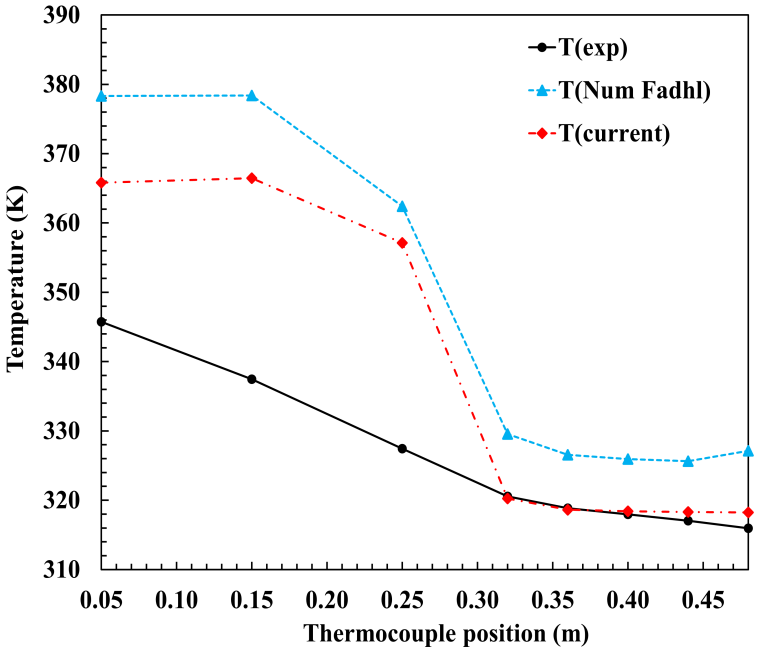

Figure 17: Comparison between experimental data and CFD simulation.

In addition, evaporation and condensation phenomena is also tracked throughout the simulation. Figure 18 depicts the condensation process near the condenser wall which clearly shows that the current numerical model can be applied to investigate the performance of the HPETC system. However, the simulation for the flow-time of 60 seconds took two weeks of simulation time on a regular personal computer with Intel(R) Core(TM) i7-7700 CPU, 32 GB of ram, and with 6 processors.

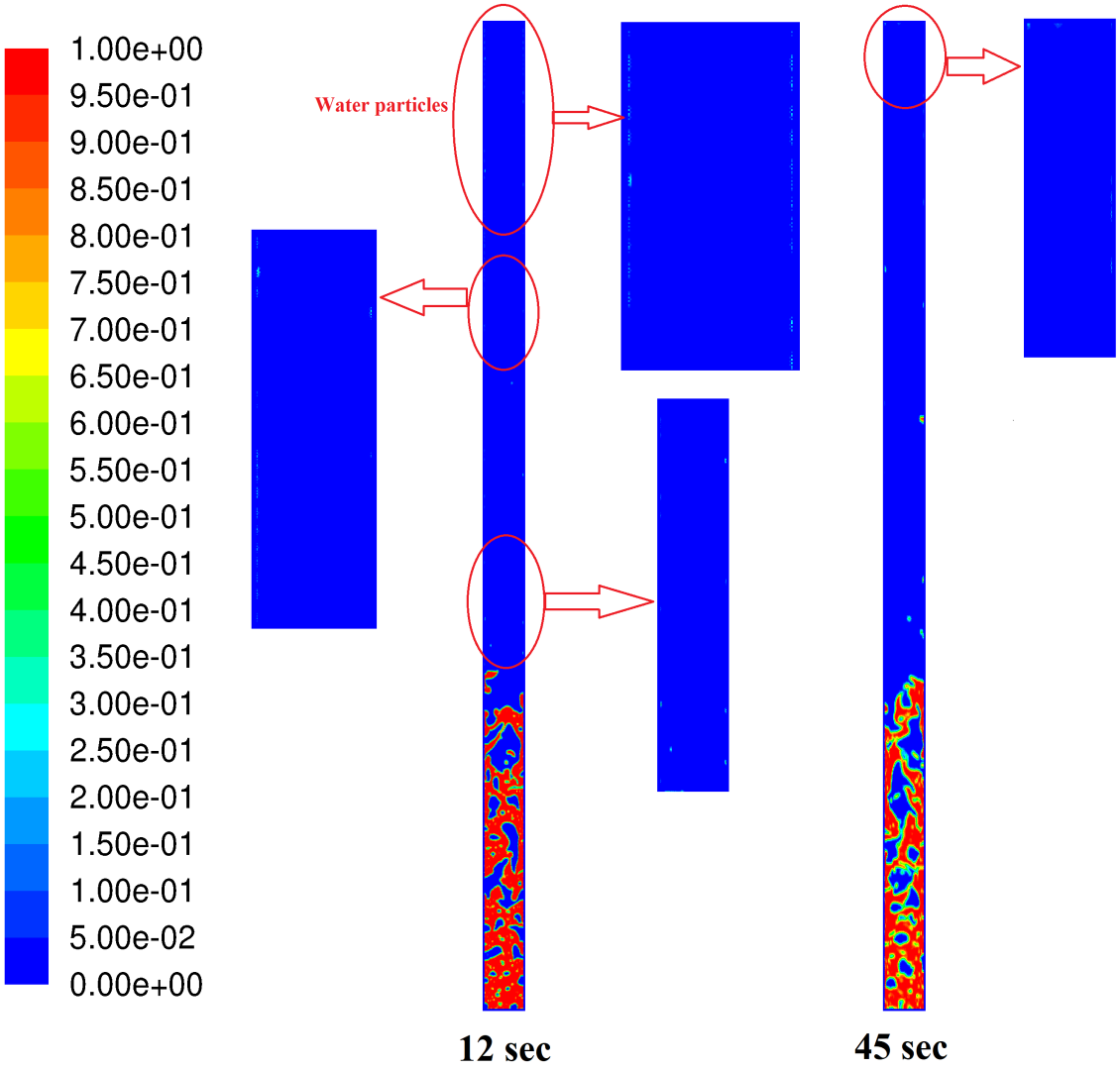

Figure 18: Volume fraction of water inside the heat pipe at different times.

2.4 Results and discussion

In this numerical study, performance of HPETC system is evaluated using VOF approach. As mentioned above, simulation of two-phase flow takes large amount of computational time. As a result, in order to see accuracy of a current VOF model is compared

with CFD analysis of HPETC system simulated by considering HP as a high thermal conductive device. Figure 19 illustrates comparison of CFD analysis of HPETC system using two different approaches. The result showed maximum deviation of 3.19% between CFD and experimental analysis when HP is considered as high thermal conductive device. On the other hand, after implementing a VOF approach, maximum deviation of 2.41% is found between CFD and experimental analysis.

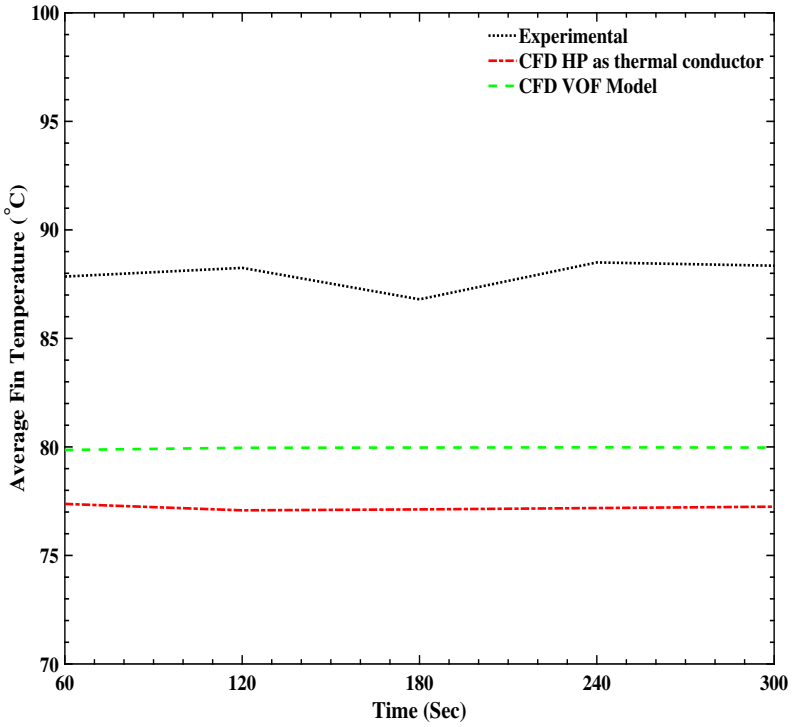

Figure 19: Comparison between experimental and CFD.

In addition, performance evaluation of HPETC system by considering HP as a high thermal conductive device took only 30 minutes of CPU time to calculate the fin temperature by solving governing equations for the flow time of 300 seconds with time-step size of 0.1 second. On the other hand, in second approach, when HP is considered

as two phase device using VOF model, it took two weeks of CPU time to calculate the fin temperature. It clearly shows that, the numerical model accuracy increase of 0.78% was achieved by using the VOF model, however, the CPU time increased by 28 times compared to the simplified numerical approach. As a result, in future (in chapter 3), the performance of HPETC system is optimized by adopting simplified numerical approach in which heat pipe is considered as a high thermal conductive device.

2.5 Summary of this research work

Aim of this numerical study is to show comparison between two different numerical approach to simulate the peformance of HPETC system. Firstly, simplified approach is adopted in which heat pipe is considered as a high thermal conductive device. The result of this numerical aproach is compared with an experimental analysis and showed maximum deviation of 3.19%. Besides, in second approach, heat pipe is considered as a two phase device and complete physics associated with it such as evaporation-condensation is solved to evaluate the performance of HPETC system. The result of a second approach showed 0.78% increase in accuracy. In addition, CPU time is also increased extensively from 30 min to 2 weeks in order to increase 0.78% of accuracy.

CHAPTER 3

DESIGN OPTIMIZATION AND HEAT TRANSFER ENHANCEMENT OF ENERGY STORAGE BASED HPETC

This research work is published in *Sustainable Energy Technologies and Assessments* in 2021:

"Pawar, V. R., & Sobhansarbandi, S. (2021). Design optimization and heat transfer enhancement of energy storage based solar thermal collector. *Sustainable Energy Technologies and Assessments, 46, 101260*."

DOI: https://doi.org/10.1016/j.seta.2021.101260

3.1 Introduction

Common sources of energy such as coal, gas, and oil can be inefficient and produce carbon emissions, which contributes to the global climate change. In the United States, water heating accounts for the second-largest heating demand at approximately 20% of all household energy use [26]. Solar water heating (SWH) systems are capable of reducing household energy usage and carbon dioxide emissions by preheating the air or water before it enters conventional heaters [27]. Solar collectors play an important role in the domestic SWH systems. Solar radiation from the sun transfers through the outer glass of the collector, which is absorbed and converted into heat energy by the solar selective coating (absorber). There are several types of solar collectors available but one of the most efficient type is evacuated tube solar collector (ETC) [146]. In ETC, two concentric

glass tubes are fused at both ends with the space between evacuated at high temperature to form an insulating vacuum which helps to reduce heat losses. Furthermore, the outer glass tube of the ETC is made from transparent glass which allows solar radiation to pass through it, while the inner glass tube is coated with a material having high absorptivity that can convert up to 95% of solar radiation into useful heat [14]. The superiority of the ETC is the circular shape of the absorber which passively tracks the sun resulting in a high solar conversion efficiency. The heat pipe (HP) is held adjacent to the upper surface of the inner glass tube with the help of an Aluminum fin, which also improves the heat transfer between the absorber wall and HP. The Heat pipe is capable of absorbing a huge amount of heat energy from a glass tube and rapidly transfer it to the manifold. The copper made HP contains pure water under a lower vacuum pressure allowing water to start boiling at around only 30°C [14]. Water absorbs a high amount of latent heat energy while forming steam, consequently high heat transfer capacity is achieved by the HP. As water converts into steam, it rapidly flows upward to the head part of the HP where it offloads heat energy to the manifold and condenses back to the liquid phase. The condensed water flows back in a downward direction due to the gravitational force and repeats the same cycle [51, 124]. Due to having such a great design, heat pipe evacuated tube collectors (HPETC) give excellent performance even in cold climates when compared to any other type of solar collectors [17, 62, 146]. Figure 20 (a) shows the schematic of HPETC including its working principle and Figure 20 (b) shows the application of 10 tube HPETC configuration in SWH system.

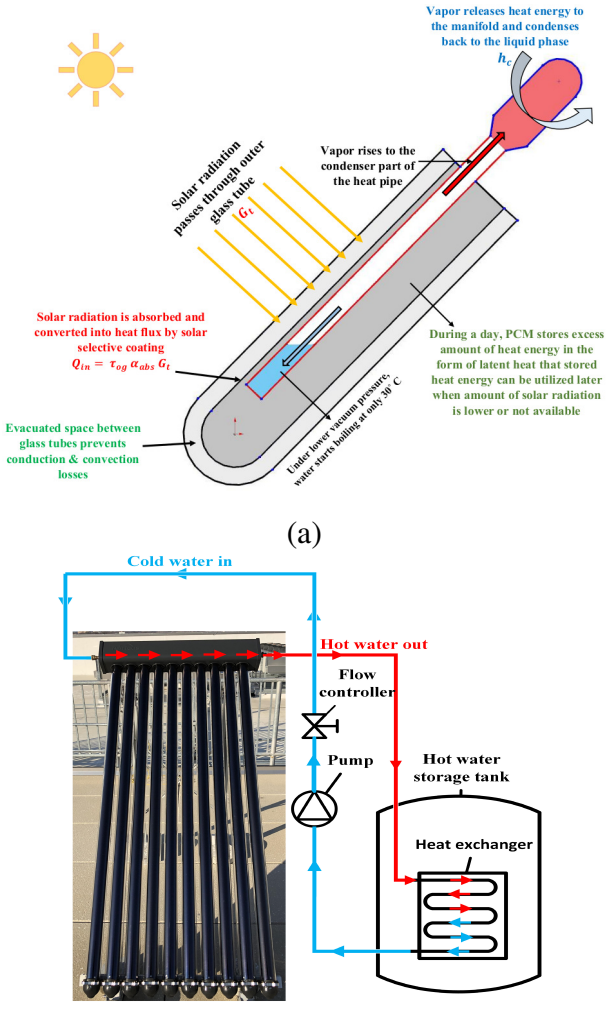

Figure 20: HPETC: (a) Schematic and working principle and (b) Application in SWH system.

Several experimental and numerical analyses have been carried out to optimize the design and thermal efficiency of a HPETC [11, 133]. Daghigh et al. [37] numerically investigated the exergy and energy efficiency of the HPETC for space heating application. They found that the rate of increase in air temperature becomes insignificant after 30

glass tubes and the trend of the thermal efficiency started decreasing with an increase in the number of glass tubes. On the other hand, during a winter day, HPETC with 20 tubes showed the maximum energy of 56.8% and the exergy efficiency of 7.2% [37]. In a recent study, Wang et al. [162] performed an experimental and numerical analysis to study a novel solar collector consisting of arrays of micro heat pipe (MHPA). In their design, they directly glued the solar selective film on the MHPA and placed it inside the transparent glass tube. They reported the maximum efficiency of 85.2% for an airflow rate of $160 m^3/h$. In their other experimental work, they studied and compared the performance of a conventional solar collector and a transparent glass tube collector. They reported the thermal efficiency of 77.6% for conventional solar collector and 85% for the transparent glass tube collector. However, the useful energy gain was found at641 W for conventional and 497 W for transparent glass tube collector [161].

In order to analyze the influence of various heat transfer fluids (HTF) inside the HP, Ersoz et al. [45] employed six different types of HTF inside the heat pipe to study the effect on the performance of HPETC. Moreover, they used three different air velocities of 2, 3, and 4 m/s to extract the heat from glass tubes. In terms of energy and exergy efficiencies, they reported the highest energy efficiency when acetone and chloroform are used with the air velocity of 2 m/s and 4 m/s, respectively [45]. Jayanthi et al. [74] performed an experiment on HPETC using a pure water and refrigerant (R134a) as HTF of HP. The average efficiency of the HPETC was found to be 31.28% and 42.95% when pure water and R134a (respectively) were used as HTF [74]. Shafieian et al. [136] introduced

a flow control technique in their experiment which controls the mass of the working fluid with the change in solar radiation intensity. They set up a three HPETC system, the first with distilled water flowing through the manifold with constant mass flow rate. The second system used nano fluid as working fluid with constant mass flow rate and last, the third system with nano fluid using flow control technique. They compared the third system's performance with the other two HPETC systems. The system with nano-fluid with variable mass flow rate showed an increase in efficiency by 19.34% compared with the system with distilled water with constant mass flow rate. Similarly, compared to the nano-fluid with constant mass flow rate, the third system showed an efficiency improvement of 12.46% [136]. In their other experimental work, Shafieian et al. [135] used the same variable mass flow rate technique during a winter. They noticed significant performance improvement in the HPETC system by regulating the mass flow rate of HTF with the change in climatic conditions. They recommended the use of an auxiliary heating unit in the early morning and during cloudy periods [135]. Daghigh et al. [38] analyzed the performance of the HPETC system experimentally. They reported the maximum water outlet temperature of 64°C between 3:00 and 4:00 PM. Moreover, they also recommended the use of an auxiliary heating system from early morning until 2:00 PM [38].

The use of an auxiliary heating system can be avoided by integrating a low-cost latent heat based thermal storage unit within the HPETC system [107, 137]. Among the various types of heat energy storage techniques, PCM based latent heat storage systems have shown enormous benefits due to higher thermal energy density during the phase

change process and nearly isothermal heat storage/release capabilities [73,134,140]. Essa et al. [48] performed an experiment on HPETC integrated with paraffin wax. To improve the heat transfer between PCM and HP they have used helically finned HP and compared its performance with a conventional system. They observed uniform temperature distribution along the tube axis with the maximum temperature difference of 4°C for the helically finned HP integrated system, while the conventional system showed a difference of 12.25°C. Besides, the system with helical fin achieved a maximum thermal efficiency improvement over the conventional system by 15%. Moreover, they observed a delay in the melting process of PCM by 60 min compared with the conventional one [48]. Chopra et al. [30] investigated the performance of HPETC system experimentally. They compared the performance between the conventional system and PCM integrated system. They used PCM SA-67 with a melting point of 67° and thermal energy storage capacity of 244.21 kJ/kg. They reported the maximum thermal efficiency of 87.80% for the HPETC system with PCM and 55.46% for without PCM [30]. Li et al. [89] conducted an experimental and numerical analysis of HPETC integrated with nano-enhanced PCM (NEPCM). They achieved the energy storage efficiency of 40.17% after adding 3 wt% expanded graphite into the PCM [89]. In another experimental study, Li et al. [90] used the same composition of NEPCM, and replaced the heat pipe with a copper tube using water as a heat transfer fluid. This new configuration showed the energy storage efficiency of 39.98% [90]. Instead of integrating PCM inside the glass tubes, Naghavi et al. [108] utilized the manifold as a thermal storage unit. In their design, first, they stored heat into the PCM filled manifold unit then transferred it to the working fluid flowing through the manifold.

They have added fins to the heat pipe head to improve the heat transfer inside the PCM. They reported the maximum thermal efficiency of 42% during sunny days and 36% during cloudy/rainy days [108]. Chopra et al. [33] used stearic acid as a PCM, filled inside the manifold. They reported the maximum thermal efficiency of 72.52% with a mass flow rate of 24 LPH [33]. Wu et al. [168] analyzed the performance of HPETC with and without PCM. They observed that the system with PCM has 30% less fluctuation in collecting efficiency compared to the system without PCM. Moreover, during night time they found that solar collector system with PCM has higher outlet temperature in comparison to the system without PCM [168]. Wang et al. [166] performed an experimental study to analyze the impact of different climate, temperature of air at inlet and mass flow rate of air on thermal efficiency of PCM based HPETC system. The result of their study showed the maximum power output of 1.26 kW at mass flow rate of 240 m^3/h with inlet temperature of 15 °C. They also reported the heat storage efficiency of 67.5% and heat release efficiency of 98.5% [166].

The previous literature reveals performance improvement of HPETC system through several techniques including: optimizing mass flow rate of air/water at manifold [32, 54], varying methods of heat extraction from the glass tube [3, 47, 48, 90], by replacing HTF inside the HP [115, 170], by using different absorber coating [70, 145], and different climatic conditions [142, 152]. On the other hand, integration of PCM with HPETC system has shown enormous benefits such as uniform temperature distribution inside the glass tube [16], less heat loss by storing the excess heat inside the PCM [130, 153], and

higher outlet temperature of HTF. The previous literature investigates the performance of an HPETC under different weather conditions or by changing different optimization parameters. As per the authors' knowledge, until now, no one has studied the performance enhancement of HPETC by reconfiguration of the HP and its effect on the melting process of the PCM.

In this study, the performance of a HPETC integrated with energy storage materials, namely phase change materials (PCMs), is investigated under two different modes of an operation, normal and on-demand. In phase-I, effect of HP position; and phase-II, the effects of various energy storage materials are investigated. In conventional HPETCs, the HP is installed inside the glass tube adjacent to the upper surface, fixed in-place by an aluminum fin, while in current study, the heat pipe is reconfigured to be in the center of the tube. The performance of the modified HPETC is compared with conventional collector.

3.2 Numerical modeling

3.2.1 Physical model

Figure 21 left depicts the position of heat pipe in conventional and right shows the cross-sectional view of proposed HPETC in this study. The tritriacontane paraffin ($C_{33}H_{68}$) is selected as PCM in phase-I of this study. Table 7 shows the physical parameters of HPETC. The preliminary analysis on the effectiveness of tritriacontane paraffin is performed in the previous work of the authors [118], which shows this type of PCM is a good candidate for the operating condition of the system while showing high storage

heat capacity. In order to investigate the effect of HP position on phase change process of PCM, two distinct three-dimensional models as shown in Figure 21 (a) and (b) are generated using ANSYS design modeler.

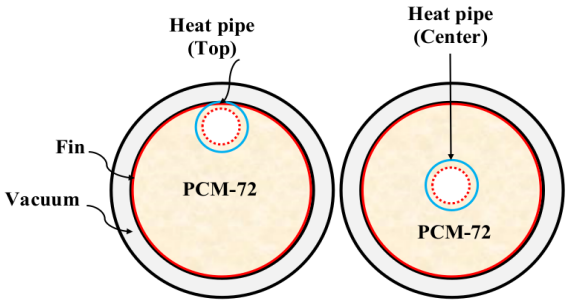

Figure 21: Cross-sectional view of proposed HPETC.

The solar radiation is allowed to pass through the outer glass tube by defining it as a semi-transparent wall with 80% transmissivity, while the opaque wall of an inner tube is defined with absorptivity of 92%. The heat conductive fin made from the aluminum is defined as a shell conduction layer with 0.2 mm thickness [118]. Physical dimensions and thermal properties of the HPETC are shown in Table 6. The main purpose of the heat pipe is to remove the accumulated heat from the PCM filled tube to the water manifold. Heat pipes have potential to conduct huge amounts of heat energy through a smallest possible cross-section area over a considerable length without any extra power input.

Furthermore, the HP's have very high heat conductivity compared with any other metals [52, 156]. However, It is very difficult and requires high computational cost/time to simulate the evaporation and condensation phenomenon inside the HP. Therefore, in

Table 6: Physical parameters & thermal properties of the HPETC [118].

Parts	**Properties**	
Glass tubes	Outer diameter (m)	0.058
	Inner diameter (m)	0.047
	Tube thickness (m)	0.0018
	Tube length (m)	1.80
	Density (kg/m^3)	2230
	Heat capacity (J/kg-K)	980
	Conductivity (W/m-K)	1.140
Aluminum fin	Fin length (m)	1.80
	Density (kg/m^3)	2699
	Heat capacity (J/kg-K)	900
	Conductivity (W/m-K)	210
Heat pipe	Length of Evaporator (m)	1.730
	Dia. of evaporator (m)	0.008
	Length of condenser (m)	0.045
	Dia. of condenser (m)	0.020
	Density (kg/m^3)	8978
	Heat capacity (J/kg-K)	381
	Thermal conductivity (W/m-K)	38000

this numerical study, the HP is considered a high thermal conductive device. Legierski et al. [87] performed a CFD simulation to investigate the conductivity of a HP filled with water as working fluid. They also validated CFD results with experiment using thermographic camera and contact thermometers. The maximum value of thermal conductivity they reported was 30,000 W/m-K While, Thyrum [154] and El-Nasr [44] recommended the higher values of 50 kW/m-K and 100 kW/m-K, respectively. In authors' initial CFD modeling of HPETC, the value of the effective thermal conductivity of 30 kW/m-K showed a good agreement with experimental measures [51, 97, 118].

In phase-II, apart from tritriacontane paraffin, two other types of sugar alcohol(SA)

based PCMs, namely, xylitol, and erythritol with melting temperature of 90° and 118° and latent heat capacity of 238 kJ/kg and 316 kJ/kg, respectively are selected to be compared with tritriacontane paraffin. The choice of PCMs is made based on low-to-medium temperature applications. The selected PCMs are low-cost and non-toxic, non-corrosive, non-flammable and easily available. Despite this, SAs possesses high latent heat capacity, high specific heat, high thermal conductivity [30, 42, 68] and great chemical and thermal stability [139, 147]. Thermal properties of the energy storage materials (PCMs) used in this study are represented in Table 7.

Table 7: Thermophysical properties of selected PCMs [15, 42, 68, 95, 164].

Property	**Tritriacontane paraffin**	**Erithrytol**	**Xylitol**
Chemical Formula	$C_{33}H_{68}$	$C_4H_{10}O_4$	$C_5H_{12}O_5$
ρ (S-L) (kg/m^3)	810-765	1440-1289	1505-1345
c_p (S-L) (J/kg-K)	870-1110	1340-2870	1270-2730
k (W/m-K)	0.21	0.33	0.36
H (kJ/kg)	256	316	238
μ (kg/m-s)	0.026	0.031	0.62
$T_{Solidus}$ (K)	339	333	353
$T_{Liquidus}$ (K)	345	391	363

3.2.2 Boundary conditions

The commercially available CFD tool ANSYS-Fluent 2020R2 is utilized for the unsteady simulation of HPETC. The simulation analysis is performed in two operation modes. In normal operation, heat is extracted from the inner glass tube via HP by circulating water through the manifold with constant flow rate of 45 LPH, while the surplus

solar/heat energy is stored by the PCMs in the form of latent heat. Conversely, in stagnation mode (on-demand), the HPETC system is exposed to the solar radiation while no water circulation (forced cooling effect) is allowed. As the result, the HPETC system absorbs solar radiation during the day, stores the heat energy inside the PCM (through phase-change process) which can be used at night time to fulfill the hot water demand in evening peak hours. The simulations are performed with a mounting angle of $45°$. The weather data for Kansas City, MO USA (39.0997 °N, 94.5786 °W) is obtained from the national solar radiation database (NSRDB [131]) which is shown in Figure 22.

The amount of useful heat gain by the collector is calculated using Eq.3.1 [93] and applied as a polynomial function in solar load model. Table 8 depicts the applied boundary conditions in this study. All the simulations are performed with the same unsteady solar radiation boundary condition which allows for thermal performance comparison in Phase-I and Phase-II. In addition, to enhance the accuracy of the model, temperature dependent thermophysical properties given in Table 7 are defined as a piecewise-linear interpolation formula.

$$\dot{Q}_{useful} = \dot{Q}_{in} - \dot{Q}_{loss} \tag{3.1}$$

where $\dot{Q}_{loss}$ is heat loss defined with a constant value of 0.8 $\mathrm{Wm^{-2}K^{-1}}$, as suggested by Apricus [14], and $\dot{Q}_{in}$ is total absorbed heat energy by absorber which can be expressed as follows:

$$\dot{Q}_{in} = \tau_{og}\alpha_a G_t \tag{3.2}$$

where τ_{og} is the transmissivity of the outer glass tube, absorptivity of a absorber layer is α_a and G_t is the solar radiation. h_c is calculated using equation (3.3) [35], and defined at the condenser wall of a HP.

$$Nu_{Churchill} = \frac{h_c D_c}{k_l} = 0.3 + 0.62 \frac{Re^{0.5} Pr^{\frac{1}{3}}}{\left[1 + \left(\frac{0.4}{Pr}\right)^{\frac{2}{3}}\right]^{\frac{1}{4}}} \left(1 + \left(\frac{Re}{282,000}\right)^{\frac{5}{8}}\right)^{\frac{4}{5}} \tag{3.3}$$

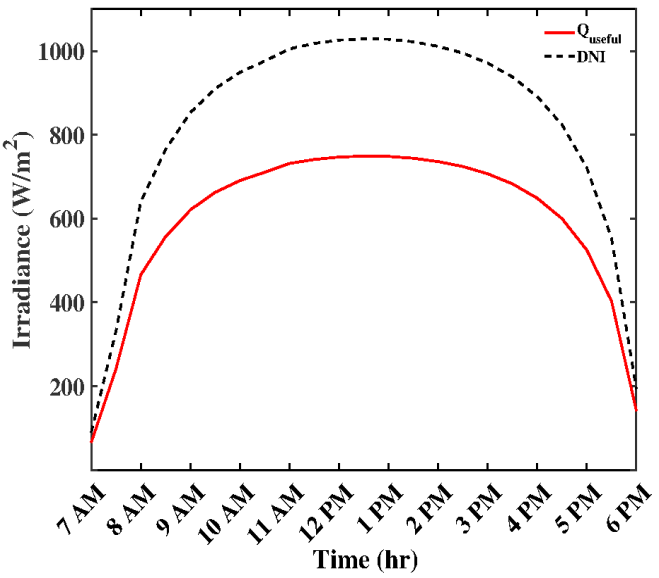

Figure 22: Solar radiation data [131].

The CFD model of an HPETC system is simplified by adopting the following outlined assumptions:

- The thermal properties of the components of the HPETC are considered as a constant value, except the density and specific heat values of the PCMs;
- The specific heat values for the PCMs are defined as a piecewise-linear polynomial function.

Table 8: Applied boundary conditions in this study.

Item	B.C. Type	Properties
Radiation model	Solar Irradiance (UDF)+ Solar ray tracing	$\dot{Q}_{useful}$ = -8.94E-24t^6 + 1.03E-18t^5 - 4.89E-14t^4 + 1.23E-9t^3 - 1.81E-5t^2 + 0.16t + 47.82
Outer glass tube		
Outer wall	Semi-transparaent wall	τ_g=0.9
Inner wall	Coupled	
Vacuum zone	Transparaent	τ=1.0, u = v = w = 0 [118]
Inner glass tube		
Outer wall	Opaque wall	α_{abs}=0.92
Inner wall	Fin	Defined as shell conduction-layer with thickness of 0.2 mm
Heat pipe		
Evaporator wall	Coupled	
Condenser wall	Heat transfer coefficient	h_c=212 W/m-K, T_∞=288 K (calculated using Eq. 3.3)
HPETC		
Top & bottom wall	Adiabatic wall	Heat flux (Q) = 0

- The effect of natural convection is applied with the help of Boussinesq approximation defined as :

  $\rho = \rho_m/(\beta(T - T_{avg.}) + 1)$ where $T_{avg.} = (T_{solidus} - T_{liquidus})/2$;

- The liquid PCM is considered as Newtonian fluid;

- The natural convective motion of the liquid PCM is considered as laminar (Ra$<$ 10^{10}) and in-compressible.

3.2.3 Governing equations

After defining all the boundary conditions, governing equations are solved for the flow-time of 86,400 seconds. The three-dimensional form of the governing equations can be written as follow:

The continuity equation:

$$\frac{\partial \rho}{\partial t} + \nabla(\rho \vec{v}) = 0 \tag{3.4}$$

where ρ & $\vec{v}$ denotes density and the velocity vector, respectively. The momentum equation is given by:

$$\frac{\partial}{\partial t}(\rho \vec{v}) + \nabla(\rho \vec{v}\vec{v}) = -\nabla p + \nabla \vec{\tau} + \rho \vec{g} + S_g \tag{3.5}$$

where p is the pressure, τ denotes the stress tensor and g is the gravitational force. The energy equation:

$$\frac{\partial}{\partial t}(\rho H) + \nabla(\vec{v}\,(\rho H + p)) = \nabla(k \nabla T + \vec{\tau}\,\vec{v}) + S_H \tag{3.6}$$

where k and H are the thermal conductivity and the total enthalpy, which can be expressed as:

$$H = h_0 + \int_{T_0}^{T} c_p \, dT + f_l \, h_{sl} \tag{3.7}$$

where h_0 and T_0 are the initial values of enthalpy and temperature. c_p denotes the specific heat capacity at constant pressure. h_{sl} and f_l are the latent heat of fusion and the liquid fraction, respectively. f_l can be calculated from [57]:

$$f_l = 0, \qquad if \quad T < T_{solidus} \tag{3.8a}$$

$$f_l = 1, \quad if \quad T > T_{liquidus} \tag{3.8b}$$

$$f_l = \frac{(T - T_{solidus})}{(T_{liquidus - Tsolidus})} \quad if \quad T_{solidus} < T < T_{liquidus} \tag{3.8c}$$

The source term S_g in Eq. (3.5) is added to consider the buoyancy forces acting on the PCM during phase change process and enthalpy-porosity model to define the phase change phenomena for the PCM [57, 159]:

$$S_g = \rho\ \vec{g}\ \beta\ (T - T_{ref}) - \frac{(1 - f_l)^2}{{f_l}^3 + \varepsilon}\ A_{mushy}\ \vec{v} \tag{3.9}$$

where, ε is a very small number (0.001) to avoid division by zero and A_{mushy} is the mushy zone constant 1.0×10^5. The detailed HP modeling and solar tracking can be found in the previous work of the authors [118].

3.2.4 Validation of Numerical model

The three-dimensional transient numerical model is validated with experimental results in the previous work of the authors [118] with average deviation of 2.04%. The validated model can be used as benchmark for further systems' investigation/improvement.

Table 9: Numerical schemes

Governing Eq.	Discretization Method	Relaxation Factor	Convergence Criteria
Pressure	PRESTO	0.3	
Momentum	Second Order Upwind	0.5	10^{-6}
Energy	Second Order Upwind	1	10^{-9}
Continuity			10^{-4}
Pressure-Velocity coupling		SIMPLE scheme	
Transient formulation		First Order Implicit	

3.2.5 Mesh

The components of the HPETC system are discretized using the patch conforming method with structured mesh, which helps to obtain better numerical stability and convergence. The discretized HPETC system with different views is represented in Figure 23.

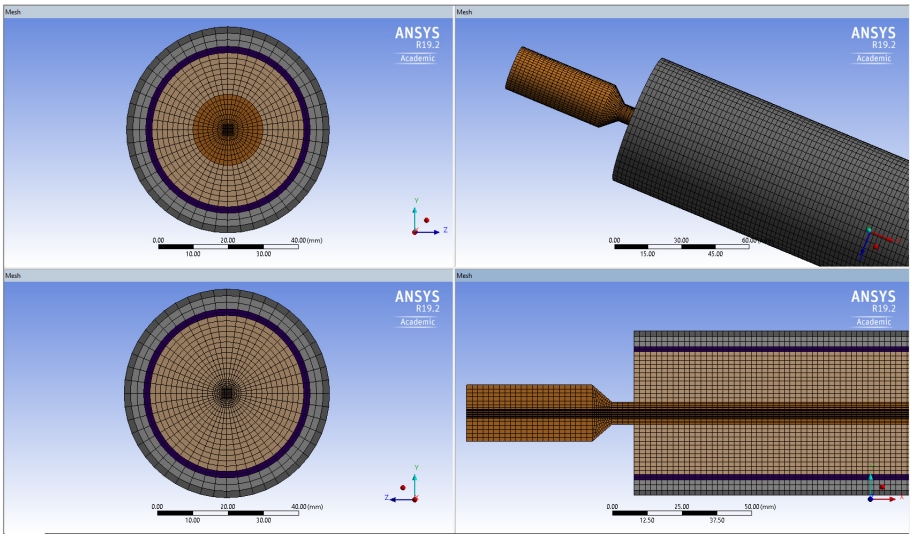

Figure 23: HPETC mesh cross-sectional views.

Three different sets of mesh with 322,342 (Coarse), 590,977 (Medium) and 878,577 (Fine) number of nodes were selected to perform the mesh independent study. Simulation is performed using time adaptive method with minimum and maximum time step size of 0.01 and 1 second, respectively (Courant number is set to 1) [118]. The volume average liquid fraction of PCM is considered to make the comparison between different mesh sizes which is illustrated in Figure 24. In which, 590,977 nodes for medium size mesh is found sufficient for the current study.

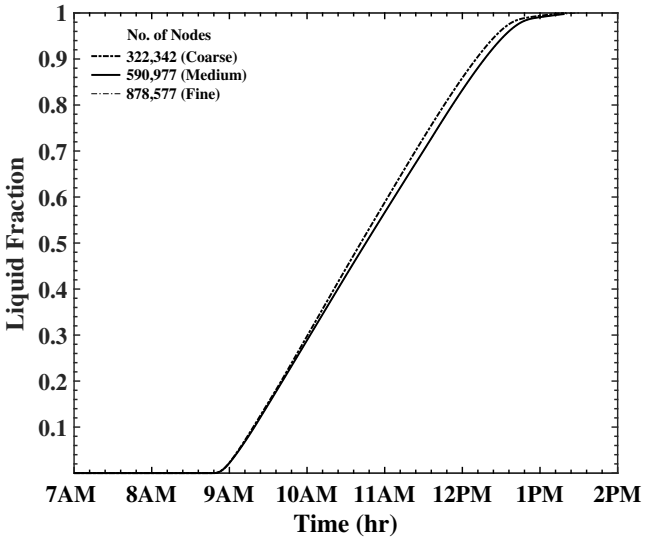

Figure 24: The grid independence test.

3.3 Results and discussion

During the simulation, the fin temperature, volume average liquid fraction of PCM and total energy stored are tracked for a flow-time of 24 hours.

3.3.1 Phase-I: effect of heat pipe reconfiguration

Figure 25 shows the volume average liquid fraction during the day-time. It is observed that the melting process of the PCM begins earlier when the HP is at the center of a glass tube, while in conventional system it is delayed by approximately 32 minutes.

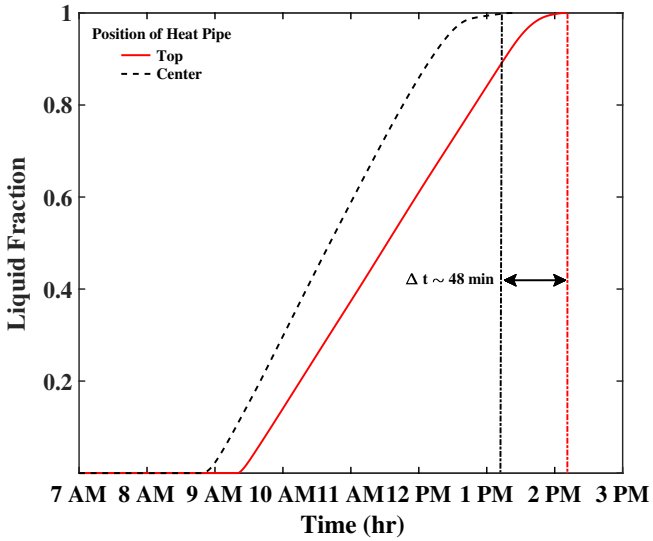

Figure 25: Phase-I: Liquid fraction rate under stagnation mode.

It should be noted that as the contact area between the PCM and fin is larger in modified geometry, compared with conventional design, thus, high heat transfer rate is achieved. In addition, solid-liquid phase change process of PCM in the optimized design is completed 48 minutes earlier than the conventional system. To investigate the influence of HP reconfiguration on natural convective flow of the liquid PCM, Liquid fraction and velocity contours are illustrated in Figure 26 and 27. During the day-time, solar radiation is available at the upper part of the glass tube, which is converted into heat energy by absorber and transferred to the PCM through the heat transfer fin. Around 9 AM, no liquid fraction is found inside the conventional tube while optimized system shows that the melting process is initiated in the vicinity of the fin. At 11 AM, in optimized system, the PCM in upper part of the glass tube is found completely in liquid state adjacent to the heat transfer fin. Conversely, conventional system shows only a heat conduction inside the PCM which

resulted in a thick layer of mushy zone.

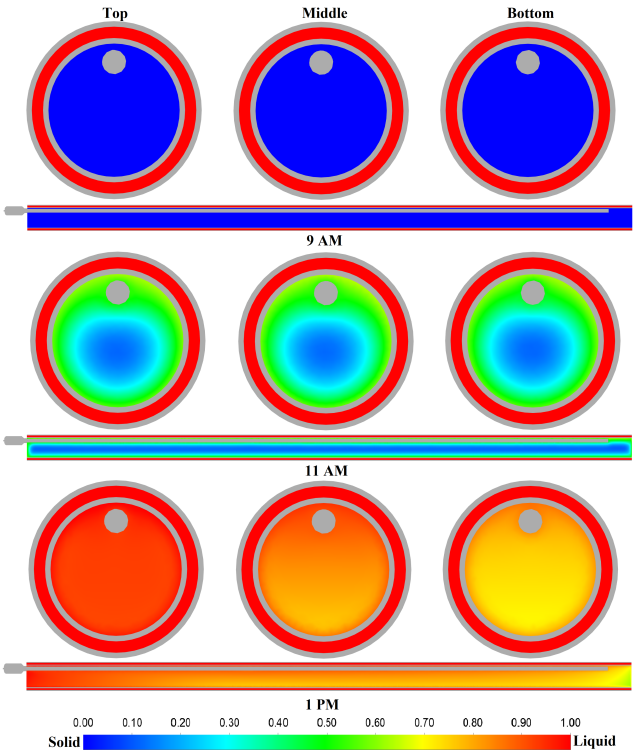

(a) Liquid fraction

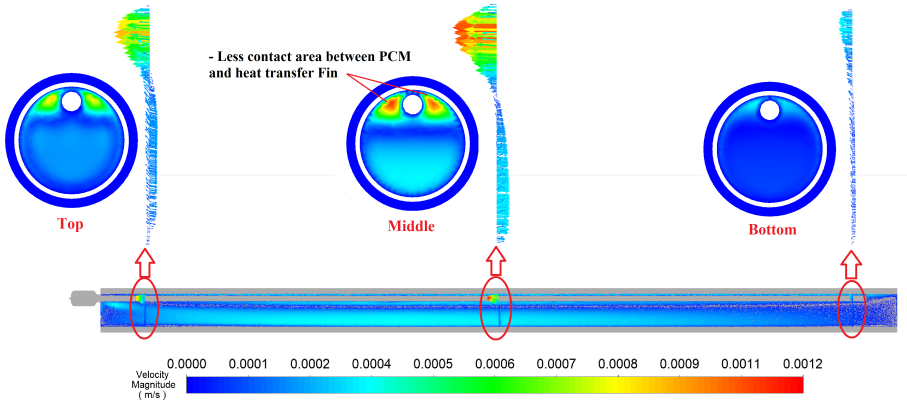

(b) Velocity contour at 1PM

Figure 26: Phase-I: (a) Liquid fraction history and (b) velocity vector for the conventional system.

Moreover, as the charging process continues, the effect of natural convection becomes stronger and liquid PCM starts flowing at higher elevation along the fin which further increases heat transfer inside the optimized tube. Liquid fraction contours in Figure 26 (a) and 27 (a), clearly exhibits the poor heat transfer inside the conventional system.

Figure 26 (b) and 27 (b) shows the velocity contours at 1 PM. The upward motion of the molten PCM along the fin occurs due to the strong buoyancy forces. In a conventional design, the HP becomes an obstacle in the natural convection flow resulting in the maximum flow velocity of only 0.0012 m/s. In contrast, the maximum flow velocity of molten PCM in an optimized design is 0.0084 m/s. This high velocity of molten PCM significantly improves the convective heat transfer resulted into a faster melting process of the PCM. The performance of the optimized HPETC system is also investigated for the normal operation to further verify the potential of HP reconfiguration in the proposed design. The comparison of an average fin temperature value over time is shown in Figure 28. The fin temperature of the HPETC system with HP reconfiguration at each time step was around 5°C higher compared with the conventional system. Moreover, the maximum liquid fraction of PCM was reached up to 98% in an optimized system where the conventional system reached up to 74% only. Consequently, the HP reconfiguration yields to heat transfer enhancement of the system by keeping fin's temperature at a higher value as well as increasing the amount of latent heat storage by 24% increase in melting fraction of PCM.

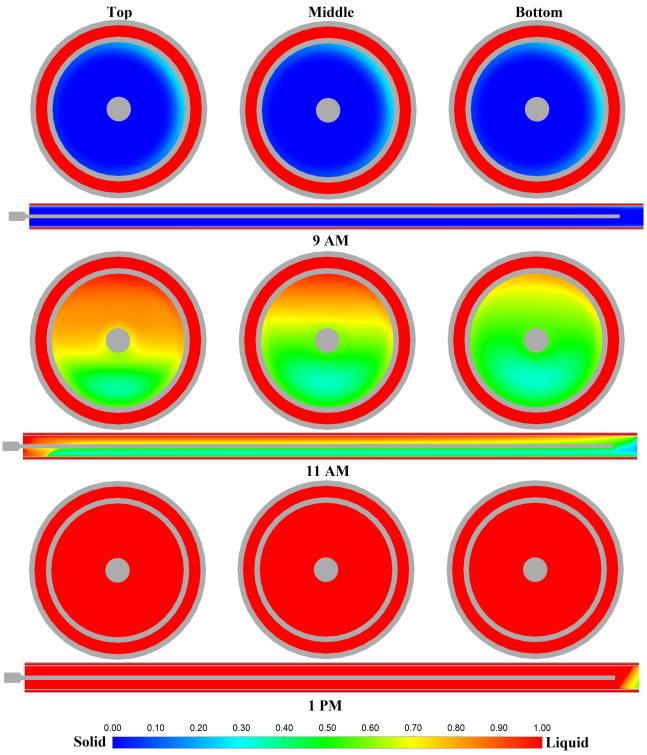

(a) Liquid fraction

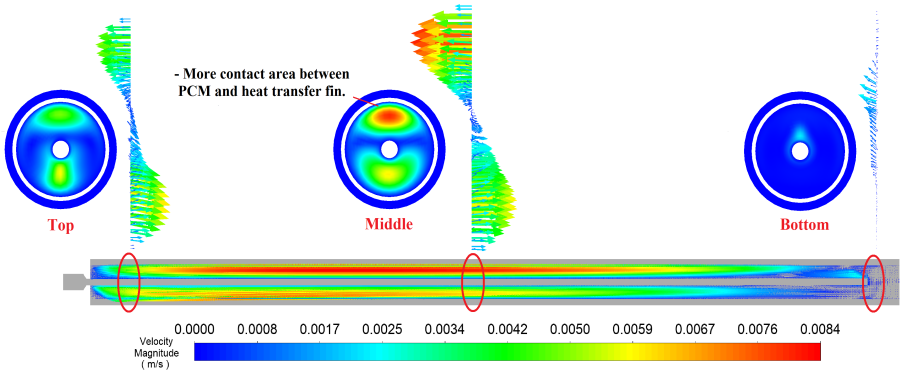

(b) Velocity contour at 1PM

Figure 27: Phase-I: (a) Liquid fraction history and (b) velocity vector for the optimized system.

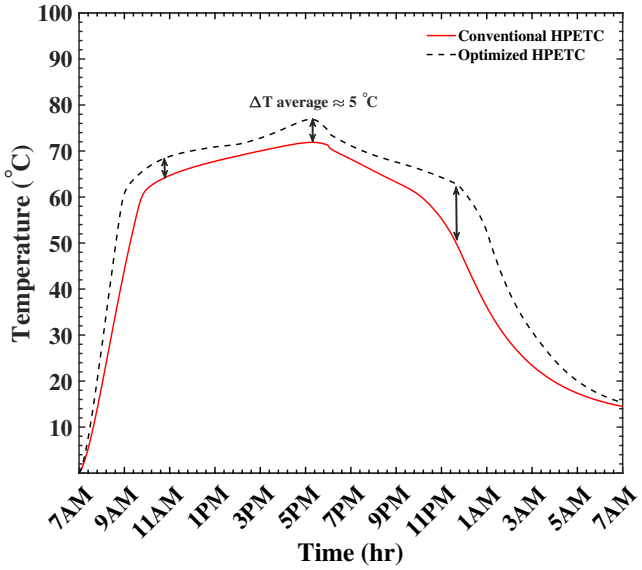

Figure 28: Phase-I: Fin temperature variation under normal operation.

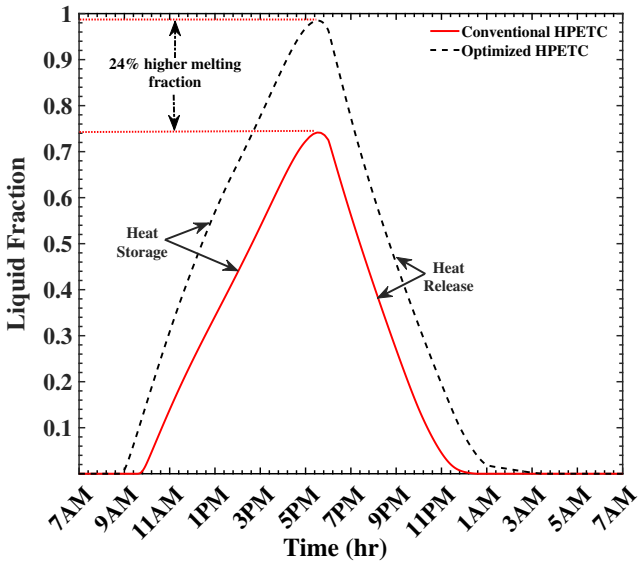

Figure 29: Phase-I: Liquid fraction rate under normal operation.

3.3.2 Phase-II:- effects of various energy storage materials

In phase-II, the optimized configuration of HP is selected for further investigation of various types of PCMs with different melting points and latent heat capacities. In normal operation, area-weighted average fin temperatures are tracked and compared between the glass tube to find a right choice of a PCM with maximum fin temperature, while to optimize the thermal energy storage capacity, volume average liquid fraction of PCMs are calculated for the 24 hours of flow-time. On the other hand, in stagnation mode, the volume average liquid fraction of PCMs are tracked until the glass tube reaches its maximum value.

3.3.2.1 Normal operation

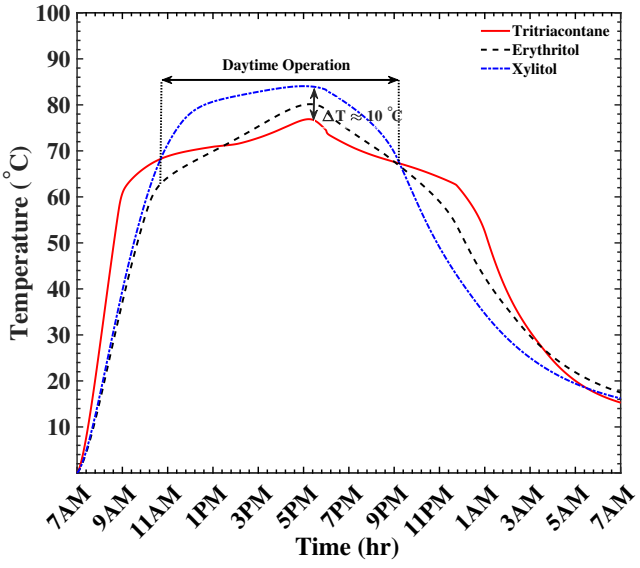

Figure 30: Phase-II: Fin temperature variation under normal operation.

The fin temperature variation over time inside the glass tube is illustrated in Figure 30 for normal operation. In the morning between 7AM to 11AM, the temperature of the fin increases linearly due to the heat conduction in a solid phase. The trend of linear increase in the fin temperature immediately changes as soon as it reaches to the melting point of the PCM. This behaviour illustrates the beginning of the PCM melting which can be observed in Figure 31. During the melting process, the fin temperature of the xylitol tube at each time step was around 10°C higher compared with the other tubes during the period of 11 AM to 7 PM. Around 5 PM when there is little or no solar radiation available, the temperature of the fin starts dropping dramatically. The HPETC system integrated with erythritol and xylitol show rapid cooling in fin temperature. In contrast, a significantly slower cooling rate is found for tritriacontane paraffin tube. This is due to the release of latent heat energy and PCM inside the glass tube starts solidifying.

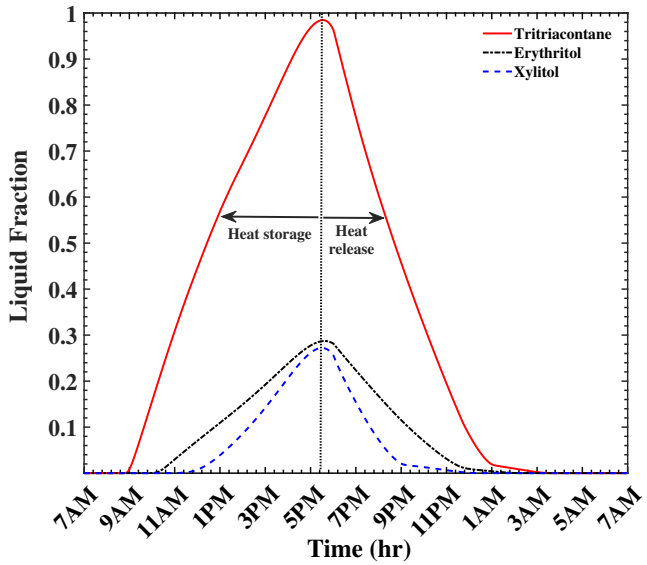

Figure 31: Phase-II: Liquid fraction rate under normal operation.

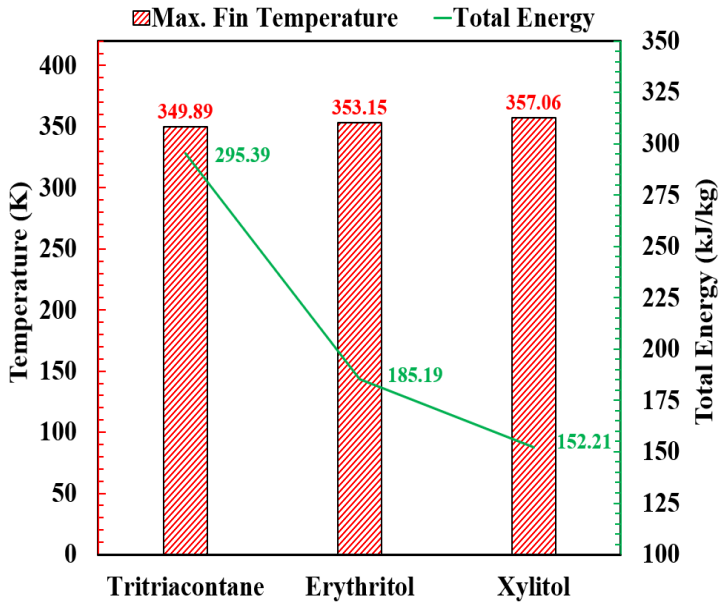

Figure 32: Phase-II: The total amount of energy stored inside the tube at maximum fin temperature under normal operation.

Figure 31 and 32 represent the volume average liquid fraction and total energy stored inside the glass tube, respectively. Under the normal operation, maximum liquid fraction and total thermal energy are achieved by tritriacontane paraffin tube with the value of 98% and 295 kJ/kg, respectively. While the system integrated with xylitol stored the least amount of total energy with the value of 152.21 kJ/kg. Despite this, the system integrated with xylitol reported the maximum fin temperature value of 357.06 K. Tritriacontane paraffin tube has stored 37.30% and 48.47% higher amount of the total energy compared with the erythritol tube and xylitol tube, respectively. The result of the normal operation shows that the maximum thermal enhancement of HPETC can be achieved by utilizing the combination of tritriacontane paraffin/xylitol PCM.

3.3.2.2 Stagnation mode

In the stagnation mode, the performance of the HPETC system is studied with no water flowing through the manifold, and during the day thermal energy is stored inside the tube to fulfill the requirement of hot water at night time. Figure 33 shows the variation in liquid fraction of PCM over time. It can be noticed that the melting process of tritriacontane paraffin begins earlier than the other two PCMs. The reason behind that is the lower values of specific heat and latent heat energy of tritriacontane paraffin. Erythritol and xylitol have 35% and 31% higher specific heat capacity compared with tritriacontane paraffin.

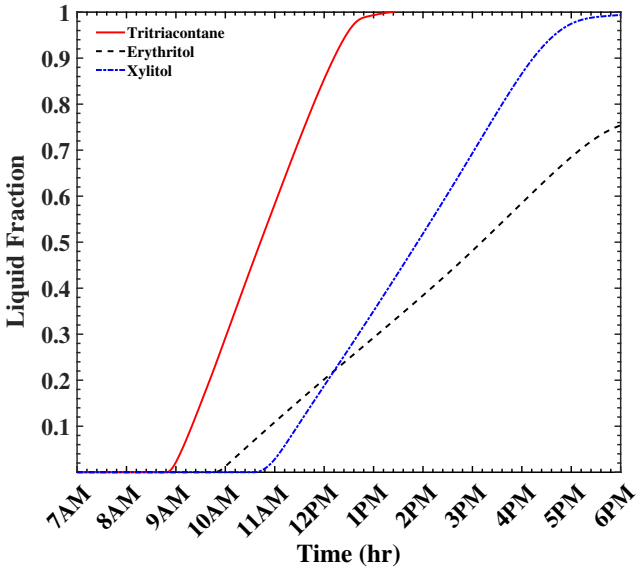

Figure 33: Phase-II: Liquid fraction rate under stagnation operation.

Furthermore, it should be noted that erythritol has high specific heat capacity compared with xylitol, even though the melting process begins early in erythritol tube due to the lower value of solidus temperature. Solidus-melting starts around at 10AM for erythritol,

while the xylitol tube shows the beginning of a melting process around 11AM. The system integrated with tritriacontane paraffin completes the charging process around 1 PM, while erythritol and xylitol take the whole day to reach the melting fraction of 68% and 98%, respectively. Figure 34 depicts the value of maximum fin temperature and total energy stored inside the tube when the maximum liquid fraction inside the tube is achieved.

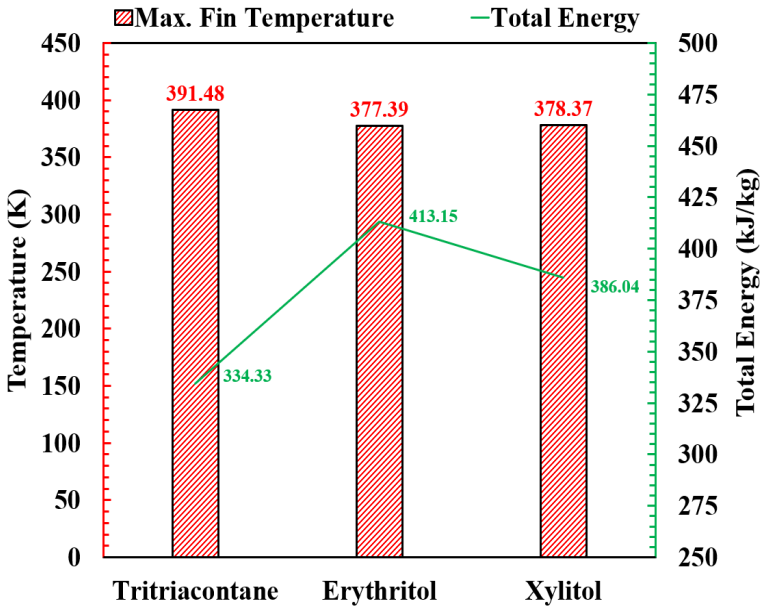

Figure 34: Phase-II: The total amount of energy stored inside the tube at maximum fin temperature under stagnation operation.

The tritriacontane paraffin tube obtained the maximum fin temperature of 391.48 K with a total energy storage of 334.33 kJ/kg, while the erythritol tube has stored the maximum thermal energy of 413.15 kJ/kg. The result of the stagnation mode shows that the maximum thermal enhancement of HPETC can be achieved by utilizing the combination of tritriacontane/erythritol PCM.

3.4 Summary of this research work

The performance of an HPETC is optimized in two phases, where phase-I is focused on the effect of HP position in stagnation (on-demand) operation, and in phase-II, the effects of various energy storage materials in both normal and on-demand operation are investigated. In phase-I, under stagnation mode, results show that the solid-to-liquid phase change process was expedited by 48 minutes when the HP shifted from the top to the center of the glass tube. On the other hand, during normal operation, the maximum liquid fraction of PCM was reached up to 98% in an optimized system where the conventional system reached up to only 74%. The results of the stagnation and normal operation exhibit the significance of HP position on melting process of PCM and its effect on latent heat thermal energy storage system. In phase-II, the optimized configuration of the HP is selected for further investigation of various types of PCMs with different melting points and latent heat capacities. In normal mode, the HPETC system integrated with tritriacontane paraffin exhibited total energy storage of 295 kJ/kg per tube at a water mass flow rate of 45 LPH, however, the fin temperature of the tube integrated with xylitol at each time step was around 10°C higher compared with the other tubes during the daytime due to its high specific heat capacity. In the stagnation mode, erythritol shows maximum thermal energy storage of 413.15 kJ/kg per tube, however, the tube integrated with xylitol shows higher fin temperature at each time step. Consequently, the utilization of tritriacontane paraffin/xylitol in normal operation and erythritol/xylitol in on-demand operation is recommended to enhance the system's thermal performance.

CHAPTER 4

EFFECT OF HIGH CONDUCTIVE POROUS MEDIA IN ENERGY STORAGE BASED HPETC: AN EXPERIMENTAL STUDY

This research work is under preparation to be published as a peer reviewed journal article.

4.1 Introduction

The phase change materials are capable of storing ample amount of heat in the form of latent heat [86]. Compared to the sensible heat, latent heat thermal energy storage (LHTES) offers higher energy density, wide operating range and iso-thermal operation [67, 72]. For instance, the energy required to melt 1 kg of KNO_3 (latent heat) is 95 times higher compared to the energy required to raise the temperature of 1kg of KNO_3 by 1 K (sensible heat). Thus, LHTES requires less volume to store small quantity of PCM which can store heat energy almost 100 times of sensible heat [113]. Due to having different characteristic properties of PCM, right choice of the PCM is inevitable in the application of solar thermal energy storage. Some of the important properties for selection of PCMs are summarized below:

- Melting point in the desired operating temperature,
- High latent heat of fusion per unit mass, so that a smaller amount of material can store a given amount of energy,
- High specific heat to provide additional significant sensible heat storage effects,

- High thermal conductivity, so that the temperature gradients for charging and discharging the storage material are small,
- Small volume changes during phase transition,
- Little or no sub-cooling during freezing,
- Chemically stable,
- Contains non-poisonous, non-flammable and non-explosive elements/compounds,
- Available in large quantities at low cost.

There is no single PCM that possesses all the properties mentioned above. Moreover, PCM exhibits some undesirable characteristics that hinders their performance in latent heat storage. The most affected undesirable characteristic is the low thermal conductivity, which affects the charging and discharging rate and leads to poor performance of the thermal energy storage system. The lower thermal conductivity can be manifested during the energy absorption (melting; charging) and energy retrieval (solidification; discharging) processes [75]. The issue of poor thermal conductivity can be addressed by either increasing thermal conductivity of the PCM or by increasing heat transfer area. The thermal conductivity of the PCM can be increased by adding high thermal conductive nano-particles such as Cu, Al, Al_2O_3, TiO_2, graphite, and carbon nano-tube [53, 99]. Besides, heat transfer between the PCM and heat transfer fluid (HTF)/heat source can be achieved by employing extended surface/fins [85, 100, 101] or by integrating high conductive porous metals [61, 77]. Agyenim et al. [7] experimentally studied the effect of circular and longitudinal fins on the heat transfer enhancement inside the PCM stored in

horizontal concentric cylinder. In their experimental study, they used Erythritol as a PCM with melting temperature of 118° C. They recommended the system with longitudinal fins showed improved results in comparison with circular fins [7]. Rathod et al. [123] experimentally examined the heat transfer augmentation by employing longitudinal fins to the shell and tube type LHTES unit. The shell and tube heat exchanger with fins reported 24.52% and 43.6% decrease in melting and solidification time in comparison with system without fins, respectively [123]. In addition, Rathod et al. [117] also investigated the effect of eccentricity (displacement of inner tube in upward direction or downward) on melting and solidification time. The experimental results showed that the shell and tube heat exchanger with inner tube eccentricity of 10 mm and 3 mm is most efficient with 27.63% and 12.82% reduction in melting and solidification time [117]. Yang et al. [171] experimentally and numerically investigated performance of the metal foam composite phase change material for cold storage application. The result showed 87.5% and 76.7% decrease in solidification time with metal foam porosity of 0.93 and 0.97 compared with pure water, respectively [171]. Chen et al. [29] numerically investigated performance of a concentric type latent heat storage unit. They used paraffin as a PCM and Cu metal foam is used to increase heat transfer between HTF and PCM. The result showed reduction in melting time by 40% compared with the LHTES system with only PCM [29].

In order to improve thermal conductivity of the PCM, Mahdavi et al. [97] numerically investigated effect of high thermal conductive nano-particles on phase change process of shell and tube type LHTES system. They examined effect of adding different volume

fraction of AlO, Cu, CuO and silver nano-particles to the PCM. The results showed maximum decrease in melting time by 5.5% and 13.5% with addition of 2% and 5% volume fraction of Cu nano-particles, respectively compared with system with pure PCM [97]. Mahdi et al. [98] assesed thermal performance by dispersing alumina nano-particles to the triplex-tube LHTES system. They observed that by adding 3% and 8% volume fraction of nano-particles to the PCM can decrease solidification time by 20% and 8%, respectively compared with pure PCM [98]. Verma et al. [141] experimentally investigated thermal performance of SiO_2, Al_2O_3 and MgO based nano-enhanced PCM (NEPCM). They analyzed thermal performance of NEPCM based LHTES system by comparing melting and solidification time with pure PCM based LHTES system. Experimental results showed increased in melting rate by 33.8%, 33.8% and 41% for Aluminum oxide, magnasium oxide and silicon dioxide, respectively. In addition, solidification rate is also increased by 19.6%, 25% and 30% for Aluminum oxide, magnasium oxide and silicon dioxide, respectively [141]. Dhaidan et al. [43] extensively reviewed the effect of dispersed nano-particles on thermal performance of LHTES system. They observed remarkable improvement in LHTES system by adding nano-particles to the PCM [43]. Despite of many advantages, there are some challenges associated with dispersion of nano-particles into the PCM such as:

- Reduction in thermal energy storage capacity by adding high volume fraction of nano-particles [20, 97],
- Increase in viscosity of liquid PCM, which adversely affects on natural convection [20, 43],

- Stability of the nano-particles [43, 129],
- Agglomeration and sedimentation of nano-particles [43, 149],
- Time consuming and involves many steps such as stirring and sonication [106, 143],

Due to above mentioned disadvantages of nano-particles, In this experimental study, Cu porous metal (metal foam) with thermal conductivity value of 390 W/m-k is used to increase effective thermal conductivity of the PCM. In chapter 3, Tritriacontane paraffin ($C_{33}H_{68}$) is utilized for thermal energy storage which has thermal conductivity value of only 0.21 W/m-k. Following equation can be used to calculate effective thermal conductivity of Tritriacontane paraffin + Cu Porous [110],

$$\lambda_{eff} = \frac{\sqrt{3}}{2}[R_a + R_b + R_c]^{-1} \tag{4.1}$$

where λ_{eff} is effective thermal conductivity of Tritriacontane paraffin + Cu Porous, while the values of constant used in Eq. 5.13 can be calculated by following equations,

$$R_a = \frac{0.09\psi}{\lambda_{PCM} + \frac{1}{3}(1+\psi)(\lambda_{por} - \lambda_{PCM})} \tag{4.2}$$

$$R_b = \frac{0.91\psi}{\lambda_{PCM} + \frac{2}{3}\psi(\lambda_{por} - \lambda_{PCM})} \tag{4.3}$$

$$R_c = \frac{\frac{\sqrt{3}}{2} - \psi}{\lambda_{PCM} + \frac{0.12}{\sqrt{3}}\psi(\lambda_{por} - \lambda_{PCM})} \tag{4.4}$$

$$\psi = \frac{-0.09 + \sqrt{0.0081 + \frac{2\sqrt{3}}{3}(1-\epsilon)[2 - 0.09(1 + \frac{4}{\sqrt{3}})]}}{\frac{2}{3}(1.91 - \frac{0.36}{\sqrt{3}})} \tag{4.5}$$

The effective thermal conductivity value of 6.83 is found for Tritriacontane paraffin + Cu Porous, which is 32 times higher than the conductivity of pure Tritriacontane paraffin. In addition, Cu porous metal used in current experiment has porosity of 98% and pore density of 110 pores per inch. To the best of the author's knowledge, no one has studied the performance of heat pipe evacuated tube solar collector (HPETC) integrated with Tritriacontane paraffin + Cu Porous metal experimentally.

In this experimental analysis, two large scale HPETC systems are used to demonstrate viability of the proposed approach in commercially available HPETC system. Both HPETC systems consist of same number of evacuated tube to keep the absorber area same (two evacuated tubes on each system). In one HPETC system, two empty evacuated glass tubes are installed without any PCM (conventional system). On the other hand, second HPETC system is also equipped with two evacuated galss tubes, one evacuated tube is filled with Tritriacontane paraffin while the second evacuated tube is filled with Tritriacontane paraffin + Cu porous metal. The same quantity of PCM is used to fill both evacuated tubes (0.75 kg in each tube). The thermal performance of proposed HPETC system is compared with conventional HPETC system. The thermal performance of each system is assessed based on the variation of fin temperature, outlet water temperature and thermal efficiency of HPETC system.

4.2 Experimental study

4.2.1 Preparation of thermal bags filled with PCM and Cu porous metal

During melting process volume of the PCM expands while contraction of PCM occurs during solidification process. The evacuated glass tube may get damage/break due to cyclic expansion and contraction of PCM during phase change process [116]. To prevent evacuated tubes from any damages, aluminum bags are used to store the PCM. Firstly, PCM is melted in pyrex glass container, after that molten PCM is pored inside aluminum bags. Besides, to prepare aluminum bags with Tritriacontane paraffin + Cu porous metal, following procedures are carried out:

1. Prepare the spiral shaped metal foam and place inside the thermal bags,
2. Melt and pour PCM into thermal bags,
3. Keep the thermal bags (with molten PCM + Porous metal) inside the vacuum box,
4. Once the PCM solidifies, the other end of the thermal bag was sealed and then placed inside the evacuated glass tube.

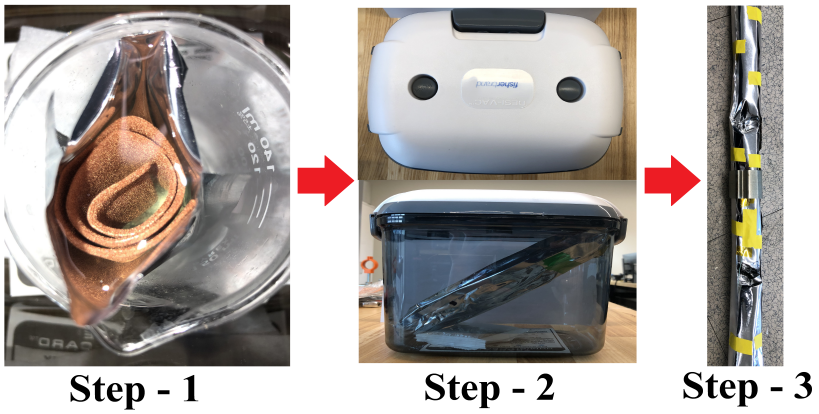

Figure 35: Procedure for thermal bags preparation.

Table 10: Physical parameters & thermal properties of the HPETC [118].

Parts	**Properties**	
Tritriacontane ($C_{33}H_{68}$)	Density(l) (kg/m^3)	782
	Density(s) (kg/m^3)	810
	Heat capacity(l) (J/kg-K)	1110
	Heat capacity(s) (J/kg-K)	870
	Melting point °C	72
	Latent heat of fusion (kJ/kg)	256
	Conductivity (W/m-K)	0.21
Cupper porous metal	Porosity	95%
	Pore density (PPI)	110
	Pore diameter (m)	1.5×10^{-4}
	Conductivity (W/m-K)	385

Figure 35 show the steps for preparing the thermal bags consist of PCM and Cu porous metal. In this experimental study, thermal performance of HPETC system is further enhanced by integrating PCM with high thermal conductive Cu porous metal.

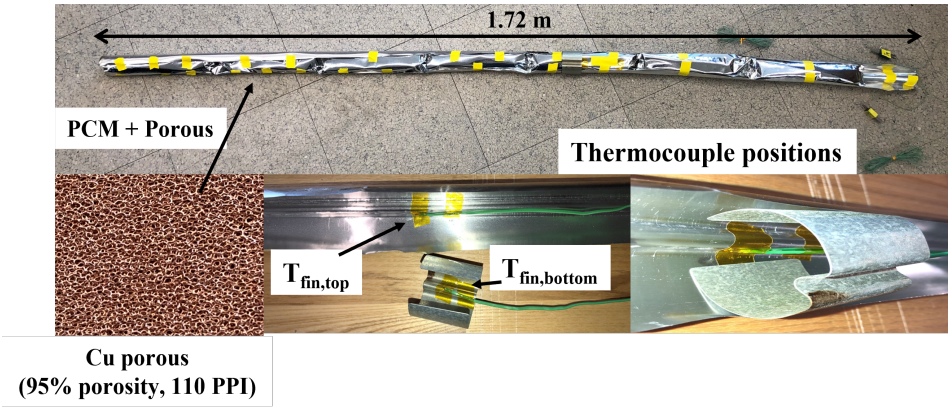

Figure 36: Thermal bags filled with PCM and arrangements of thermocouples.

During the experiment, Tritriacontane paraffin with melting temperature of 72 °C is selected as a PCM. Thermophysical properties and physical parameters of PCM and Cu

porous are listed in Table 10. In order to investigate the thermal performance of different evacuated glass tubes, several K-type thermocouples with accuracy of ± 2 °C are placed inside the tube (attached with aluminum fin). Figure 36 shows the arrangement of aluminum bags filled with PCM/PCM + Cu porous and thermocouples.

4.2.2 Description of the Apparatus

In order to perform the experiment, two standard size HPETCs are used to demonstrate the proposed approach in commercially available glass tube solar water heaters. Thermal performance of the HPETC system integrated with PCM + Cu porous is compared with the conventional HPETC system.

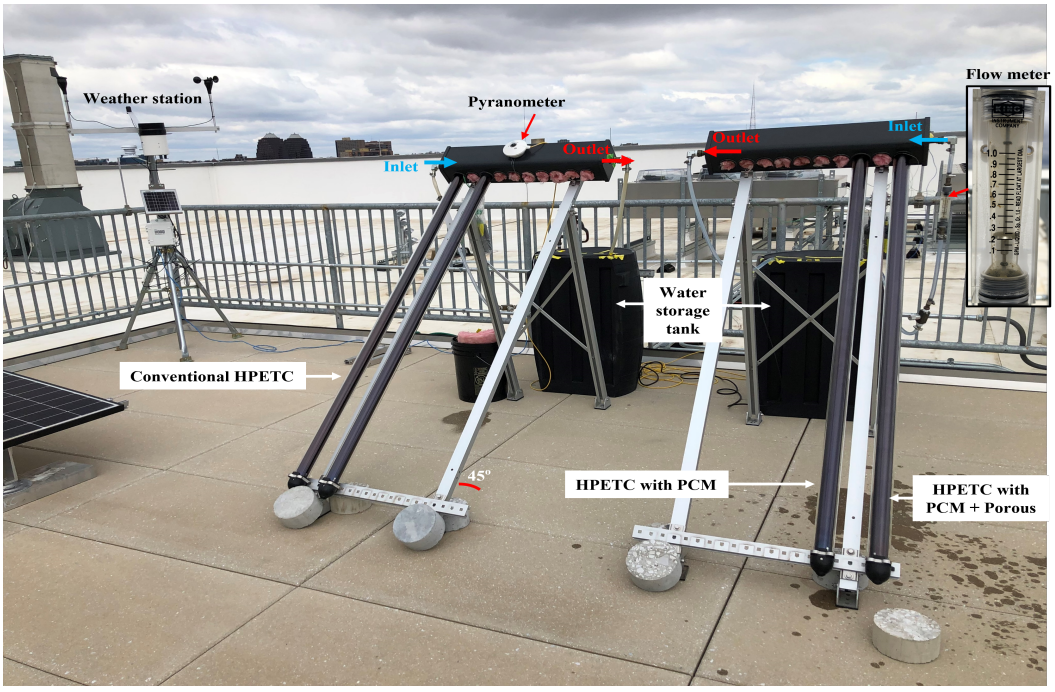

Figure 37: Experimental apparatus.

Figures 37 and 38 shows the experimental setup. The HPETC system shown on the left

is the conventional collector, while the other HPETC system contains one evacuated tube filled with PCM and second tube filled with PCM + Cu porous metal.

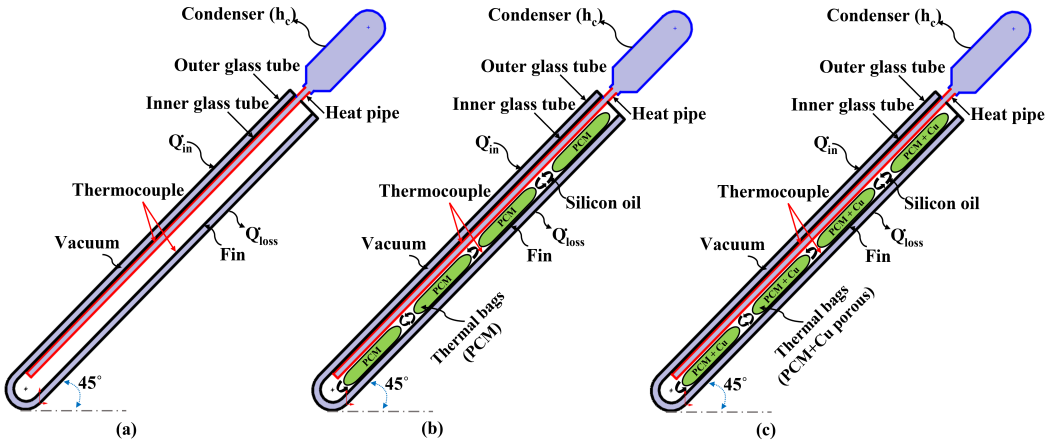

Figure 38: Schematic for different configuration of HPETC system (a) Conventional HPETC (b) HPETC integrated with PCM and (c) HPETC integrated PCM + Cu porous metal.

COMPONENT MATERIALS

Component	Material Specifications
Evacuated Tubes	**Material:** Borosilicate 3.3 **Tube style:** Twin wall all glass **Dimensions:** ø58mm outer tube; ø47mm inner tube; 1.8m length, 1.8mm outer tube wall thickness **Absorber Material:** Selective coating **Absorptance:** >93% (AM1.5); **Emittance:** <8% (80ºC) **Vacuum:** P<5x10^{-3} Pa; **Heat loss:** <0.8W/(m^2 ºC)
Heat Pipes	**Material:** High purity "oxygen free" copper (ASTM: C10200; DIN: OF-Cu) **Working fluid:** non-toxic liquid (Apricus' proprietary mixture) **Maximum heat transfer capacity:** 220W **Operating angle:** 20-80º **Startup temperature:** ~30ºC
Copper Header Pipe	**Material:** Copper (ASTM: C1100, DIN: ECu-58); **Brazing rod material:** BAg45CuZn (Potable water certified) **Maximum pressure:** 800kPa / 116psi **Connection options:** 3/4"M NPT; 3/4" SWEAT; 3/4"M BSP; 1/2"M BSP ELBOW
Heat Transfer Fins	**Material:** High purity aluminium
Rubber Components	**Material:** HTV Silicone Rubber (UV stabilized)
Mounting Frame	**Material:** 6005-T5 Aluminium Alloy with Anodized Finish (Stainless Steel frame available upon special request)
Tube Clips	**Material:** 316 Stainless Steel
Fasteners	**Material:** 316 Stainless Steel
Manifold Casing	**Material:** 3003 Aluminium with PVDF coating.
Manifold Insulation	**Material:** Glass Wool (<0.043W/mK) **Thickness:** Average >50mm

Figure 39: Geometrical parameters and materials specifications of each component of HPETC.

Dimensions and materials specifications of each component are listed in Figure 39 [14]. The experiment is performed on three consecutive days (April 9-11, 2022). Both the collectors are installed at same mounting angle of 45° and with two evacuated glass tubes on each system. In addition, submersible pumps are kept inside the 40 L capacity of the water storage tank for the continues supply of the water. The mass flow rate of water is kept constant at 0.0126 kg/s for both HPETC system. Flow meter (accuracy:$\pm$ 6% full scale flow, repeatability: $\pm$ 3% 50mm scale) is used to measure the mass flow rate.

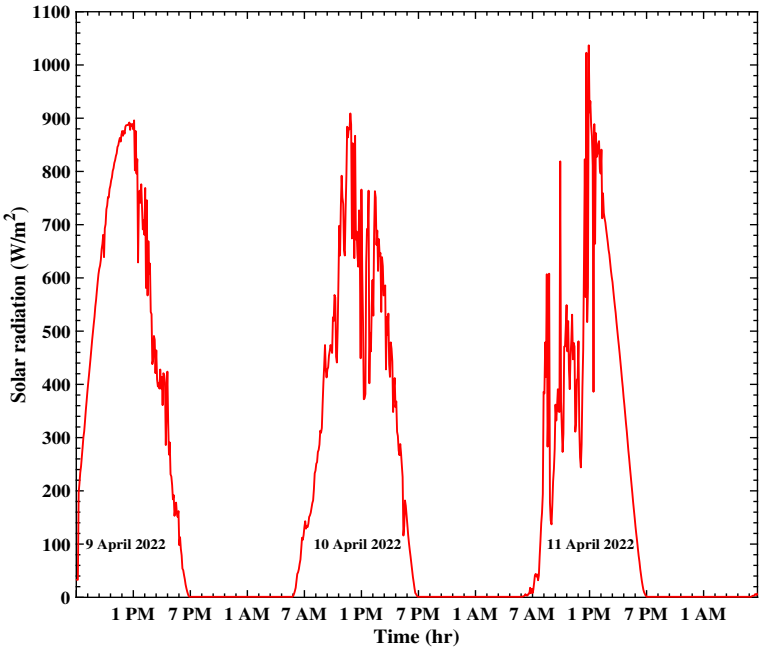

Figure 40: Solar radiation.

Moreover, weather data such as solar radiation, wind velocity, and ambient temperature are measured using weather station (Pyranometer: directional response accuracy $\leq$10 W/m^2, temperature sensor: accuracy $\pm$ 0.2° C and Anemometer: accuracy $\pm$1.1 m/s). Figure 40 illustrates the value of solar radiation recorded on April 9-11, 2022 (when the

experiment was performed).

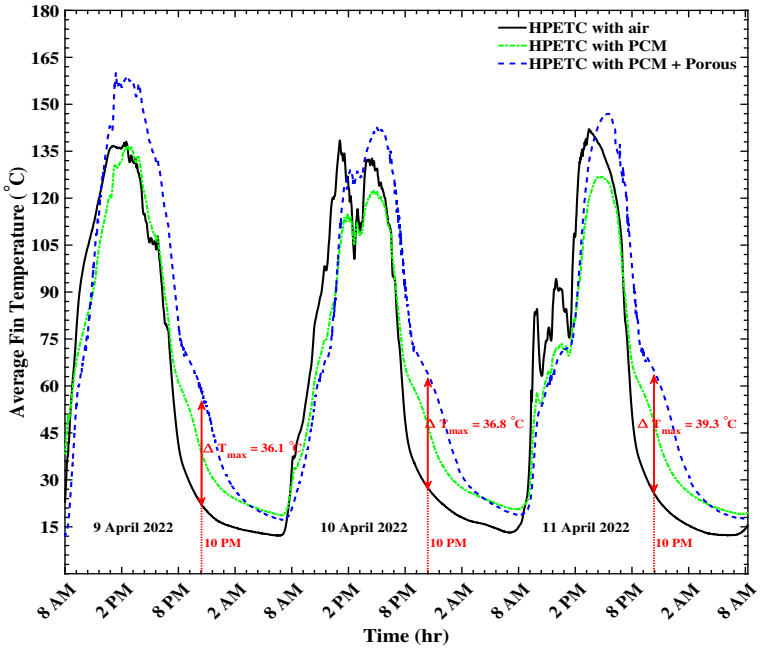

Figure 41: Fin temperature comparison.

Figure 41 depicts fin temperature variation inside the evacuated tubes. During a day, with increase in solar radiation, temperature inside the glass tube also starts rising. On April 9, around 2 PM, when the value of solar radiation is at peak, the evacuated tube filled with PCM + Cu porous metal has reported maximum fin temperature of 158.4° C. On the other hand, conventional evacuated tube and evacuated tube filled with PCM have reported almost same temperature values of 137.6° C and 136.4° C, respectively. Furthermore, conventional evacuated tube reported sudden rise and drop in temperature values inside the glass tube during sunrise and sunset, respectively. The sudden variation inside the evacuated tube temperature reduces the service life of solar water heating system [36, 64, 160]. In contrast, the evacuated tubes filled with PCM and PCM + Cu porous

showed gradual increase and decrease in temperature inside the glass tube. On top of that, around 10 PM, fin temperature difference of 36.1° C is found between the conventional evacuated tube and evacuate tube filled with PCM + Cu porous. Simillarly, the fin temperature difference of 18.2° C is found between the conventional evacuated tube and evacuate tube filled with PCM. During three days of an experiment, the highest difference in fin temperature was recorded on April 11 with value of 39.3° C. After sunset, higher fin temperature inside the evacuated glass tube assists HPETC system to keep in the operation for an extended period of time, where higher outlet water temperature shown in Figure 42 is the clear evident of that.

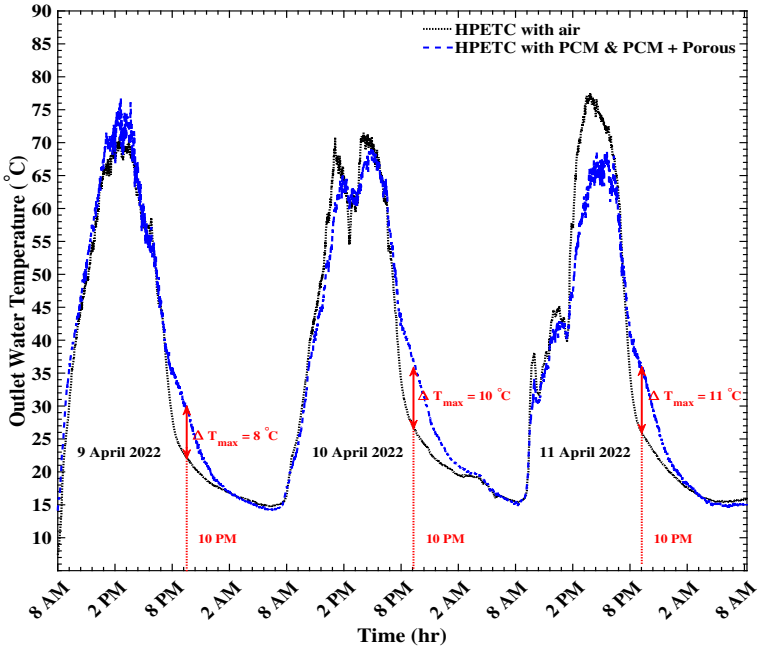

Figure 42: Comparison of water outlet temperature.

Apart from the fin temperature, the performance of conventional HPETC system and HPETC system consist of PCM and PCM + Cu porous metal (combined HPETC system)

is also evaluated by comparing the outlet water temperature. During day time, both the HPETC systems have showed almost same value of water outlet temperature value of 77.5° C and 76.90° C for conventional HPETC and combined HPETC system, respectively. Moreover, during night time at 10 PM (evening peak hours [28]) when the demand of hot water supply is high, the maximum water outlet temperature difference of 8° C is observed on April 9, followed by 10° C and 11° C on April 10 and 11 , respectively.

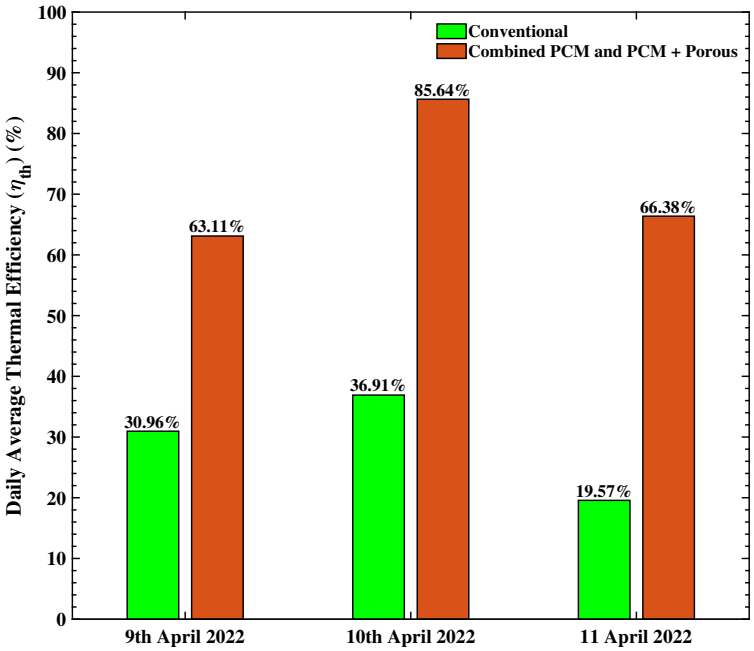

Figure 43: Comparison of daily average thermal efficiency.

The amount of latent heat energy stored (Q_{lhs}) by the combined system (PCM and PCM + Cu porous metal) can be calculated using following equation,

$$Q_{lhs} = (m_{PCM} + m_{PCM+Cuporous})H \tag{4.6}$$

where m_{PCM}+$m_{PCM+Cuporous}$ is the total amount of PCM utillized to fill the evacuated

tubes (0.75 kg in each tube) and H is the latent heat of the Tritriacontane paraffin which is 256 kJ/kg. The total latent heat stored by the combined system is,

$$Q_{lhs} = 1.5(kg)\ H(kJ/kg) \approx 384\ kJ \tag{4.7}$$

Lastly, the performance of HPETC system is evaluated by calculating daily average thermal efficiency. The following equation can be used to calculate the thermal efficiency,

$$\eta_{thermal} = \frac{\dot{m}\ c_p\ (T_{w,out} - T_{w,in})}{A_c G_t} \tag{4.8}$$

where $\dot{m}$ is the mass flow rate of water which was around 0.0126 kg/s (0.2 gpm), c_p is the heat capacity of water (4186 J/kg-k), and $T_{w,out}$ & $T_{w,in}$ are the outlet and inlet temperature of the water. G_t is the total global solar radiation on the collector surface and A_c is the collector gross area which is 0.32 m^2 [14]. Figure 43 show a daily average thermal efficiency of conventional HPETC and combined HPETC system. Based on the comparison, the maximum thermal efficiency of combined HPETC system has increased 48.73% compared with conventional HPETC system. Three days average of thermal efficiency was found around 29.14% and 71.71% for the conventional HPETC system and combined HPETC system.

4.3 Summary of this research work

In this experimental analysis, thermal performance of the HPETC is enhanced by integration of high thermal conductive porous metal with PCM. The experiment is performed on three consecutive days (from April 9-11, 2022). In addition, two large scale HPETC

systems are used to demonstrate the viability of the proposed approach in commercially available HPETC system. Both HPETC systems consist of same number of evacuated tubes to keep the absorber area same (two evacuated tubes on each system). In one HPETC system, two empty evacuated glass tubes are installed without any PCM (conventional system). On the other hand, second HPETC system is also equipped with two evacuated galss tubes, one evacuated tube is filled with Tritriacontane paraffin while the second evacuated tube is filled with Tritriacontane paraffin + Cu porous metal. The same quantity of PCM is used to fill both evacuated tubes (0.75 kg in each tube). The thermal performance of proposed HPETC system is compared with conventional HPETC system. The thermal performance of each system is assessed based on the variation of fin temperature, outlet water temperature and thermal efficiency of HPETC system. Both the collectors are installed at same mounting angle of 45° and with two evacuated glass tubes on each system. In addition, submersible pumps are kept inside the 40 L capacity of the water storage tank for the continues supply of the water. The mass flow rate of water is kept constant at 0.0126 kg/s for both HPETC system.

The evacuated tube filled with PCM + Cu porous metal has reported maximum fin temperature of 158.4° C. On the other hand, conventional evacuated tube and evacuated tube filled with PCM have reported almost same temperature values of 137.6° C and 136.4° C, respectively. On top of that, around 10 PM, fin temperature difference of 36.1° C is found between the conventional evacuated tube and evacuate tube filled with PCM + Cu porous. Simillarly, the fin temperature difference of 18.2° C is found between the conventional evacuated tube and evacuate tube filled with PCM. During three days of an

experiment, the highest difference in fin temperature was recorded on April 11 with the value of 39.3° C. Lastly, the performance of HPETC system is evaluated by calculating daily average thermal efficiency. The maximum thermal efficiency of combined HPETC system has increased 48.73% compared with conventional HPETC system. Three days average of thermal efficiency was found around 29.14% and 71.71% for the conventional HPETC system and combined HPETC system.

CHAPTER 5

PERFORMANCE ANALYSIS OF PHOTOVOLTAIC-THERMAL SYSTEM INTEGRATED WITH PCM/POROUS MEDIUM: CFD MODELING AND EXPERIMENTAL EVALUATION

This research work is under review in *International Journal of Thermal Sciences* (Pending).

"Pawar, V. R., Siddiki, M. K., Sobhansarbandi, S. Performance Analysis of Photovoltaic-Thermal System Integrated with PCM/Porous Medium: CFD Modeling and Experimental Evaluation. *International Journal of Thermal Sciences.*"(Pending).

5.1 Introduction

Among the numerous forms of renewable energy sources, the use of solar energy has shown enormous growth and its proportion to the world's overall energy supply has expanded dramatically [60]. Solar collectors can be used to gather heat energy from the sun, which can then be used to heat water or air [66, 91]. Besides, harvesting solar energy in the form of heat energy, solar cells are capable of directly convert sunlight into electrical energy [174]. Moreover, PV modules produce electricity with no pollution or noise, and it can be placed directly where the power is needed [12]. Despite their many advantages, solar panels have an efficiency of only 15-20 percent, which means that only 15-20 percent of the solar energy absorbed by the solar panel is transformed into electricity, while the remaining 80 -85 percent is dissipated as heat. [1, 5]. Many researchers

have investigated the concept of hybrid photovoltaic/thermal (PVT) systems in order to utilise the waste heat and improve the electrical performance of PVT panels [144]. In hybrid PVT panels, PV cells are placed on top of the absorber plate and connected with copper piping. During an operation, visible light is converted into electricity by solar cells while infrared light is absorbed by a copper absorber plate. Then the generated heat by the absorber is extracted by circulating water through the copper pipes. Al-Shamani et al. [9] conducted experiments to investigate the performance of a PVT system. They have used different types of nano-fluids (SiO_2, TiO_2, and SiC) as heat transfer fluids (HTF). They reported the highest overall efficiency of 81.73% with SiC nanofluid [9]. Salem et al. [126] an experiment to compare the performance of the PV and PVT systems. The results of their study showed an increase in the average electrical efficiency (η_{ele}) of the PVT system from 17.7% to 38.4% in comparison with an uncooled PV system. They concluded that the electrical performance of the PV panel can be improved by extracting excess heat from the PV panel [126]. In addition, some research studies have shown that active heat removal systems can extend lives of PV panels from 30 to 50 years, demonstrating that heat removal enhances not just the PV cells' instantaneous performance but also their lifespan [2, 138].

Numerous experimental and numerical studies have been conducted to further enhance the overall performance of the PVT system. Jia et al. [76] utilised nanofluid as a HTF and numerically studied its effect on the overall performance of a PVT system. The results of the PVT system with Al_2O_3 nanofluid showed better performance compared to the

PVT system with TiO_2 nanofluid. Additionally, they also studied the effects of different mass flow rates of a nano fluid (0.0005 kg/s, 0.001 kg/s, 0.01 kg/s, and 0.03 kg/s). They observed an increase in thermal output by 12.11% for the mass flow rate of 0.03 kg/s in comparison with the mass flow rate of 0.0005 kg/s [76]. Fudholi et al. [58] conducted an experimental analysis to study the effects of different mass flow rates of HTF under various solar radiation conditions ranging from 500 W/m^2 to 800 W/m^2. The results of their study showed maximum overall thermal efficiency of 65% for the mass flow rate of 0.041 kg/s and solar radiation of 800 W/m^2 [58]. Similarly, Khanjari et al. [82] numerically investigated the performance of a PVT system. In their numerical study, they used constant solar radiation of 600 W/m^2 and mass flow rate of 0.06 kg/s. They compared the performance of the PVT system for two different types of HTF: pure water and Al_2O_3-water. They evaluated a PVT system with Al_2O_3-water and found that it increased heat transfer coefficient and electrical efficiency by 24% and 1%, respectively [82]. Hussain et al. [71] proposed a novel design for the PV system attached to honeycomb heat exchanger. In their experimental study, they used different mass flow rates of air, ranging from 0.02 kg/s to 0.13 kg/s and constant solar irradiance of 828 W/m^2. They claimed 87% and 27% thermal efficiency for PV systems with and without heat exchangers, respectively. Additionally, PV system with a heat exchanger showed improvement in electrical efficiency by 0.1% [71]. Mojumder et al. [103] reported improvement in thermal performance by 56.19% after attaching an aluminium fin structure at the back of the PV system. [103]. Hasan et al. [65] extracted heat from the PV system by impinging water on an absorber plate with a mass flow rate of 0.167 kg/s (using a total of 36 nozzles). They reported

electrical, thermal, and overall efficiency of 12.75%, 85%, and 97.75%, respectively [65].

In recent years, integration of phase change materials (PCMs) with the PVT system has attracted many researchers due to its notable latent heat capacity during its phase change process. During the daytime, PCM acts as a thermal capacitance and helps to keep the PV panel temperature lower by absorbing heat. This absorbed heat energy is stored inside the PCM in the form of latent heat. During the night or when the intensity of solar radiation is lower or at zero, it releases its heat energy, which can be utilised to heat water or air for domestic hot water applications. [92, 118, 119, 173]. Browne et al. [22–24] conducted a few experiments to study the effect of PCM on the performance of the PVT system. They observed thermal performance improvements in the range of 20% to 25% [22–24]. Yang et al. [172] claimed that the PVT/PCM system had a 1.8% and a 11.5% increase in electrical and thermal efficiency when compared to the PVT system. [172]. Yuan et al. [173] experimentally compared the performance of the water-based PVT system with that of the PVT/PCM system. The results of their study showed daily electrical efficiencies of 12.1% and 11.9% and thermal efficiencies of 44.5% and 42.3% for the PVT/PCM and PVT systems, respectively. They also claimed that PCM can act as an antifreeze at night and in the winter, preventing the PV system from freezing. [173]. Despite the numerous benefits of integrating a PCM with a PVT system, the lower thermal conductivity of PCMs reduces the overall thermal performance of the PVT system. Khodadadi et al. [84] used nano-enhanced PCM (NEPCM) (0.04%vol Al_2O_3 + RT35-HC PCM) to overcome the poor thermal conductivity issue, while trapezoidal fins were attached to the absorber plate to improve heat transfer inside the PCM. They reported 25.52% increase

in thermal efficiency of the PVT/NEPCM system compared with PVT system. Besides, PVT/NEPCM with fins reported further enhancement in thermal performance by 9.47% compared with the PVT/NEPCM system. Moreover, PVT/NEPCM with fins reduced the PV surface temperature by 1.79°C and increased the liquid fraction of PCM by 16.74% compared with PVT/NEPCM system [84].

In order to enhance the heat transfer inside the PCM, some researchers have suggested impregnation of porous materials into PCM. Kasaeian et al. [121] performed experimental analysis to investigate the effect of aluminum porous on the performance of PVT/PCM system. They developed a low-cost aluminum porous media and integrated with PVT/PCM system. They reported 2.5% increase in electrical efficiency of PVT/PCM/porous compared to only PV system. In addition, the results of their study showed decrease in melting time of the PCM by 25% compared to the PVT/PCM system [121]. Ahmed et al. [8] experimentally investigated influence of the porous media on the performance of the double pass hybrid PVT system. They found thermal efficiency of 80.23% for the PVT/PCM/Porous system while the system without porous medium reported thermal efficiency of 51.25% only [8]. Wang et al. [163] investigated thermal performance of the PVT/PCM/Porous system experimentally. They observed uniform temperature distribution in PVT/PCM/Porous system compared with the only PVT system. They also claimed reduction in temperature of the PV panel by 5 °C for the PVT/PCM/Porous system compared to the PVT/PCM system. In past, some researchers

have made an attempt to investigate the performance of PVT/PCM/Porous system numerically. However, in most of the previous numerical studies, constant solar radiation boundary condition are used, such as Khanjari et al. [82] used constant solar radiation (boundary condition) of 600 W/m^2, Khodadadi et al. [84] and Das et al. [39] used 1000 W/m^2 and many other previous studies used similar constant solar irradiance [69, 80, 105, 125]. To the best of author's knowledge thermal analysis of PV/T integrated with PCM/Porous medium has not been studied under variable heat flux for 24 hours of operation.

In this study, a computational fluid dynamics (CFD) analysis of the performance of PVT system in conjunction with PCM and PCM/porous medium is studied. During the simulation, a real-time transient solar radiation boundary condition is applied to accurately predict the performance parameters such as the surface temperature of the PV cell, the outlet temperature of water, the melting fraction of PCM, and the thermal energy stored by each system. The selected type of porous media is made of Cu and Al metal were used with a porosity of 95% and a pore density of 40 PPI. The reason behind choosing a high porosity value of 95% is to keep the maximum amount of PCM and store the maximum amount of latent heat energy. The PVT system is designed with copper-made riser tubes attached to the back surface of the PV panel, through which water is continuously circulated to remove excess heat from the PV cell.

5.2 Simulation modeling

5.2.1 Model description

A three-dimensional model of the PVT system is constructed using the ANSYS Design modeler, which includes the PVT system integrated with PCM. Figure 44 (a) and (b) show a PVT system integrated with PCM (PVT/ PCM) and a PVT system integrated with PCM and highly conductive porous metal. As shown in the Figure 44, the PVT system is made up of discrete layers. The transparent glass cover allows solar radiation to pass through and provides strength to PV cells from the surroundings. The layer of Ethylene-vinyl acetate (EVA) prevents PV cells from moisture and dust. The PV cell converts solar radiation into electricity. A thin layer of Tedlar Polyvinyl Fluoride (Tedlar) acts as an insulator between the absorber plate and the PV cell. The absorber plate is attached to a copper pipe which continuously extracts heat from the PV cells, and lastly a layer of PCM, which helps to control PV cell temperature and stores access heat energy during the day. In addition, as shown in Figure 44 (b), PCM is embedded in a highly conductive porous metal, which helps to overcome the issue of the lower thermal conductivity of PCM. Cu and Al porous metals with 95% porosity and a pore density of 40 pore per inch (PPI) are used. The reason behind selecting a porosity of 95% is to keep the quantity of PCM higher. Thermophysical properties of each layer of the PVT system integrated with PCM and porous metals are enumerated in Table 11. The actual PVT system, with a dimension of $1.2\times0.508\times0.035$ (l$\times$w$\times\delta$) m^3 has a total of five copper tubes. These tubes are attached to the back side of the panel with copper absorber plates at equal spacing. Also, an arrangement of the top and bottom copper header pipes allows water to flow with

an equal mass flow rate and creates a plane of symmetry at the mid-distance of any two adjacent copper tubes. Therefore, only 1/4 of the geometry is modeled and simulated with symmetry boundary conditions at the side walls [34].

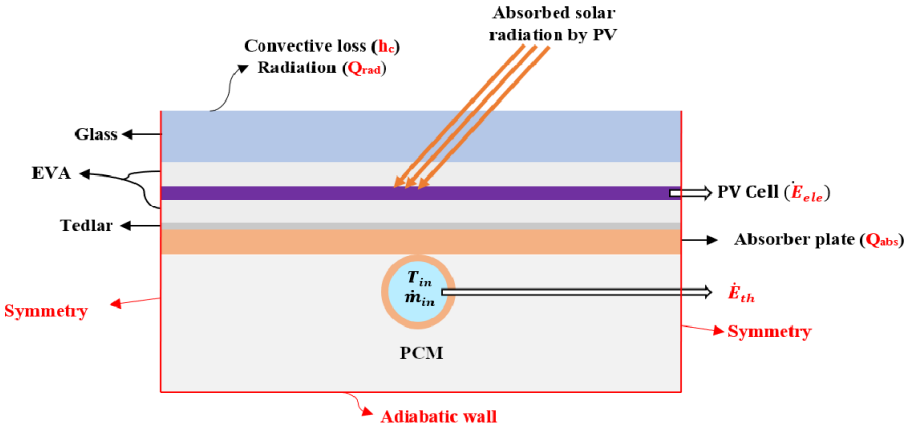

(a) PVT/PCM system

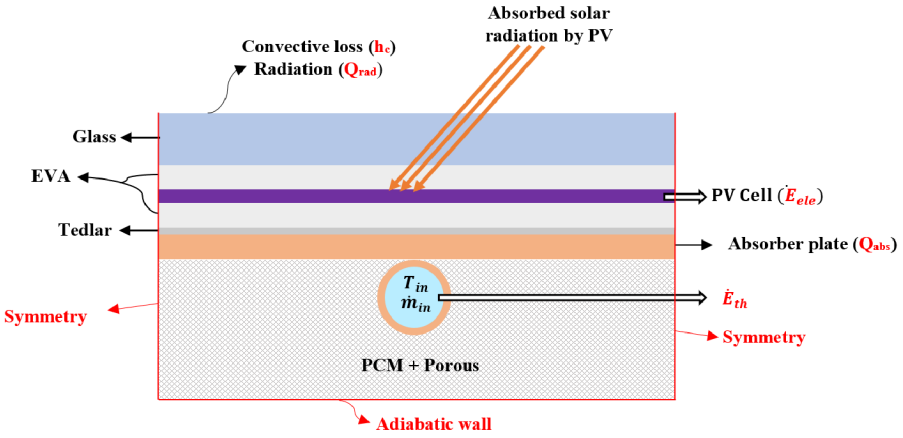

(b) PVT/PCM integrated with highly conductive porous metal

Figure 44: Different configurations of the PVT/PCM systems

Table 11: Thermo-physical properties of the PVT/PCM components [92, 120].

PV cell			Porous material		
	L×W (m)	1.2×0.5	Cu	ρ_{cu} (kg/m^3)	8978
	δ_{PV} (m)	0.0003		$c_{p_{cu}}$(kJ/kgK)	385
	ρ_{PV} (kg/m^3)	2330		k_{cu} (W/mK)	400
	$c_{p_{PV}}$ (kJ/kgK)	700	Al	$\rho_{Al}(kg/m^3)$	2699
	k_{PV} (W/mK)	148		cp_{Al} (kJ/kgK)	900
	η_r (%)	17.39		k_{Al} (W/mK)	210
	α_{PV}	0.85		Porosity	95%
Glass				PPI	40
	δ_g (m)	0.0032		d_{pore}(m)	0.0004
	ρ_g (kg/m^3)	2200		d_f (m)	0.0031
	c_{p_g}(kJ/kgK)	830		K	1.3×10^{-7}
	k_g (W/mK)	0.76		Ci	0.09
	ϵ_g	0.9	PCM		
	α_g	0.1		δ_{PCM}(m)	0.015
EVA				$\rho_{PCM}(kg/m^3)$	800
	δ_{EVA} (m)	0.0005		$c_{p_{PCM}}$(kJ/kgK)	2300
	$\rho_{EVA}(kg/m^3)$	960		k_{PCM}(W/mK)	0.25
	$c_{p_{EVA}}$(kJ/kgK)	2090		h_{sl}(kJ/kg)	170
	k_{EVA} (W/mK)	0.35		T_m(°C)	40
Tedlar			Absorber		
	δ_{Ted}(m)	0.0001		δ_{abs}(m)	0.0005
	$\rho_{Ted}(kg/m^3)$	1200		ρ_{abs} (kg/m^3)	8960
	$c_{p_{Ted}}$ (kJ/kgK)	1250		$c_{p_{abs}}$ (kJ/kgK)	385
	k_{Ted}(W/mK)	0.20		k_{abs}(W/mK)	401
Tube					
	d (m)	0.010			
	δ_{tube}(m)	0.001			

5.2.2 Boundary conditions and governing equations

In order to simulate different configurations of PVT/PCM systems, three-dimensional transient simulations are carried out with several assumptions,

- The contact resistances in each layer of the PVT/PCM/Porous metal system are neglected [83];
- The HTF flowing through a copper pipe and the natural convective flow of molten PCM are considered laminar and incompressible;
- The structure of porous metal is considered homogeneous;
- The natural convective flow of molten PCM is derived using Boussinesq approximation;
- Incident solar radiation is uniformly distributed over the PV cell.

Considering the above mentioned assumptions, suitable boundary conditions are applied to each component of the PVT/PCM/Porous metal system and the following governing equations are solved.

5.2.2.1 PVT module

The top glass layer of the PVT system is defined as a semi-transparent glass with a transitivity of 0.9, and convective heat transfer loss through the glass layer is calculated by [128]:

$$\dot{q}_{loss} = h_w^*(T_{amb} - T_g) + \sigma\epsilon((0.0522 \times {T_{amb}}^{1.5})^4 - {T_g}^4) \tag{5.1}$$

where σ is Stefan-Boltzman constant and ϵ is emissivity of the glass. The value of a T_{amb} used in Eq 5.1 is shown in Figure 45 while (h_w^*) is calculated by,

where V_w is the velocity of wind considered to be constant at 0.5 m/s [6]. Similarly, the transitivity of both EVA and Tedlar is defined as 1. While the solar cell is defined as an opaque surface with an absorptivity of 0.85. In order to implement a real-time solar radiation boundary condition, experimentally recorded solar radiation and ambient temperature data recorded by Browne et al. [23] shown in the Figure 45 are used as a boundary condition using a user-defined function (UDF). In UDF, transient solar radiation data and ambient temperature data are defined using a polynomial function. The equation (5.2) is used to calculate the useful heat gain by the PV cell.

$$\dot{Q}_{useful} = \dot{Q}_{available}\tau_{(g)}\tau_{(EVA)}\alpha_{cell} \tag{5.2}$$

The layer of the PV cell absorbs this useful heat energy ($\dot{Q}_{useful}$) and generates electricity and heat. Heat generated in PV cell layer is conducted in different layers of PVT system via conduction, which is calculated by,

$$\rho_s C_{p,s} \frac{\partial T_s}{\partial t} = \nabla.(k_s \nabla T_s) \tag{5.3}$$

where ρ_s, $c_{p,s}$ and k_s are the thermal properties of solid layers defined in Table 11, t is the time in seconds and subscript "s" indicates the solid layers of the PV modules.

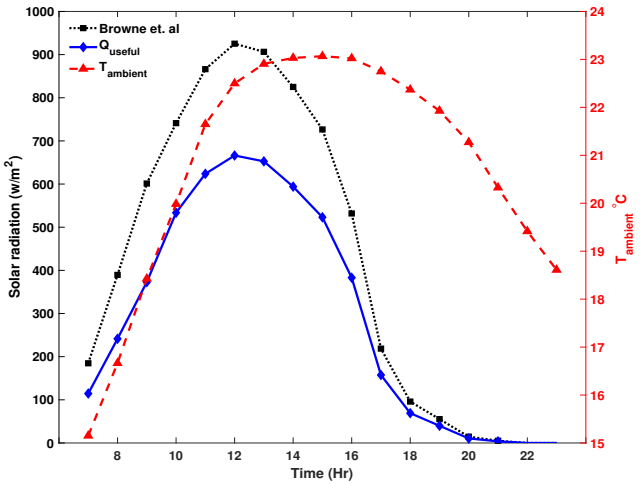

Figure 45: Solar radiation [23].

5.2.2.2 Heat transfer fluid

In order to lower the PV cell temperature, water is continuously circulated through the copper pipe at a constant mass flow rate of 0.03 kg/s. No slip boundary condition is applied at the inner wall of the pipe. On the outlet of the copper pipe, a pressure outlet boundary condition is applied. The following transient form of the governing equations are used to simulate the heat transfer fluid (HTF).

$$\frac{\partial \rho_f}{\partial t} + \nabla(\rho_f \vec{V_f}) = 0 \tag{5.4}$$

$$\frac{\partial}{\partial t}(\rho_f \vec{V_f}) + \nabla(\rho_f \vec{V_f} \vec{V_f}) = -\nabla p + \nabla \cdot (\mu_f \nabla \vec{V_f}) \tag{5.5}$$

$$\frac{\partial}{\partial t}(\rho_f H) + \rho c_{p,f} \vec{V_f} = \nabla(k_f \nabla T_f) \tag{5.6}$$

where ρ_f, $\vec{V}_f$ and μ_f are the density, velocity and viscosity of water, respectively.

5.2.2.3 Porous medium with PCM

The solidification and melting process of the PCM is simulated using an enthalpy-porosity model. The detailed mathematical modeling for the phase change process of PCM is discussed in previous work by the authors [97, 118]. Apart from that, to simulate the phase change process of the PCM embedded with porous metal, the following transient form of the governing equations are used:

Continuity:

$$\frac{\partial \rho_{pcm}}{\partial t} + \nabla(\rho_{pcm}\vec{V}_{pcm}) = 0 \tag{5.7}$$

Momentum equation:

$$\rho_{pcm}\frac{\partial}{\partial t}(\vec{V}_{pcm}) + \frac{\rho_{pcm}}{\epsilon}((\vec{V}_{pcm}\cdot\nabla)\vec{V}_{pcm}) = -\nabla p + \frac{\mu_{pcm}}{\epsilon}\nabla^2(\vec{V}_{pcm}) + S_g \tag{5.8}$$

where momentum sink term S_g includes enthalpy-porosity model, Darcy model, and buoyancy force (from left to right).

$$S_g = A_{mushy}\frac{(1-\beta)^2}{\beta^3+\delta}\vec{V}_{pcm} - \frac{\mu}{K}\vec{V}_{pcm} - \frac{\rho C_i}{\sqrt{K}}\left|\vec{V}_{pcm}\right|\vec{V}_{pcm} + \rho_{pcm,ref}g\beta\epsilon(T_{pcm}-T_{ref}) \tag{5.9}$$

where, C_i, K and ϵ are the properties of the porous metal and it can be found in Table 11. In current CFD study, local thermal equilibrium (LTE) model is used to simulate the

heat transfer between PCM and porous metal. LTE model considers the same value of temperature for the PCM and porous metal.

Energy equation:

where total enthalpy H is calculated using equation:

$$H = h_{ref} + \int_{T_{ref}}^{T} c_{p_{eff}}\, dT + f_l h_{sl} \tag{5.10}$$

where h is sensible enthalpy (at T_{ref}), liquid fraction of the PCM f_l and the value of effective specific heat can be written as:

$$\rho_{eff} c_{p,eff} = \epsilon \rho_{pcm} c_{p,pcm} + (1-\epsilon)\rho_{por} c_{p,por} \tag{5.11}$$

ρ_{eff} term in Eq. (5.11) is calculated using Eq. (5.12).

$$\rho_{eff} = \epsilon \rho_{pcm} + (1-\epsilon)\rho_{por} \tag{5.12}$$

The effective thermal conductivity k_{eff} of PCM/porous metal composite is calculate using Eq. (5.12),

$$\lambda_{eff} = \frac{\sqrt{3}}{2}[R_a + R_b + R_c]^{-1} \tag{5.13}$$

$$R_a = \frac{0.09\psi}{\lambda_{PCM} + \frac{1}{3}(1+\psi)(\lambda_{por} - \lambda_{PCM})} \tag{5.14}$$

$$R_b = \frac{0.91\psi}{\lambda_{PCM} + \frac{2}{3}\psi(\lambda_{por} - \lambda_{PCM})} \tag{5.15}$$

$$R_c = \frac{\frac{\sqrt{3}}{2} - \psi}{\lambda_{PCM} + \frac{0.12}{\sqrt{3}}\psi(\lambda_{por} - \lambda_{PCM})} \tag{5.16}$$

$$\psi = \frac{-0.09 + \sqrt{0.0081 + \frac{2\sqrt{3}}{3}(1-\epsilon)[2 - 0.09(1 + \frac{4}{\sqrt{3}})]}}{\frac{2}{3}(1.91 - \frac{0.36}{\sqrt{3}})} \tag{5.17}$$

5.2.2.4 Performance of PVT system

Lastly, electrical and thermal efficiency of the of different configurations of PVT/PCM systems are calculated using Eq. 5.18 and 5.19, respectively:

$$\eta_{ele} = \eta_{ref} * [1 - 0.0045(T_{cell} - 298.15)] \tag{5.18}$$

where, T_{cell} is the PV cell temperature and η_{ref} depicts the electrical performance of the PV cell at standard condition.

$$\dot{Q}_t = \dot{m}_f \, C_{(p,f)} \, (T_{(f,out)} - T_{(f,in)}) + E_{PCM} \tag{5.19}$$

where, $\dot{m}_f$ and $C_{p,f}$ are mass flow rate and specific heat capacity of HTF. $T_{(f,out)}$ $T_{(f,in)}$ are outlet temperature and inlet temperature of HTF, respectively. While, E_{PCM}, the amount of thermal energy stored inside the PCM in the form of latent heat energy can be calculated as follows,

where, m_{PCM} and $C_{(p,PCM)}$ are the mass and heat capacity of PCM at time 't', respectively. In addition, t_i is initial time, $t_{(fl,0)}$ is time when melting process begins, and $t_{(fl,1)}$ is the time when PCM is completely in liquid phase.

Lastly, overall thermal efficiency of PV-T/PCM systems can be calculated by,

$$\eta_{overall} = \eta_{th} + \eta_{ele} \tag{5.20}$$

5.2.3 Mesh

The Figure 46 illustrates a cross-section view of the PVT/PCM system, which is discretized using hexahedral mesh. A patch-confirming method is used in order to ensure the connectivity between each layer of the PVT/PCM system. In addition, the mesh is refined near the inner wall of the pipe to accurately capture the temperature gradient, which adds more accuracy and also helps to achieve faster convergence.

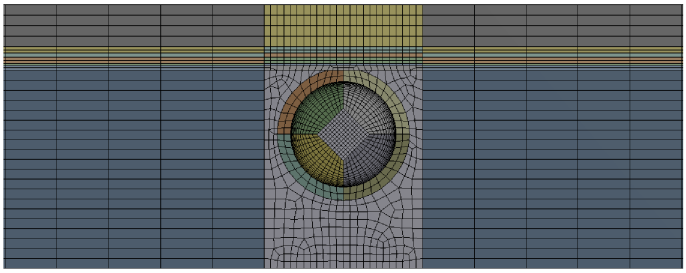

Figure 46: PVT/PCM mesh

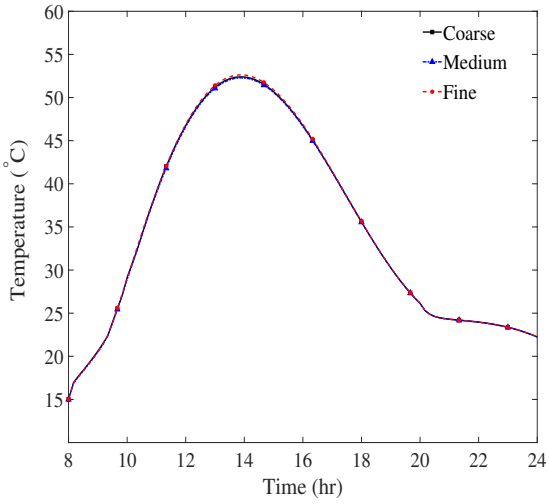

Figure 47: PVT/PCM system back surface temperature

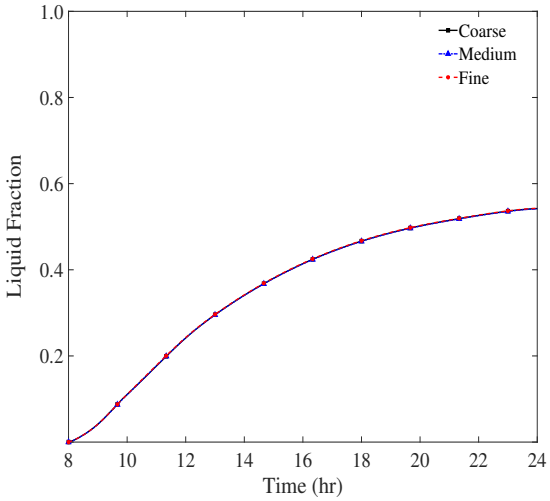

Figure 48: PVT/PCM system liquid fraction

Furthermore, simulation results are tested for different mesh sizes and values of PV cell temperature, liquid fraction of PCM, and outlet temperature of water are compared to ensure results are mesh independent. In addition, simulations are carried out using a time-adaptive scheme with a minimum and maximum time-step size of 0.001 and 0.1 second (Courant no. ≤ 0.25). Table 12 show value of PV cell temperature, liquid fraction of PCM, and outlet temperature of water for different grids. The difference in PV cell temperature (T_{cell}), liquid fraction (f_l), and outlet temperature of HTF ($T_{(f,o)}$) between medium and fine mesh is found to be 0.04%, 0.07%, and 0.04%, respectively. Because of the lower variation ($< 0.1\%$) in the output data, a medium mesh size (with 895,834 nodes) was chosen for further analysis in the final analysis.

Table 12: Mesh independence test

	Mesh type	**No. of nodes**	T_{cell} **(K)**	f_l	$T_{(f,o)}$ **(K)**
1	Coarse	409,705	325.3995	0.5421	298.1136
2	Medium	895,834	325.4825	0.5424	298.1182
3	Fine	1,932,858	325.6325	0.5428	298.1210

5.2.4 Numerical method and model validation

In order to solve the governing equations for each element of the discretized model of the PVT system, the commercially available CFD package Ansys-Fluent 2020 R2 is used. During the simulation, velocity and pressure equations are coupled using a SIMPLE (Semi-Implicit Method for Pressure-Linked Equations) algorithm, while the pressure values at the cell faces are interpolated using a PRESTO (PREssure STaggering Option) scheme. In order to achieve the better accuracy in numerical results, convergence criteria of 10^{-6} for the mass and momentum and 10^{-9} for the energy equation are set. During a simulation, area weighted average value PV cell surface and outlet temperature of HTF are tracked throughout the simulation. Also, to calculate the amount of stored heat energy inside the PCM, the melting rate of the PCM is tracked with volume average method. In order to ensure the reliability of CFD model, validation process is classified into two parts. In the first part (part-I), CFD results of the PVT/PCM system is validated with an experimental study carried out by Browne et al. [23]. In second part (part-II), melting process of PCM embedded with porous metal is validated with an experimental study conducted by Tian et al. [155]. In addition, result of the CFD study is also compared with other numerical study as well for both parts to ensure the accuracy and reliability of

current CFD model.

5.2.4.1 Part-I: Validation of PVT/PCM system

In order to validate the CFD model of PVT/PCM system, PV cell temperature is tracked throughout the simulation and compared with experimental values reported by Browne et al. [23]. Figure 49 shows the comparison of PV cell temperature data recorded during an experiment and value calculated by CFD study. It can be noticed that both experimental and simulation results follow the same trend, the value of PV cell temperature starts increasing during a day from 8 to 14 hr and after 14 hr, It starts decreasing. The simulated results showed a maximum and minimum deviation of 2.35% and 0.01%, while a mean deviation of 0.82% is found from 8 to 11 hr. The main reason behind this deviation is melting point of the PCM which is kept constant during the simulation, while during an experiment author mentioned the melting temperature range of 17.7 to 22.8 °C.

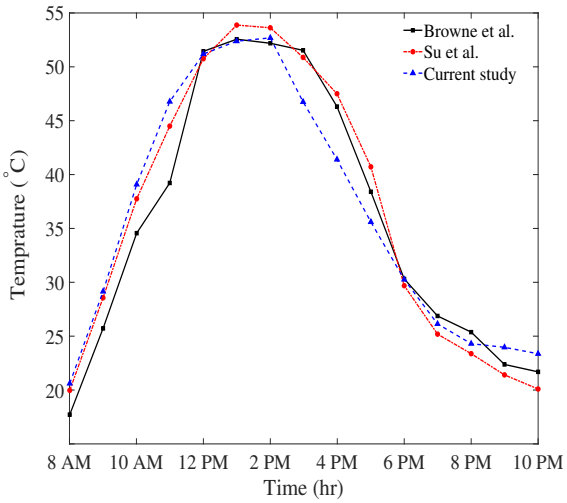

Figure 49: PVT system model Validation using experimental data by Browne et al. [23]

5.2.4.2 Part-II: Validation of phase change process of PCM embedded with porous metal

The numerical model used to simulate the phase change process is validated with both an experiment and numerical data published by Tian et al. [155]. Figure 50 depicts the temperature profile tracked at the distance of 8mm away from the heating plate. Temperature value obtained using current numerical model is compared with an experimental work performed by Tian et al. [155] and numerical study performed by Liu et al. [96]. The result of the current study show a good agreement with and experimental data and the current numerical model is found more accurate compared with the numerical model proposed by Liu et al. [96].

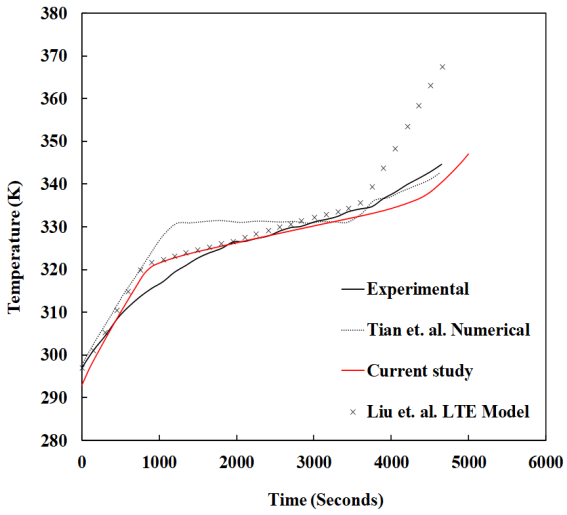

Figure 50: Porous medium model validation using the data by Tian et al. [96, 155]

5.3 Results and discussion

After validating the numerical models, further analysis has been done on two different configurations of PVT/PCM/Cu and PVT/PCM/Al systems. During the simulation, important parameters such as surface temperature of the PV cell, amount of thermal energy stored, value of melting fraction, and outlet temperature of water are tracked to calculate the electrical and thermal performance of the PVT/PCM embedded with porous metals.

5.3.1 Effect of porous metal on the PV cell temperature

The effect of porous materials on the surface temperature of the PV cell is illustrated in Figure 51 which depicts variation in the surface temperature of the PV cell throughout a day. Initially, the surface temperature of PV cell is found to be higher for the PVT/PCM based system due to the higher thermal resistance between the copper (absorber) plate and the PCM. On the other hand, the system with porous metal showed a low surface temperature. The reason behind the low surface temperature is the integration of PCM with porous metal, which improves the overall heat transfer between the absorber plate and PCM. Uniform heat distribution is achieved inside the PCM due to the high thermal conductivity of the Cu and Al porous metals. A gradual increase in PV cell surface temperature is evident in Figure 51.

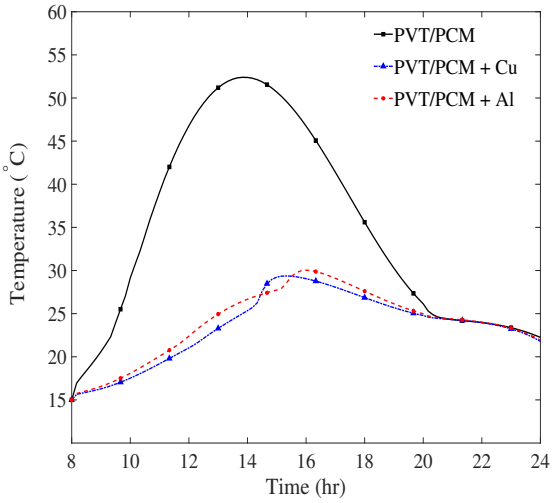

Figure 51: Effect of porous metal on temperature of the PV cell

As can be seen in Figure 51, compared with the PVT/PCM system, PV cell temperature decreased by 7.04% and 6.84% when PCM is embedded with Cu and Al metal foam, respectively. It can also be noticed from Figure 51, that the PVT/PCM/Al system has shown a slightly higher temperature due to the fact that Al has a lower thermal conductivity than copper. The performance of the PV cell is very sensitive to the operating temperature. Even an increase of 1K temperature decreases the performance of the PV cell by 0.65% [122].

5.3.2 Effect of porous metal on PCM melting

The main purpose of adding porous metal to PCM is to overcome the lower thermal conductivity issue and enhance the overall heat transfer inside the PCM. Figure 52 depicts the melting fraction of the PCM for the PVT/PCM, PVT/PCM/Cu and PVT/PCM/Al. It

can be seen in Figure 52 that only 50% melting of the PCM is achieved by PVT/PCM system. On the other hand, 100% melting is achieved by integrating PCM with porous metal, which clearly indicates the improved heat transfer inside the PCM. Moreover, due to the high thermal conductivity of copper, melting process is completed around 1 PM in PVT/PCM/Cu system. While the melting process of PCM is delayed by an hour for the PVT/PCM/Al system.

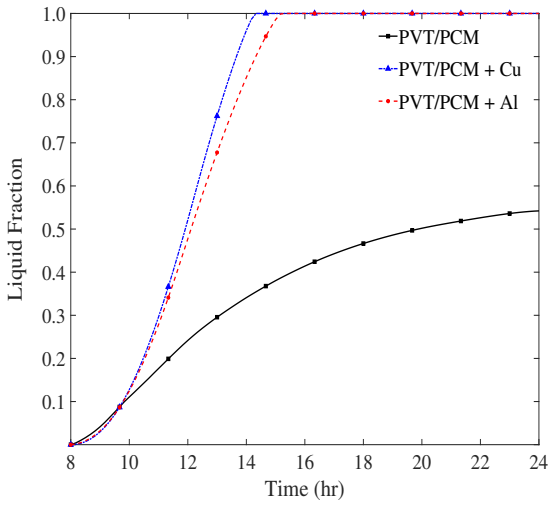

Figure 52: Effect of porous metal on PCM melting

In order to study the melting behaviour of the PCM, melting fraction contours of the PVT/PCM, PVT/PCM/Cu and PVT/PCM/Al has shown in Figure 53, 54, and 55, respectively.

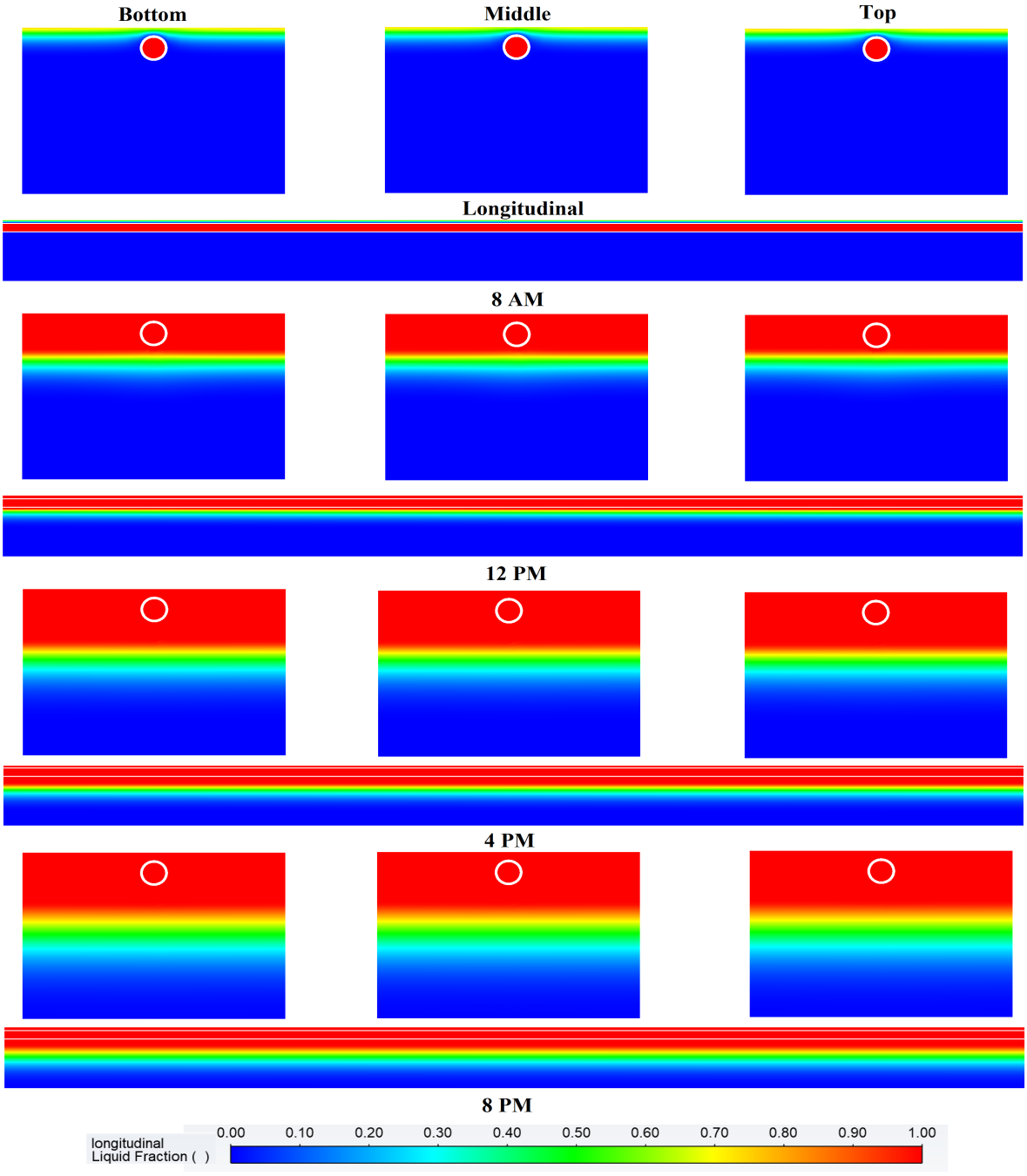

Figure 53: PVT Liquid fraction contour

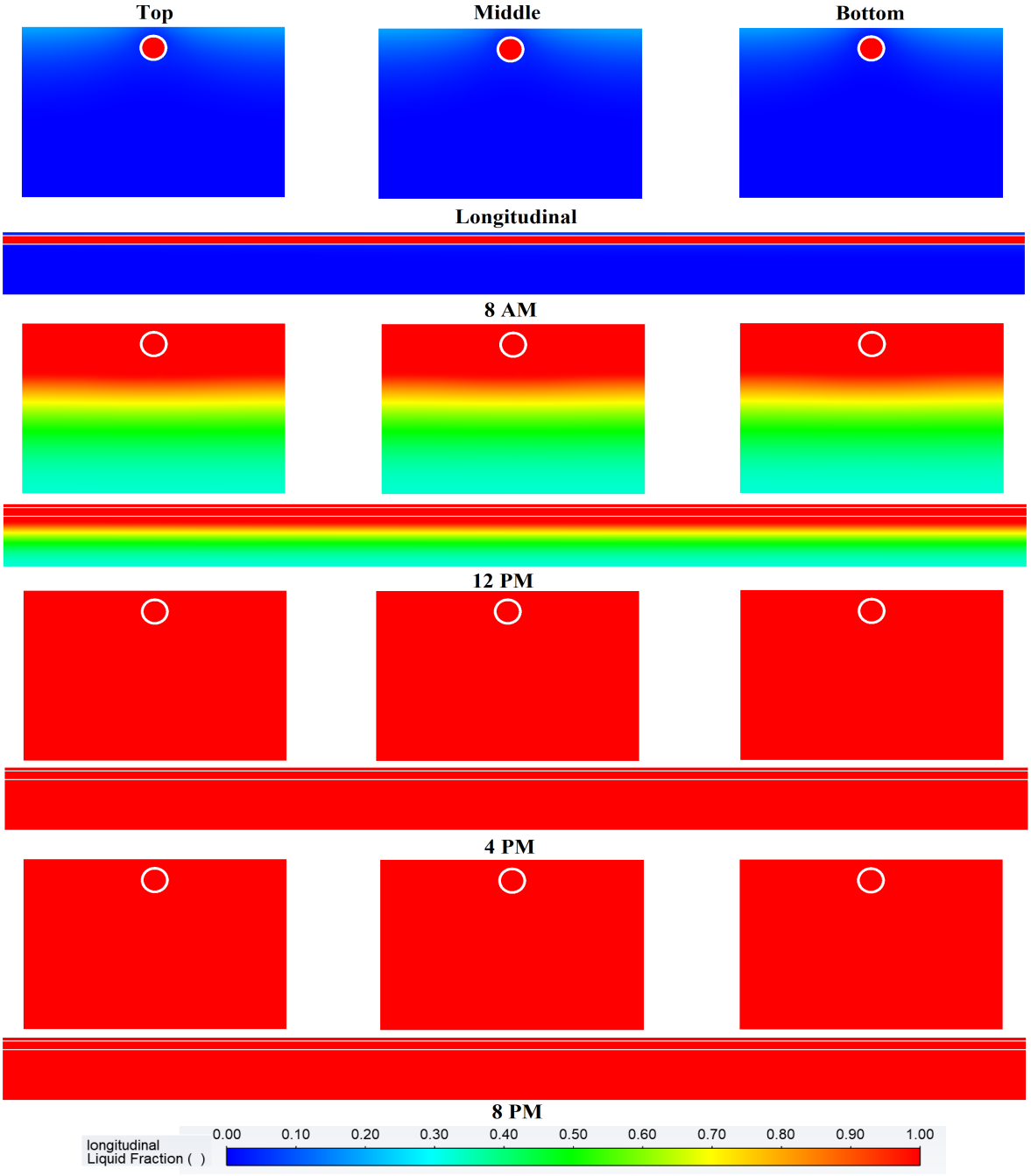

Figure 54: PVT/PCM/Al Liquid fraction contour

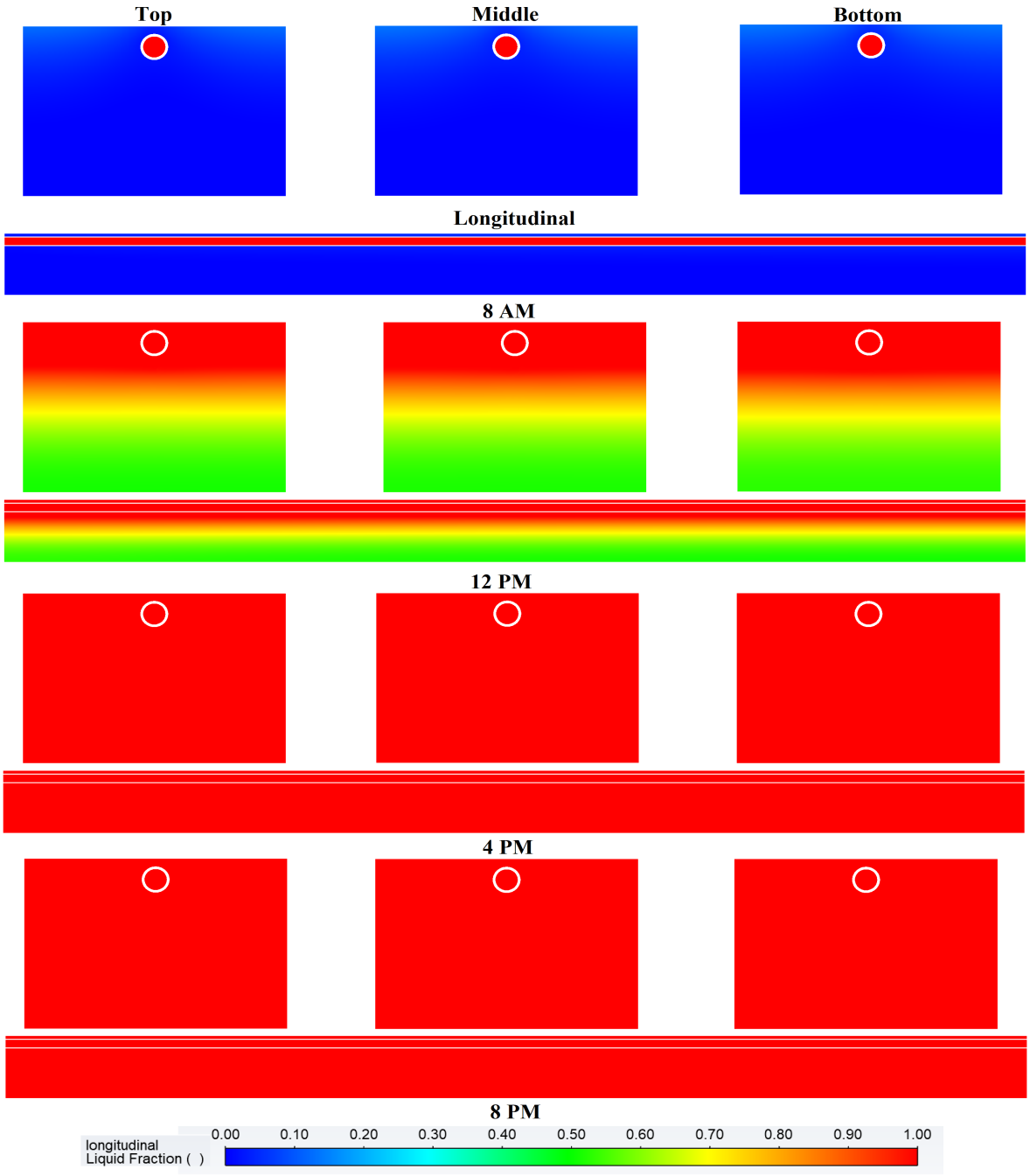

Figure 55: PVT/PCM/Cu Liquid fraction contour

Figure 53 illustrates the liquid fraction of PCM for PVT/PCM system. Around 8 AM,

near the back surface of the PV panel very thin layer of the PCM is found in mushy-zone. Due to having a zero inclination angle, PCM has shown same melting behaviour at top, middle and bottom sections. At noon, PCM is found completely in liquid phase near the absorber plate. Besides, the bottom part of the container is found in solid phase due to the poor heat transfer inside the PCM. Likewise, at around 4 PM and 8 PM, melting behaviour of the PCM is found to be similar. On the other hand, as shown in Figure 54 and Figure 55, embedding PCM with porous metal has shown an improved melting fraction. Melting fraction contours at 4 PM and 8 PM in Figure 54 and Figure 55 are evidence of the improved melting fraction. In addition, it clearly indicates that embedding PCM with highly conductive porous metal accelerates heat transfer into the depth of the PCM.

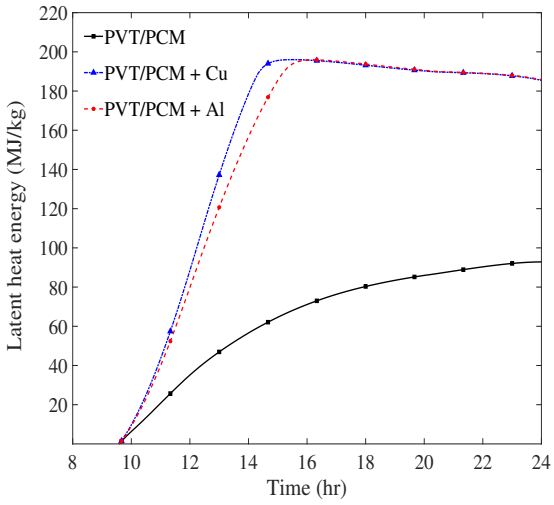

Figure 56: Effect of porous metal on Latent heat energy

Figure 56 represents the amount of thermal energy stored by PCM in the form of latent heat with respect to time. The PVT/PCM system reported a maximum latent heat storage

of 92.84 kJ/kg. On the other hand, PVT/PCM/Cu and PVT/PCM/Al systems reported maximum latent heat storage of 196.03 kJ/kg and 195.91 kJ/kg, respectively (which is almost 2.11 times higher compared with the PVT/PCM system). It is concluded that embedding PCM with porous metal increases the heat storage capacity to a great extent.

5.3.3 Electrical efficiency and thermal energy output

Figure 57 shows an electrical performance of the PVT/PCM, PVT/PCM/ Cu, and PVT/PCM/Al systems with respect to time. In order to calculate electrical performance, Eq 5.18 is used [148]. At around 2 PM, PVT/PCM system reported the lowest electrical efficiency of 10.25%. On the other hand, PVT/PCM/Cu and PVT/PCM/Al systems exhibited electrical efficiency of 11.49% and 11.41% which is 12.09% and 11.31% higher compared with PVT/PCM system, respectively.

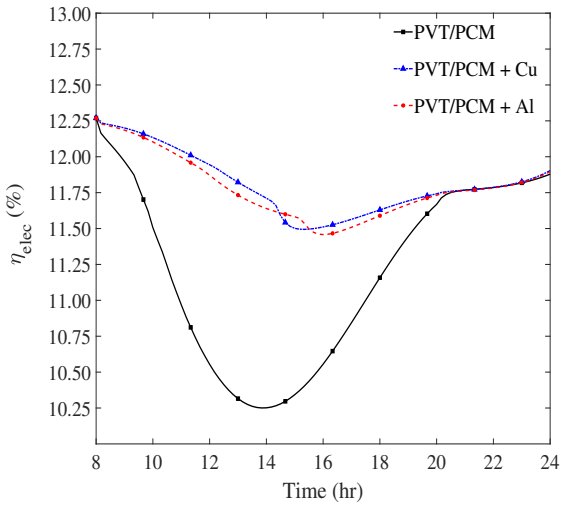

Figure 57: Effect of porous metal on electrical performance of the PV system

Figure 58 depicts thermal output of the PVT/PCM, PVT/PCM/Cu, and PVT/PCM/Al

systems calculated using Eq 5.19. As shown in Figure 58, thermal output of PVT/PCM started increasing very slowly due to poor heat transfer inside the PCM. On the other hand, the PVT/PCM/Cu and PVT/PCM/Al systems showed a sharp increase in thermal energy output. The reasons are the faster melting rate and improved heat transfer into the depth of the PCM. The PVT/PCM system reported thermal output of only 442.87 kJ, while the PVT/PCM/Cu and PVT/PCM/Al systems reported almost the same thermal output of 935.26 kJ, which is almost double the amount compared with PVT/PCM system.

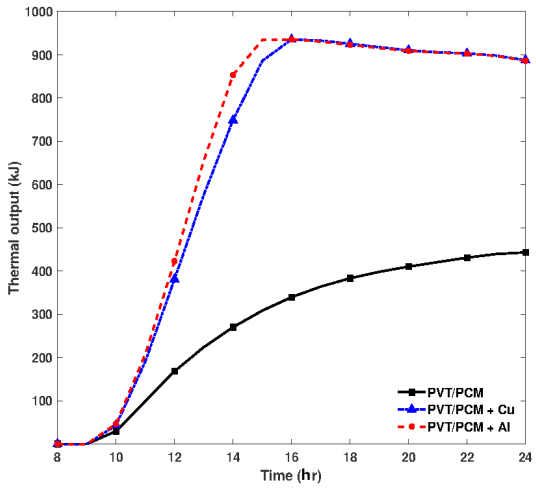

Figure 58: Effect of porous metal on thermal performance of the PV system

5.4 Summary of this research work

The performance of the PVT system is studied numerically to investigate the effect of PCM embedded in highly conductive porous metal. The Cu and Al metal foam with a porosity of 95% and a pore density of 40 PPI is used to enhance the overall thermal conductivity of the PCM. In addition, Cu and Al metal foams helps to reduce the PV cell

temperature by reducing thermal resistance between absorber plate and PCM. In the current CFD study, 3D models of PVT systems with three different configurations of PVT systems (PVT/PCM, PVT/PCM/Cu and PVT/PCM/Al system) are studied. In addition, during the simulation, a real-time transient solar radiation boundary condition is applied to accurately predict the performance parameters such as the surface temperature of the PV cell, melting fraction of PCM, and the thermal energy stored by each system. The PVT/PCM/Cu and PVT/PCM/Al systems showed a faster melting process compared with PVT/PCM system. Both PVT/PCM/Cu and PVT/PCM/Al systems reported 100% melting of the PCM, while PVT/PCM system showed only 50% melting of the PCM. By embedding PCM with porous metal, the melting process was expedited, which resulted in the complete melting of the PCM at 14 hrs. In addition, in compared with the PVT/PCM system, PV cell temperature decreased by 7.04% and 6.84% when PCM is embedded with Cu and Al metal foam, respectively. The PVT/PCM/Cu and PVT/PCM/Al systems exhibited electrical efficiency of 11.49% and 11.41% which is 12.09% and 11.31% higher compared with PVT/PCM system, respectively. The PVT/PCM system reported thermal output of only 442.87 kJ, while the PVT/PCM/Cu and PVT/PCM/Al systems reported almost the same thermal output of 935.26 kJ, which is almost double the amount compared with PVT/PCM system.

CHAPTER 6

CONCLUSION

The common sources of energy such as electricity, gas, and oil can be inefficient and produce carbon emissions, all of which contribute to global climate change. In the united states, water heating accounts for the second-largest heating demand approximately 20% of all household energy use. Solar water heating (SWH) systems are capable to reduce household energy usage and carbon dioxide emissions by preheating the air or water before it enters a conventional heater. Among various types of solar collectors, evacuated tube solar collector (ETC) has attracted many attentions especially for the application in SWHs. However, due to the intermittency in solar intensity, the ETCs may not work at their maximum functionality. In this study, the computational fluid dynamics (CFD) modeling of a heat pipe ETC (HPETC) with and without the integration of phase change materials (PCMs) is performed. In order to cross-validate the obtained results from CFD and recent experimental analysis, the boundary conditions are set as the field-testing data. In phase-I, the 3D model of commercially available HPETC is simulated, while in phase-II, the HPETC integrated with the PCM is developed. The selected type of PCM is Tri-triacontane paraffin ($C_{33}H_{68}$) with melting point of 72 °C. The simulation results show an acceptable agreement with the experimental data with an average deviation of 4.8% and 2.04% for phase-I and phase-II, respectively. In order to further increase accuracy of a numerical model, volume of fluid (VOF) approach is adopted to simulate two-phase

(evaporation-condensation process) phenomena inside a heat pipe. The result showed 0.78% increase in numerical model accuracy when heat pipe is simulated as a two-phase device in comparison with the numerical model in which HP is considered as a high thermal conductive device (simplified approach). However, CPU time is also increased extensively from 30 minutes to two weeks (20160 minutes) when heat pipe is simulated as a two-phase device compared with simplified approach. Due to large computational time, simplified numerical approach is adopted to optimize thermal performace of a HPETC system.

The performance of an HPETC is optimized in two phases, where phase-I is focused on the effect of HP position in stagnation (on-demand) operation, and in phase-II, the effects of various energy storage materials in both normal and on-demand operation are investigated. In phase-I, under stagnation mode, results show that the solid-to-liquid phase change process was expedited by 48 minutes when the HP shifted from the top to the center of the glass tube. On the other hand, during normal operation, the maximum liquid fraction of PCM was reached up to 98% in an optimized system where the conventional system reached up to only 74%. The results of the stagnation and normal operation exhibit the significance of HP position on melting process of PCM and its effect on latent heat thermal energy storage system. In phase-II, the optimized configuration of the HP is selected for further investigation of various types of PCMs with different melting points and latent heat capacities. In normal mode, the HPETC system integrated with tritriacontane paraffin exhibited total energy storage of 295 kJ/kg per tube at a water mass flow rate of 45 LPH, however, the fin temperature of the tube integrated with xylitol at each time

step was around 10°C higher compared with the other tubes during the daytime due to its high specific heat capacity. In the stagnation mode, erythritol shows maximum thermal energy storage of 413.15 kJ/kg per tube, however, the tube integrated with xylitol shows higher fin temperature at each time step. Consequently, the utilization of tritriacontane paraffin/xylitol in normal operation and erythritol/xylitol in on-demand operation is recommended to enhance the system's thermal performance.

During normal operation, no PCM has showed 100% melting fraction due to its poor thermal conductivity. In order to increase effective thermal conductivity of the PCM, high thermal conductive Cu porous metal is integrated with PCM. Experimental analysis is carried out to demonstrate the viability of proposed approach in commercially available HPETC system. In this experiment, two large scale HPETC systems are used. In one HPETC system, two empty evacuated glass tubes are installed without any PCM (conventional system). On the other hand, second HPETC system is also equipped with two evacuated galss tubes, one evacuated tube is filled with Tritriacontane paraffin while the second evacuated tube is filled with Tritriacontane paraffin + Cu porous metal. The same quantity of PCM is used to fill both evacuated tubes (0.75 kg in each tube). The thermal performance of proposed HPETC system is compared with conventional HPETC system. The thermal performance of each system is assessed based on the variation of fin temperature, outlet water temperature and thermal efficiency of HPETC system. During the experiment, proposed system has reported maximum thermal efficiency of 71.71% while conventional system showed maximum thermal efficiency of only 29.14%. Impregnation of porous metal to PCM showed promising result in HPETC system. The same approch

is used to improve electrical and thermal performance of a photovoltaic-thermal (PVT) system. CFD analysis is carried out to to assess the effect of integrating PCM + Porous metal with PVT system. 3D models of PVT systems with three different configurations of PVT systems (PVT/PCM, PVT/PCM/Cu and PVT/PCM/Al system) are studied. In addition, during the simulation, a real-time transient solar radiation boundary condition is applied to accurately predict the performance parameters such as the surface temperature of the PV cell, melting fraction of PCM, and the thermal energy stored by each system. The PVT/PCM/Cu and PVT/PCM/Al systems exhibited electrical efficiency of 11.49% and 11.41% which is 12.09% and 11.31% higher compared with PVT/PCM system, respectively. The PVT/PCM system reported thermal output of only 442.87 kJ, while the PVT/PCM/Cu and PVT/PCM/Al systems reported almost the same thermal output of 935.26 kJ, which is almost double the amount compared with PVT/PCM system. The outcome of this study can be a benchmark for further optimization of thermal energy storage based solar collectors.

CHAPTER 7

FUTURE WORK

In current study, the amount of PCM used to fill an evacuated glass tube is limited due to the aluminum bags which creates void space and resulted into low volume of the PCM. This issue can be addressed by developing a rigid aluminum or copper container which can be easily inserted to the glass tube. Aluminum container can store higher amount of the PCM compared with the aluminum bags which helps to store higher amount of latent heat energy during a day-time operation. In addition, PCM with different melting temperature and latent heat capacity can be utilized with porous metal to further increase the thermal performance of the heat pipe evacuated tube solar collector.

CHAPTER 8

PUBLICATIONS

8.1 PEER-REVIEWED JOURNALS

- **Pawar, V. R.**, Siddiki, M. K., Sobhansarbandi, S. Performance Analysis of Photovoltaic-Thermal System Integrated with PCM/Porous Medium: CFD Modeling and Experimental Evaluation. International Journal of Thermal Sciences (Pending).

- **Pawar, V. R.**, & Sobhansarbandi, S. (2021). Design optimization and heat transfer enhancement of energy storage based solar thermal collector. Sustainable Energy Technologies and Assessments, 46, 101260.
  DOI: https://doi.org/10.1016/j.seta.2021.101260

- **Pawar, V. R.**, & Sobhansarbandi, S. (2020). CFD modeling of a thermal energy storage based heat pipe evacuated tube solar collector. Journal of Energy Storage, 30, 101528.
  DOI: https://doi.org/10.1016/j.est.2020.101528

- Mahdavi, M., Tiari, S., & **Pawar, V.** (2020). A numerical study on the combined effect of dispersed nanoparticles and embedded heat pipes on melting and solidification of a shell and tube latent heat thermal energy storage system. Journal of Energy Storage, 27, 101086.
  DOI: https://doi.org/10.1016/j.est.2019.101086

8.2 CONFERENCE PROCEEDINGS (REFEREED)

- **Pawar, V. R.**, & Sobhansarbandi, S. (2021, July). Performance Optimization of Thermal Energy Storage Based Solar Collector. In ASME Power Conference (Vol. 85109, p. V001T12A005). American Society of Mechanical Engineers. **Received Best Student Paper Award.**

  DOI: https://doi.org/10.1115/POWER2021-64127

- **Pawar, V. R.**, Siddiki, M. K., & Sobhansarbandi, S. (2021, June). Numerical Analysis of a Photovoltaic-Thermal Solar Collector With PCM Embedded in Highly Conductive Porous Material. In Heat Transfer Summer Conference (Vol. 84874, p. V001T07A005). American Society of Mechanical Engineers.

  DOI: https://doi.org/10.1115/HT2021-62974

- Lim, C. S., **Pawar, V. R.**, & Sobhansarbandi, S. (2020, June). Thermal Performance Analysis of a Novel U-Tube Evacuated Tube Solar Collector. In Energy Sustainability (Vol. 83631, p. V001T08A002). American Society of Mechanical Engineers.

  DOI: https://doi.org/10.1115/ES2020-1674

- **Pawar, V. R.**, & Sobhansarbandi, S. (2019, November). Computational Fluid Dynamics Modeling of a Heat Pipe Evacuated Tube Solar Collector Integrated With Phase Change Material. In ASME International Mechanical Engineering Congress and Exposition (Vol. 59438, p. V006T06A087). American Society of Mechanical Engineers.

DOI: https://doi.org/10.1115/IMECE2019-10252

- Mahdavi, M., **Pawar, V.**, & Sawyer, C. (2019). ON THE EFFECTS OF POROUS INSERTS ON THE IMPROVEMENT OF LATENT HEAT THERMAL ENERGY STORAGE SYSTEMS CHARGING PERFORMANCE. In ASTFE Digital Library. DOI: 10.1615/TFEC2019.tes.028102

- Mahdavi, M., Tiari, S., & **Pawar, V.** (2018, November). Heat Transfer Analysis of a Low-Temperature Heat Pipe-Assisted Latent Heat Thermal Energy Storage System With Nano-Enhanced PCM. In ASME International Mechanical Engineering Congress and Exposition (Vol. 52088, p. V06BT08A051). American Society of Mechanical Engineers.
  DOI: https://doi.org/10.1115/IMECE2018-86609

- Mahdavi, M., Tiari, S., Solanki, A., & **Pawar, V.** (2018, November). Numerical Study on the Performance Characteristics of Cylindrical Heat Pipes With Differing Wick Type. In ASME International Mechanical Engineering Congress and Exposition (Vol. 52125, p. V08BT10A062). American Society of Mechanical Engineers.
  DOI: https://doi.org/10.1115/IMECE2018-86607

REFERENCE LIST

[1] Best Research-Cell Efficiency, Chart Photovoltaics Research, NREL. *https://www.nrel.gov/pv/cell-efficiency.html*.

[2] Photovoltaics Research and Development, Energy Efficiency and Renewable Energy. *https://www.energy.gov/eere/solar/photovoltaics-research-and-development*.

[3] Abokersh, M. H., El-Morsi, M., Sharaf, O., and Abdelrahman, W. An experimental evaluation of direct flow evacuated tube solar collector integrated with phase change material. *Energy 139* (2017), 1111–1125.

[4] Abokersh, M. H., El-Morsi, M., Sharaf, O., and Abdelrahman, W. On-demand operation of a compact solar water heater based on U-pipe evacuated tube solar collector combined with phase change material. *Solar Energy 155* (2017), 1130–1147.

[5] Aggarwal, V. Solar Panel Efficiency: What Panels Are Most Efficient: EnergySage. *https://news.energysage.com/what-are-the-most-efficient-solar-panels-on-the-market*.

[6] Agrawal, S., and Tiwari, G. Energy and exergy analysis of hybrid micro-channel photovoltaic thermal module. *Solar Energy 85*, 2 (2011), 356–370.

[7] Agyenim, F., Eames, P., and Smyth, M. A comparison of heat transfer enhancement in a medium temperature thermal energy storage heat exchanger using fins. *Solar Energy 83*, 9 (2009), 1509–1520.

[8] Ahmed, O. K., and Mohammed, Z. A. Influence of porous media on the performance of hybrid PV/Thermal collector. *Renewable Energy 112* (2017), 378–387.

[9] Al-Shamani, A. N., Sopian, K., Mat, S., Hasan, H. A., Abed, A. M., and Ruslan, M. Experimental studies of rectangular tube absorber photovoltaic thermal collector with various types of nanofluids under the tropical climate conditions. *Energy Conversion and Management 124* (2016), 528–542.

[10] Alammar, A. A., Al-Dadah, R. K., and Mahmoud, S. M. Numerical investigation of effect of fill ratio and inclination angle on a thermosiphon heat pipe thermal performance. *Applied Thermal Engineering 108* (2016), 1055–1065.

[11] Ali, H. M. Applications of combined/hybrid use of heat pipe and phase change materials in energy storage and cooling systems: A recent review. *Journal of Energy Storage 26* (2019), 100986.

[12] Alsema, E. Energy payback time and CO2 emissions of PV systems. In *Practical Handbook of Photovoltaics*. Elsevier, 2012, pp. 1097–1117.

[13] Alva, G., Lin, Y., and Fang, G. An overview of thermal energy storage systems. *Energy 144* (2018), 341–378.

[14] Apricus. AP Evacuated Tube Solar Collector. *https://www.apricus.com/ETC-30-Solar-Collector-pd43215927.html*.

[15] Aquing, M., Ciotta, F., Creton, B., Fejean, C., Pina, A., Dartiguelongue, C., Trusler, J. M., Vignais, R., Lugo, R., Ungerer, P., et al. Composition analysis and viscosity prediction of complex fuel mixtures using a molecular-based approach. *Energy & Fuels 26*, 4 (2012), 2220–2230.

[16] Aramesh, M., and Shabani, B. On the integration of phase change materials with evacuated tube solar thermal collectors. *Renewable and Sustainable Energy Reviews 132* (2020), 110135.

[17] Ayompe, L., Duffy, A., Mc Keever, M., Conlon, M., and McCormack, S. Comparative field performance study of flat plate and heat pipe evacuated tube collectors (ETCs) for domestic water heating systems in a temperate climate. *Energy 36*, 5 (2011), 3370–3378.

[18] Barrak, A. Heat Pipes Heat Exchanger for HVAC Applications. In *Heat Transfer-Design, Experimentation and Applications*. IntechOpen, 2021.

[19] Beiginaloo, G., Mohebbi, A., and Afsahi, M. M. Combination of CFD and DOE for optimization of thermosyphon heat pipe. *Heat and Mass Transfer* (2021), 1–14.

[20] Benbrika, M., Teggar, M., Arıcı, M., Ismail, K. A., Bouabdallah, S., and Mezaache, E.-H. Effect of graphene nanoparticles on charging and discharging processes of

latent thermal energy storage using horizontal cylinders. *Sustainable Energy Technologies and Assessments 45* (2021), 101242.

[21] Brackbill, J. U., Kothe, D. B., and Zemach, C. A continuum method for modeling surface tension. *Journal of Computational Physics 100*, 2 (1992), 335–354.

[22] Browne, M. C., Lawlor, K., Kelly, A., Norton, B., and Mc Cormack, S. J. Indoor characterisation of a photovoltaic/thermal phase change material system. *Energy Procedia 70* (2015), 163–171.

[23] Browne, M. C., Norton, B., and McCormack, S. J. Heat retention of a photovoltaic/thermal collector with PCM. *Solar Energy 133* (2016), 533–548.

[24] Browne, M. C., Quigley, D., Hard, H. R., Gilligan, S., Ribeiro, N. C., Almeida, N., and McCormack, S. J. Assessing the thermal performance of phase change material in a photovoltaic/thermal system. *Energy Procedia 91* (2016), 113–121.

[25] Budihardjo, I., and Morrison, G. Performance of water-in-glass evacuated tube solar water heaters. *Solar Energy 83*, 1 (2009), 49–56.

[26] Cao, X., Dai, X., and Liu, J. Building energy-consumption status worldwide and the state-of-the-art technologies for zero-energy buildings during the past decade. *Energy and Buildings 128* (2016), 198–213.

[27] Cassard, H., Denholm, P., and Ong, S. Break-even cost for residential solar water heating in the United States: key drivers and sensitivities. Tech. rep., National Renewable Energy Lab.(NREL), Golden, CO (United States), 2011.

[28] Center, F. S. E., and Fenaughty, K. Connected Water Heater Load Shifting and Energy Efficiency Evaluation for the Southeast: Winter Laboratory Assessment, Final Report. *https://stars.library.ucf.edu/fsec/1* (2021).

[29] Chen, X., Li, X., Xia, X., Sun, C., and Liu, R. Thermal performance of a pcm-based thermal energy storage with metal foam enhancement. *Energies 12*, 17 (2019), 3275.

[30] Chopra, K., Pathak, A. K., Tyagi, V., Pandey, A., Anand, S., and Sari, A. Thermal performance of phase change material integrated heat pipe evacuated tube solar collector system: An experimental assessment. *Energy Conversion and Management 203* (2020), 112205.

[31] Chopra, K., Tyagi, V., Pandey, A., and Sari, A. Global advancement on experimental and thermal analysis of evacuated tube collector with and without heat pipe systems and possible applications. *Applied Energy 228* (2018), 351–389.

[32] Chopra, K., Tyagi, V., Pandey, A., Sharma, R., and Sari, A. PCM integrated glass in glass tube solar collector for low and medium temperature applications: Thermodynamic & techno-economic approach. *Energy* (2020), 117238.

[33] Chopra, K., Tyagi, V., Pathak, A. K., Pandey, A., and Sari, A. Experimental performance evaluation of a novel designed phase change material integrated manifold heat pipe evacuated tube solar collector system. *Energy Conversion and Management 198* (2019), 111896.

[34] Chow, T. Performance analysis of photovoltaic-thermal collector by explicit dynamic model. *Solar Energy 75*, 2 (2003), 143–152.

[35] Churchill, S., and Bernstein, M. A correlating equation for forced convection from gases and liquids to a circular cylinder in crossflow. *Journal of Heat Transfer 99*, 2 (05 1977), 300–306.

[36] Çimen, M., Colakoglu, M., and Güngör, A. Overheating limitation of thermosiphon solar collectors by controlling heat pipe fluid in all glass evacuated tubes. *Solar Energy 230* (2021), 515–527.

[37] Daghigh, R., and Shafieian, A. Energy and exergy evaluation of an integrated solar heat pipe wall system for space heating. *Sādhanā 41*, 8 (2016), 877–886.

[38] Daghigh, R., and Shafieian, A. Theoretical and experimental analysis of thermal performance of a solar water heating system with evacuated tube heat pipe collector. *Applied Thermal Engineering 103* (2016), 1219–1227.

[39] Das, L., Habib, K., Saidur, R., Aslfattahi, N., Yahya, S. M., and Rubbi, F. Improved thermophysical properties and energy efficiency of aqueous ionic liquid/MXene nanofluid in a hybrid PV/T solar system. *Nanomaterials 10*, 7 (2020), 1372.

[40] De Schepper, S. C., Heynderickx, G. J., and Marin, G. B. CFD modeling of all gas–liquid and vapor–liquid flow regimes predicted by the Baker chart. *Chemical Engineering Journal 138*, 1-3 (2008), 349–357.

[41] De Schepper, S. C., Heynderickx, G. J., and Marin, G. B. Modeling the evaporation of a hydrocarbon feedstock in the convection section of a steam cracker. *Computers & Chemical Engineering 33*, 1 (2009), 122–132.

[42] del Barrio, E. P., Godin, A., Duquesne, M., Daranlot, J., Jolly, J., Alshaer, W., Kouadio, T., and Sommier, A. Characterization of different sugar alcohols as phase change materials for thermal energy storage applications. *Solar Energy Materials and Solar Cells 159* (2017), 560–569.

[43] Dhaidan, N. S., Kokz, S. A., Rashid, F. L., Hussein, A. K., Younis, O., and Al-Mousawi, F. N. Review of solidification of phase change materials dispersed with nanoparticles in different containers. *Journal of Energy Storage 51* (2022), 104271.

[44] El-Nasr, A. A., and El-Haggar, S. Effective thermal conductivity of heat pipes. *Heat and Mass Transfer 32*, 1-2 (1996), 97–101.

[45] Ersöz, M. A. Effects of different working fluid use on the energy and exergy performance for evacuated tube solar collector with thermosyphon heat pipe. *Renewable Energy 96* (2016), 244–256.

[46] Essa, M. A., and Mostafa, N. H. Theoretical and experimental study for temperature distribution and flow profile in all water evacuated tube solar collector considering solar radiation boundary condition. *Solar Energy 142* (2017), 267–277.

[47] Essa, M. A., Mostafa, N. H., and Ibrahim, M. M. An experimental investigation of the phase change process effects on the system performance for the evacuated tube solar collectors integrated with PCMs. *Energy Conversion and Management 177* (2018), 1–10.

[48] Essa, M. A., Rofaiel, I. Y., and Ahmed, M. A. Experimental and theoretical analysis for the performance of evacuated tube collector integrated with helical finned heat pipes using PCM energy storage. *Energy* (2020), 118166.

[49] Fadhl, B., Wrobel, L. C., and Jouhara, H. Numerical modelling of the temperature distribution in a two-phase closed thermosyphon. *Applied Thermal Engineering 60*, 1-2 (2013), 122–131.

[50] Faegh, M., and Shafii, M. B. Experimental investigation of a solar still equipped with an external heat storage system using phase change materials and heat pipes. *Desalination 409* (2017), 128–135.

[51] Faghri, A. *Heat pipe science and technology*. Global Digital Press, 1995.

[52] Faghri, A. Heat pipes: review, opportunities and challenges. *Frontiers in Heat Pipes (FHP) 5*, 1 (2014).

[53] Fang, Y., Ding, Y., Tang, Y., Liang, X., Jin, C., Wang, S., Gao, X., and Zhang, Z. Thermal properties enhancement and application of a novel sodium acetate trihydrate-formamide/expanded graphite shape-stabilized composite phase change

material for electric radiant floor heating. *Applied Thermal Engineering 150* (2019), 1177–1185.

[54] Feliński, P., and Sekret, R. Experimental study of evacuated tube collector/storage system containing paraffin as a PCM. *Energy 114* (2016), 1063–1072.

[55] Feliński, P., and Sekret, R. Effect of PCM application inside an evacuated tube collector on the thermal performance of a domestic hot water system. *Energy and Buildings 152* (2017), 558–567.

[56] Finlayson, E. U., Arasteh, D. K., Huizenga, C., Rubin, M. D., and Reilly, M. WINDOW 4.0: Documentation of calculation procedures. *https://facades.lbl.gov/publications/window-40-documentation-calculation* (1993).

[57] Fluent. FLUENT 6.3 user's guide. *https://forum.ansys.com/discussion/13811/ansys-fluent-2020-r1-theory-guide-user-guide-full-pdf* (2006).

[58] Fudholi, A., Sopian, K., Yazdi, M. H., Ruslan, M. H., Ibrahim, A., and Kazem, H. A. Performance analysis of photovoltaic thermal (PVT) water collectors. *Energy Conversion and Management 78* (2014), 641–651.

[59] Gao, Y., Fan, R., Zhang, X., An, Y., Wang, M., Gao, Y., and Yu, Y. Thermal performance and parameter analysis of a U-pipe evacuated solar tube collector. *Solar Energy 107* (2014), 714–727.

[60] Gernaat, D. E., de Boer, H. S., Daioglou, V., Yalew, S. G., Müller, C., and van Vuuren, D. P. Climate change impacts on renewable energy supply. *Nature Climate Change 11*, 2 (2021), 119–125.

[61] Ghahremannezhad, A., Xu, H., Salimpour, M. R., Wang, P., and Vafai, K. Thermal performance analysis of phase change materials (PCMs) embedded in gradient porous metal foams. *Applied Thermal Engineering 179* (2020), 115731.

[62] Greco, A., Gundabattini, E., Gnanaraj, D. S., and Masselli, C. A comparative study on the performances of flat plate and evacuated tube collectors deployable in domestic solar water heating systems in different climate areas. *Climate 8*, 6 (2020), 78.

[63] Guerraiche, D., Bougriou, C., Guerraiche, K., Valenzuela, L., and Driss, Z. Experimental and numerical study of a solar collector using phase change material as heat storage. *Journal of Energy Storage 27* (2020), 101133.

[64] Harrison, S., and Cruickshank, C. A. A review of strategies for the control of high temperature stagnation in solar collectors and systems. *Energy Procedia 30* (2012), 793–804.

[65] Hasan, H. A., Sopian, K., Jaaz, A. H., and Al-Shamani, A. N. Experimental investigation of jet array nanofluids impingement in photovoltaic/thermal collector. *Solar Energy 144* (2017), 321–334.

[66] Heidari, A., and Khovalyg, D. Short-term energy use prediction of solar-assisted water heating system: Application case of combined attention-based LSTM and time-series decomposition. *Solar Energy 207* (2020), 626–639.

[67] Herrmann, U., and Kearney, D. W. Survey of thermal energy storage for parabolic trough power plants. *Journal of Solar Energy Engineering 124*, 2 (2002), 145–152.

[68] Höhlein, S., König-Haagen, A., and Brüggemann, D. Thermophysical characterization of MgCl2· 6H2O, xylitol and erythritol as phase change materials (PCM) for latent heat thermal energy storage (LHTES). *Materials 10*, 4 (2017), 444.

[69] Huang, M., Eames, P., and Norton, B. Phase change materials for limiting temperature rise in building integrated photovoltaics. *Solar Energy 80*, 9 (2006), 1121–1130.

[70] Huang, X., Wang, Q., Yang, H., Zhong, S., Jiao, D., Zhang, K., Li, M., and Pei, G. Theoretical and experimental studies of impacts of heat shields on heat pipe evacuated tube solar collector. *Renewable Energy 138* (2019), 999–1009.

[71] Hussain, F., Othman, M., Yatim, B., Ruslan, H., Sopian, K., Anuar, Z., and Khairuddin, S. An improved design of photovoltaic/thermal solar collector. *Solar Energy 122* (2015), 885–891.

[72] Ibrahim, N. I., Al-Sulaiman, F. A., Rahman, S., Yilbas, B. S., and Sahin, A. Z. Heat transfer enhancement of phase change materials for thermal energy storage

applications: A critical review. *Renewable and Sustainable Energy Reviews 74* (2017), 26–50.

[73] Javadi, F., Metselaar, H., and Ganesan, P. Performance improvement of solar thermal systems integrated with phase change materials (PCM), a review. *Solar Energy 206* (2020), 330–352.

[74] Jayanthi, N., Kumar, R. S., Karunakaran, G., and Venkatesh, M. Experimental investigation on the thermal performance of heat pipe solar collector (HPSC). *Materials Today: Proceedings 26* (2020), 3569–3575.

[75] Jegadheeswaran, S., and Pohekar, S. D. Performance enhancement in latent heat thermal storage system: a review. *Renewable and Sustainable Energy Reviews 13*, 9 (2009), 2225–2244.

[76] Jia, Y., Ran, F., Zhu, C., and Fang, G. Numerical analysis of photovoltaic-thermal collector using nanofluid as a coolant. *Solar Energy 196* (2020), 625–636.

[77] Joshi, V., and Rathod, M. K. Experimental and numerical assessments of thermal transport in fins and metal foam infused latent heat thermal energy storage systems: a comparative evaluation. *Applied Thermal Engineering 178* (2020), 115518.

[78] Jouhara, H., Fadhl, B., and Wrobel, L. C. Three-dimensional CFD simulation of geyser boiling in a two-phase closed thermosyphon. *International Journal of Hydrogen Energy 41*, 37 (2016), 16463–16476.

[79] Kalidasan, B., Pandey, A., Shahabuddin, S., Samykano, M., Thirugnanasambandam, M., and Saidur, R. Phase change materials integrated solar thermal energy systems: Global trends and current practices in experimental approaches. *Journal of Energy Storage 27* (2020), 101118.

[80] Kazemian, A., Salari, A., Hakkaki-Fard, A., and Ma, T. Numerical investigation and parametric analysis of a photovoltaic thermal system integrated with phase change material. *Applied Energy 238* (2019), 734–746.

[81] Khalid, S. U., Babar, H., Ali, H. M., Janjua, M. M., and Ali, M. A. Heat pipes: progress in thermal performance enhancement for microelectronics. *Journal of Thermal Analysis and Calorimetry 143*, 3 (2021), 2227–2243.

[82] Khanjari, Y., Kasaeian, A., and Pourfayaz, F. Evaluating the environmental parameters affecting the performance of photovoltaic thermal system using nanofluid. *Applied Thermal Engineering 115* (2017), 178–187.

[83] Khanna, S., Reddy, K., and Mallick, T. K. Performance analysis of tilted photovoltaic system integrated with phase change material under varying operating conditions. *Energy 133* (2017), 887–899.

[84] Khodadadi, M., and Sheikholeslami, M. Numerical simulation on the efficiency of PVT system integrated with PCM under the influence of using fins. *Solar Energy Materials and Solar Cells 233* (2021), 111402.

[85] Kothari, R., Sahu, S., Kundalwal, S. I., and Sahoo, S. Experimental investigation of the effect of inclination angle on the performance of phase change material based finned heat sink. *Journal of Energy Storage 37* (2021), 102462.

[86] Lane, G. A., and Lane, G. *Solar heat storage: latent heat materials*, vol. 1. CRC press Boca Raton, FL, USA:, 1983.

[87] Legierski, J., Wie, B., De Mey, G., et al. Measurements and simulations of transient characteristics of heat pipes. *Microelectronics Reliability 46*, 1 (2006), 109–115.

[88] Lhuillier, D. A mean-field description of two-phase flows with phase changes. *International Journal of Multiphase Flow 29*, 3 (2003), 511–525.

[89] Li, B., and Zhai, X. Experimental investigation and theoretical analysis on a mid-temperature solar collector/storage system with composite PCM. *Applied Thermal Engineering 124* (2017), 34–43.

[90] Li, B., Zhai, X., and Cheng, X. Experimental and numerical investigation of a solar collector/storage system with composite phase change materials. *Solar Energy 164* (2018), 65–76.

[91] Li, L., Yu, H., Li, Y., and He, Y.-L. Characteristics of the transient thermal load and deformation of the evacuated receiver in solar parabolic trough collector. *Science China Technological Sciences 63* (2020), 1188–1201.

[92] Li, W., Qu, Z., He, Y., and Tao, W. Experimental and numerical studies on melting phase change heat transfer in open-cell metallic foams filled with paraffin. *Applied Thermal Engineering 37* (2012), 1–9.

[93] Li, Z., Chen, C., Luo, H., Zhang, Y., and Xue, Y. All-glass vacuum tube collector heat transfer model used in forced-circulation solar water heating system. *Solar Energy 84*, 8 (2010), 1413–1421.

[94] Liang, R., Ma, L., Zhang, J., and Zhao, D. Theoretical and experimental investigation of the filled-type evacuated tube solar collector with U tube. *Solar Energy 85*, 9 (2011), 1735–1744.

[95] Lim, C. S., Weaver, R., and Sobhansarbandi, S. Heat Transfer Enhancement of Phase Change Materials for Thermal Energy Storage Systems. In *ASME 2019 Power Conference* (2019), American Society of Mechanical Engineers Digital Collection.

[96] Liu, Z., Yao, Y., and Wu, H. Numerical modeling for solid–liquid phase change phenomena in porous media: Shell-and-tube type latent heat thermal energy storage. *Applied Energy 112* (2013), 1222–1232.

[97] Mahdavi, M., Tiari, S., and Pawar, V. A numerical study on the combined effect of dispersed nanoparticles and embedded heat pipes on melting and solidification of a shell and tube latent heat thermal energy storage system. *Journal of Energy Storage 27* (2020), 101086.

[98] Mahdi, J. M., and Nsofor, E. C. Solidification of a PCM with nanoparticles in triplex-tube thermal energy storage system. *Applied Thermal Engineering 108* (2016), 596–604.

[99] Masoumi, H., Mirfendereski, S., et al. Experimental and numerical investigation of melting/solidification of nano-enhanced phase change materials in shell & tube thermal energy storage systems. *Journal of Energy Storage 47* (2022), 103561.

[100] Meghari, Z., Bouhal, T., Benghoulam, M., El Rhafiki, T., Mohammed, O. J., et al. Numerical simulation of a phase change material in a spherical capsule with a hollow fin. *Journal of Energy Storage 43* (2021), 103024.

[101] Mehta, D. S., Vaghela, B., Rathod, M. K., and Banerjee, J. Thermal performance augmentation in latent heat storage unit using spiral fin: an experimental analysis. *Journal of Energy Storage 31* (2020), 101776.

[102] Mofijur, M., Mahlia, T. M. I., Silitonga, A. S., Ong, H. C., Silakhori, M., Hasan, M. H., Putra, N., and Rahman, S. Phase change materials (PCM) for solar energy usages and storage: An overview. *Energies 12*, 16 (2019), 3167.

[103] Mojumder, J. C., Chong, W. T., Ong, H. C., Leong, K., et al. An experimental investigation on performance analysis of air type photovoltaic thermal collector system integrated with cooling fins design. *Energy and Buildings 130* (2016), 272–285.

[104] Morrison, G., Budihardjo, I., and Behnia, M. Water-in-glass evacuated tube solar water heaters. *Solar Energy 76*, 1-3 (2004), 135–140.

[105] Mousavi, S., Kasaeian, A., Shafii, M. B., and Jahangir, M. H. Numerical investigation of the effects of a copper foam filled with phase change materials in a water-cooled photovoltaic/thermal system. *Energy Conversion and Management 163* (2018), 187–195.

[106] Muzhanje, A. T., Hassan, M., Ookawara, S., and Hassan, H. An overview of the preparation and characteristics of phase change materials with nanomaterials. *Journal of Energy Storage 51* (2022), 104353.

[107] Naghavi, M., Metselaar, H., Ang, B., Zamiri, G., Esmailzadeh, A., and Nasiri-Tabrizi, B. A critical assessment on synergistic improvement in PCM based thermal batteries. *Renewable and Sustainable Energy Reviews 135* (2021), 110259.

[108] Naghavi, M., Ong, K., Badruddin, I., Mehrali, M., and Metselaar, H. Thermal performance of a compact design heat pipe solar collector with latent heat storage in charging/discharging modes. *Energy 127* (2017), 101–115.

[109] Naik, B. K., Varshney, A., Muthukumar, P., and Somayaji, C. Modelling and performance analysis of U type evacuated tube solar collector using different working fluids. *Energy Procedia 90* (2016), 227–237.

[110] Naldi, C., Dongellini, M., and Morini, G. L. The evaluation of the effective thermal conductivity of metal-foam loaded phase change materials. *Journal of Energy Storage 51* (2022), 104450.

[111] Navarro, L., Barreneche, C., Castell, A., Redpath, D. A., Griffiths, P. W., and Cabeza, L. F. High density polyethylene spheres with PCM for domestic hot water applications: Water tank and laboratory scale study. *Journal of Energy Storage 13* (2017), 262–267.

[112] Neupauer, K., and Magiera, J. A vacuum in a solar collector reducing the heat lost from convection and conductivity way. *Technical Transactions 10* (2011), 223–232.

[113] Nithyanandam, K., and Pitchumani, R. Analysis and optimization of a latent thermal energy storage system with embedded heat pipes. *International Journal of Heat and Mass Transfer 54*, 21-22 (2011), 4596–4610.

[114] Olczak, P., and Olek, M. The influence of evacuated-tube collector assembly on heat loss in tracking solar system with parabolic mirror reflectors. *Procedia Engineering 157* (2016), 317–324.

[115] Olfian, H., Ajarostaghi, S. S. M., and Ebrahimnataj, M. Development on evacuated tube solar collectors: A review of the last decade results of using nanofluids. *Solar Energy 211* (2020), 265–282.

[116] Papadimitratos, A., Sobhansarbandi, S., Pozdin, V., Zakhidov, A., and Hassanipour, F. Evacuated tube solar collectors integrated with phase change materials. *Solar Energy 129* (2016), 10–19.

[117] Patel, J. R., Rathod, M. K., and Sheremet, M. Heat transfer augmentation of triplex type latent heat thermal energy storage using combined eccentricity and longitudinal fin. *Journal of Energy Storage 50* (2022), 104167.

[118] Pawar, V. R., and Sobhansarbandi, S. CFD modeling of a thermal energy storage based heat pipe evacuated tube solar collector. *Journal of Energy Storage 30* (2020), 101528.

[119] Pawar, V. R., and Sobhansarbandi, S. Design optimization and heat transfer enhancement of energy storage based solar thermal collector. *Sustainable Energy Technologies and Assessments 46* (2021), 101260.

[120] Phanikumar, M., and Mahajan, R. Non-Darcy natural convection in high porosity metal foams. *International Journal of Heat and Mass Transfer 45*, 18 (2002), 3781–3793.

[121] Rad, M. A. V., Kasaeian, A., Mousavi, S., Rajaee, F., and Kouravand, A. Empirical investigation of a photovoltaic-thermal system with phase change materials and aluminum shavings porous media. *Renewable Energy 167* (2021), 662–675.

[122] Radziemska, E., and Klugmann, E. Thermally affected parameters of the current–voltage characteristics of silicon photocell. *Energy Conversion and Management 43*, 14 (2002), 1889–1900.

[123] Rathod, M. K., and Banerjee, J. Thermal performance enhancement of shell and tube Latent Heat Storage Unit using longitudinal fins. *Applied Thermal Engineering 75* (2015), 1084–1092.

[124] Reay, D., McGlen, R., and Kew, P. *Heat pipes: theory, design and applications*. Butterworth-Heinemann, 2013.

[125] Salari, A., Kazemian, A., Ma, T., Hakkaki-Fard, A., and Peng, J. Nanofluid based photovoltaic thermal systems integrated with phase change materials: Numerical simulation and thermodynamic analysis. *Energy Conversion and Management 205* (2020), 112384.

[126] Salem, M., Ali, R., and Elshazly, K. Experimental investigation of the performance of a hybrid photovoltaic/thermal solar system using aluminium cooling plate with straight and helical channels. *Solar Energy 157* (2017), 147–156.

[127] Salunkhe, P. B., et al. Investigations on latent heat storage materials for solar water and space heating applications. *Journal of Energy Storage 12* (2017), 243–260.

[128] Sardarabadi, M., and Passandideh-Fard, M. Experimental and numerical study of metal-oxides/water nanofluids as coolant in photovoltaic thermal systems (PVT). *Solar Energy Materials and Solar Cells 157* (2016), 533–542.

[129] Saydam, V., and Duan, X. Dispersing different nanoparticles in paraffin wax as enhanced phase change materials. *Journal of Thermal Analysis and Calorimetry 135*, 2 (2019), 1135–1144.

[130] Sekret, R., and Feliński, P. The impact of ETC/PCM solar energy storage on the energy performance of a building. In *E3S Web of Conferences* (2019), vol. 116, EDP Sciences, p. 00073.

[131] Sengupta, M., Xie, Y., Lopez, A., Habte, A., Maclaurin, G., and Shelby, J. The national solar radiation data base (NSRDB). *Renewable and Sustainable Energy Reviews 89* (2018), 51–60.

[132] Senthil, R., Elavarasan, R. M., Pugazhendhi, R., Premkumar, M., Vengadesan, E., Navakrishnan, S., Islam, M. R., and Natarajan, S. K. A holistic review on the integration of heat pipes in solar thermal and photovoltaic systems. *Solar Energy 227* (2021), 577–605.

[133] Shafieian, A., Khiadani, M., and Nosrati, A. A review of latest developments, progress, and applications of heat pipe solar collectors. *Renewable and Sustainable Energy Reviews 95* (2018), 273–304.

[134] Shafieian, A., Khiadani, M., and Nosrati, A. Strategies to improve the thermal performance of heat pipe solar collectors in solar systems: A review. *Energy Conversion and Management 183* (2019), 307–331.

[135] Shafieian, A., Khiadani, M., and Nosrati, A. Thermal performance of an evacuated tube heat pipe solar water heating system in cold season. *Applied Thermal Engineering 149* (2019), 644–657.

[136] Shafieian, A., Osman, J. J., Khiadani, M., and Nosrati, A. Enhancing heat pipe solar water heating systems performance using a novel variable mass flow rate technique and different solar working fluids. *Solar Energy 186* (2019), 191–203.

[137] Shafieian, A., Parastvand, H., and Khiadani, M. Comparative and performative investigation of various data-based and conventional theoretical methods for modelling heat pipe solar collectors. *Solar Energy 198* (2020), 212–223.

[138] Sharma, R., Gupta, A., Nandan, G., Dwivedi, G., and Kumar, S. Life span and overall performance enhancement of solar photovoltaic cell using water as coolant: a recent review. *Materials Today: Proceedings 5*, 9 (2018), 18202–18210.

[139] Shukla, A., Buddhi, D., and Sawhney, R. Thermal cycling test of few selected inorganic and organic phase change materials. *Renewable Energy 33*, 12 (2008), 2606–2614.

[140] Shukla, A., Buddhi, D., and Sawhney, R. Solar water heaters with phase change material thermal energy storage medium: A review. *Renewable and Sustainable Energy Reviews 13*, 8 (2009), 2119–2125.

[141] Singh, S. K., Verma, S. K., and Kumar, R. Thermal performance and behavior analysis of SiO2, Al2O3 and MgO based nano-enhanced phase-changing materials,

latent heat thermal energy storage system. *Journal of Energy Storage 48* (2022), 103977.

[142] Siuta-Olcha, A., Cholewa, T., and Dopieralska-Howoruszko, K. Experimental studies of thermal performance of an evacuated tube heat pipe solar collector in Polish climatic conditions. *Environmental Science and Pollution Research* (2020), 1–10.

[143] Sivasamy, P., Harikrishnan, S., Jayavel, R., Hussain, S. I., Kalaiselvam, S., and Lu, L. Preparation and thermal characteristics of caprylic acid based composite as phase change material for thermal energy storage. *Materials Research Express 6*, 10 (2019), 105051.

[144] Smets, A., Jäger, K., Isabella, O., van Swaaij, R., and Zeman, M. *Solar Energy: The Physics and Engineering of Photovoltaic Conversion, Technologies and Systems*. UIT Cambridge, 2016.

[145] Sobhansarbandi, S., Martinez, P. M., Papadimitratos, A., Zakhidov, A., and Hassanipour, F. Evacuated tube solar collector with multifunctional absorber layers. *Solar Energy 146* (2017), 342–350.

[146] Sokhansefat, T., Kasaeian, A., Rahmani, K., Heidari, A. H., Aghakhani, F., and Mahian, O. Thermoeconomic and environmental analysis of solar flat plate and evacuated tube collectors in cold climatic conditions. *Renewable Energy 115* (2018), 501–508.

[147] Solé, A., Neumann, H., Niedermaier, S., Martorell, I., Schossig, P., and Cabeza, L. F. Stability of sugar alcohols as PCM for thermal energy storage. *Solar Energy Materials and Solar Cells 126* (2014), 125–134.

[148] Su, D., Jia, Y., Lin, Y., and Fang, G. Maximizing the energy output of a photovoltaic–thermal solar collector incorporating phase change materials. *Energy and Buildings 153* (2017), 382–391.

[149] Sudheer, R., and Prabhu, K. Cooling Curve Analysis of Micro-and Nanographite Particle-Embedded Salt-PCMs for Thermal Energy Storage Applications. *Journal of Materials Engineering and Performance 26*, 8 (2017), 4040–4045.

[150] Sukarno, R., Putra, N., Hakim, I. I., Rachman, F. F., and Mahlia, T. M. I. Multistage heat-pipe heat exchanger for improving energy efficiency of the HVAC system in a hospital operating room. *International Journal of Low-Carbon Technologies 16*, 2 (2021), 259–267.

[151] Sukhatme, K., and Sukhatme, S. Solar Energy: Principles of Thermal Collection and Storage. *https://books.google.com/books?id=l-XHcwZo9XwC* (1996).

[152] Tamuli, B. R., Saikia, S. S., Nath, S., and Bhanja, D. Thermal performance analysis of a co-axial evacuated tube collector with single and two-phase flow consideration under North-eastern India climatic condition. *Solar Energy 196* (2020), 107–124.

[153] Tascioni, R., Arteconi, A., Del Zotto, L., and Cioccolanti, L. Fuzzy Logic Energy Management Strategy of a Multiple Latent Heat Thermal Storage in a Small-Scale Concentrated Solar Power Plant. *Energies 13*, 11 (2020), 2733.

[154] Thyrum, G., and Herda, A. N. Critical aspects of modeling heat pipe assisted heat sinks. *Thermacore* (1999), 101–115.

[155] Tian, Y., and Zhao, C.-Y. A numerical investigation of heat transfer in phase change materials (PCMs) embedded in porous metals. *Energy 36*, 9 (2011), 5539–5546.

[156] Tiari, S., and Qiu, S. Three-dimensional simulation of high temperature latent heat thermal energy storage system assisted by finned heat pipes. *Energy Conversion and Management 105* (2015), 260–271.

[157] Tyagi, V., Pandey, A., Giridhar, G., Bandyopadhyay, B., Park, S., and Tyagi, S. Comparative study based on exergy analysis of solar air heater collector using thermal energy storage. *International Journal of Energy Research 36*, 6 (2012), 724–736.

[158] Vo, D.-T., Kim, H.-T., Ko, J., and Bang, K.-H. An experiment and three-dimensional numerical simulation of pulsating heat pipes. *International Journal of Heat and Mass Transfer 150* (2020), 119317.

[159] Voller, V., and Prakash, C. A fixed grid numerical modelling methodology for convection-diffusion mushy region phase-change problems. *International Journal of Heat and Mass Transfer 30*, 8 (1987), 1709 – 1719.

[160] Wang, Q., Chen, H., Wang, Y., and Sun, J. Thermal shock effect on the glass thermal stress response and crack propagation. *Procedia Engineering 62* (2013), 717–724.

[161] Wang, T., Diao, Y., Zhao, Y., Liang, L., Wang, Z., and Chen, C. A comparative experimental investigation on thermal performance for two types of vacuum tube solar air collectors based on flat micro-heat pipe arrays (FMHPA). *Solar Energy 201* (2020), 508–522.

[162] Wang, T.-y., Zhao, Y.-h., Diao, Y.-h., Ren, R.-y., and Wang, Z.-y. Performance of a new type of solar air collector with transparent-vacuum glass tube based on micro-heat pipe arrays. *Energy 177* (2019), 16–28.

[163] Wang, Y., Gao, Y., Huang, Q., Hu, G., and Zhou, L. Experimental study of active phase change cooling technique based on porous media for photovoltaic thermal management and efficiency enhancement. *Energy Conversion and Management 199* (2019), 111990.

[164] Wang, Y., Wang, L., Xie, N., Lin, X., and Chen, H. Experimental study on the melting and solidification behavior of erythritol in a vertical shell-and-tube latent heat thermal storage unit. *International Journal of Heat and Mass Transfer 99* (2016), 770–781.

[165] Wang, Z., Diao, Y., Zhao, Y., Chen, C., Liang, L., and Wang, T. Thermal performance of integrated collector storage solar air heater with evacuated tube and lap joint-type flat micro-heat pipe arrays. *Applied Energy 261* (2020), 114–466.

[166] Wang, Z., Diao, Y., Zhao, Y., Chen, C., Liang, L., and Wang, T. Thermal performance of integrated collector storage solar air heater with evacuated tube and lap joint-type flat micro-heat pipe arrays. *Applied Energy 261* (2020), 114466.

[167] Wu, H., Peng, X., Ye, P., and Gong, Y. E. Simulation of refrigerant flow boiling in serpentine tubes. *International Journal of Heat and Mass Transfer 50*, 5-6 (2007), 1186–1195.

[168] Wu, W., Dai, S., Liu, Z., Dou, Y., Hua, J., Li, M., Wang, X., and Wang, X. Experimental study on the performance of a novel solar water heating system with and without PCM. *Solar Energy 171* (2018), 604–612.

[169] Xu, B., Li, P., and Chan, C. Application of phase change materials for thermal energy storage in concentrated solar thermal power plants: a review to recent developments. *Applied Energy 160* (2015), 286–307.

[170] Yan, S., Wang, F., Shi, Z., and Tian, R. Heat transfer property of SiO2/water nanofluid flow inside solar collector vacuum tubes. *Applied Thermal Engineering 118* (2017), 385–391.

[171] Yang, X., Bai, Q., Zhang, Q., Hu, W., Jin, L., and Yan, J. Thermal and economic analysis of charging and discharging characteristics of composite phase change materials for cold storage. *Applied Energy 225* (2018), 585–599.

[172] Yang, X., Sun, L., Yuan, Y., Zhao, X., and Cao, X. Experimental investigation on performance comparison of PV/T-PCM system and PV/T system. *Renewable Energy 119* (2018), 152–159.

[173] Yuan, W., Ji, J., Modjinou, M., Zhou, F., Li, Z., Song, Z., Huang, S., and Zhao, X. Numerical simulation and experimental validation of the solar photovoltaic/thermal system with phase change material. *Applied Energy 232* (2018), 715–727.

[174] Zheng, L., and Xuan, Y. Suppressing the negative effect of UV light on perovskite solar cells via photon management. *Solar Energy 173* (2018), 1216–1224.

VITA

Vivek Pawar has received his master's degree in Mechanical Engineering from Gannon University, PA, USA. He is currently pursuing his Ph.D. in Mechanical Engineering at UMKC. Vivek's main research interests include computational fluid dynamics modeling (CFD), heat transfer, multi-phase flow, and thermal energy storage. Currently, he is working on the CFD modeling with ANSYS Fluent as well as experimental analysis of solar thermal collectors. During his Ph.D., he worked as a graduate technical intern at Intel co. for the duration of 6 months. This internship helped him to gain knowledge in advanced flow visualization techniques using software tools like surface evolver, where he developed a CFD model to improve substrate manufacturing processes. He has published his PhD work as several peer reviewed journals and refereed conference proceedings, and he has also received the best student paper award in ASME 2021 Power Conference student competition program.